Electronic refrigeration and thermal couplings in supraconductor hybrid devices

Laëtitia Pascal

UNIVERSITÉ DE GRENOBLE

THÈSE

Pour obtenir le grade de

DOCTEUR DE L'UNIVERSITÉ DE GRENOBLE

Spécialité : **Physique/Nanophysique**

Arrêté ministérial : 7 août 2006

Présentée par

Laetitia Pascal

Thèse dirigée par **Hervé Courtois**

préparée au sein **Institut Néel**
et de **École doctorale de Physique**

Electronic refrigeration and Thermal couplings in Superconducting Hybrid Devices

Thèse soutenue publiquement le **30 mars 2012**,
devant le jury composé de :

Hélène Bouchiat
LPS Orsay, CNRS/Université Paris-Sud, Rapporteur
Hugues Pothier
Quantronics group SPEC, Cea Saclay, Rapporteur
Wiebke Guichard
Institut Néel, CNRS/Université de Grenoble, Examinateur
Francesco Giazotto
SNS Pise, NEST Istituto Nanoscienze-CNR, Examinateur
Clemens Winkelmann
INPG, CNRS, Examinateur
Hervé Courtois
Institut Néel, UJF/CNRS, Directeur de thèse

Table des matières

Remerciements

Ces années de thèse à l'Institut Néel ont été très enrichissantes tant scientifiquement, professionnellement mais aussi et surtout humainement. On l'oublie sans doute parfois mais c'est une chance exceptionnelle que de faire sa thèse à l'Institut Néel. Le laboratoire, notamment son couloir principal et ses cafétérias, incitent aux discussions et échanges avec les différents membres du laboratoire.
Je tiens tout d'abord à remercier sincèrement Hélène Bouchiat et Hugues Pothier pour avoir accepter d'être les rapporteurs de ma thèse. Mon manuscrit a été grandement enrichi grâce à leurs remarques et commentaires. I am really thankfull to Francesco Giazotto who accepted to be members of my thesis committee. Thank you for the collaboration we had in the past and the one we will have in the future. Je suis également très reconnaissante envers Clemens Winkelman d'avoir accepter de faire partie de mon jury de thèse, ainsi que pour ses remarques très constructives qui ont amélioré la clarté et la qualité du manuscrit. Ayant pu côtoyer Wiebke Guichard pendant mes années de thèse et apprécier ces qualités de physicienne, je la remercie profondément d'avoir présider mon jury de thèse.
Je tiens à remercier mon directeur de thèse Hervé Courtois pour avoir dirigé cette thèse, pour sa grande disponibilité malgé ses fonctions, et pour son soutien les derniers mois de thèse qui m'a permis de soutenir dans les temps. Je souhaite également exprimer ma profonde gratitude envers Bernard Pannetier. J'ai eu la chance de pouvoir bénéficier de sa pédagogie, de son savoir et de sa patience. En parlant de pédagogie, je remercie sincèrement Frank Hekking d'avoir pu bénéficier de ses talents de pédagogue qui m'ont permis de sentir le sens physique de ses calculs, avec simplicité sans pour autant négliger la rigueur scientifique et mathématique nécessaire.
J'ai eu le privilège durant ma thèse d'interagir avec un certain nombre de chercheurs. Je remercie donc Jukka Pekola pour les différentes discussions et ses remarques toujours très pertinentes qui m'ont beaucoup aidé, ainsi que de m'avoir fait confiance pour faire les mesures de refroidissement électronique sous faible champ magnétique. Par la même occasion je remercie Wolfgang Wernsdorfer de m'avoir laisser mesurer dans sa nouvelle Sionludi, un vrai bijou. Je remercie également Franck Balestro pour m'avoir laisser utiliser leur frigo à échantillons. Je remercie tous les chercheurs et thésard de l'équipe champ Proche notamment Olivier Arcizet pour ces conseils et Benjamin Sacépé pour les discussions lors des group meeting. Je remercie également Olivier Buisson de m'avoir invité au

réunion Cohérence Quantique. Je remercie Philippe Gandit pour m'avoir permis de maniper sur sa dilution et m'avoir fait profité de son expertise de Labview. I am thankfull for having worked with Anjan Gupta during my first year.
Je remercie le pôle électronique notamment Jean-Luc pour l'électronique, Daniel pour le porte-échantillon et Eric pour les contacts électromécaniques. Je remercie tout le pôle mécanique notamment Anne et Pierre pour leur aide dans la conception du porte-échantillon. Je remercie évidemment toute l'équipe Nanofab Bruno, Gwenaëlle, Sébastien, Jef, Thierry C. et Thierry F. Compte-tenu du temps que j'ai pu passé en salle blanche, j'ai pu apprécier votre excellent travail, votre bonne humeur et votre patience. Un grand merci à Thierry C. pour le miracle de la haute-tension de l'UHV. Je remercie également Véronique et Cécile pour leur aide pendant cette fin de thèse. Je remercie les services informatique notamment Patrick pour le déverolage d'ordi pendant la rédaction et le service cryogénique.
Je remercie mes formidables compagnons d'aventure de thèse Franck, Sukumar, Thomas, Sylvain. Je les remercie pour leur soutien et leur joie de vivre.
Je remercie tous les thésards et post-doc de l'Institut notamment Sayanti, Audrey G., Audrey D., Justine, Joanna, Romain V. pour le sample-sitting, son expertise en Python, Stefen pour son aide précieuse dans les mesures de champ magnétique, Matthias, Antoine, Raoul, Ioan, Iulian, Aurélien, David, Ahmad, Pierre, Olexei, Thomas, Dibyendu, Florent, Nicolas, Christoph, Germain, Danny et Oana pour leur bonne humeur et leur professionnalisme.
Je remercie tous mes amis pour être là dans les bons comme dans les mauvais moments malgré la distance, je suis la plus chanceuse de vous avoir ! Merci Armande, Cécilia, Louis, Davide, Camille, Vincent et Amélie.
Je remercie ma famille pour leur soutien indéfectible, leur compréhension qui m'ont permis d'arriver jusqu'au bout de cette thèse et au-delà. Merci Papa, merci Maman, pour m'avoir permis de faire ce que je voulais et d'être les merveilleux parents que vous êtes. Merci Clélia tu es la soeur que j'attendais, je suis heureuse que l'on reste si proche malgré les kilomètres. Merci de me faire rire. Je souhaite que tu puisses accomplir tes rêves.

Résumé

Le mot physique est issue du grec ancien et signifie «nature». Il s'agit de l'analyse générale de la nature, menée dans le but de comprendre comment l'Univers se comporte. Depuis l'Antiquité, l'Homme a essayé de comprendre son environnement, tout d'abord avec les règles de la physique classique. Cependant, confronté à des problèmes insolubles de manière classique, tels que le rayonnement du corps noir, le XX^e siècle a vu l'avènement de la mécanique quantique. Il découle de l'observation que certaines grandeurs physiques ne peuvent changer que par des quantités discrètes, ou quanta. Les points clés de la mécanique quantique sont la dualité onde-particule de l'énergie et de la matière et le principe d'incertitude et fournissent une vue unifiée du comportement des photons, électrons et autres objets à l'échelle atomique. Dans le même temps, la physique des basses températures s'est également développée, permettant de découvrir la supraconductivité. La supraconductivité est la propriété de certains matériaux de présenter une résistance électrique nulle à température suffisamment basse.
Prenons maintenant une jonction tunnel supraconductrice, où un métal normal est séparé d'un supraconducteur par une barrière tunnel. Lorsque la jonction est polarisée à proximité de sa bande d'énergie interdite, les quasi-particules les plus chaudes du métal normal peuvent passer dans le supraconducteur par effet tunnel. Grâce à sa bande d'énergie interdite, le supraconducteur se comporte ainsi comme un filtre en énergie. En outre, en raison de la symétrie de la densité d'états supraconducteur, l'effet de refroidissement est symétrique par rapport à la tension de polarisation. Une representation de ce phénomène serait quand on souffle sur sa soupe pour la redroidir. On enlève seulement les particules les plus chaudes à la surface, de telle sorte que la soupe refroidit.
Parfois, les gens sont induits en erreur sur le refroidissement électronique par effet tunnel et le considèrent comme un effet Peltier. L'effet Peltier a lieu quand on couple deux matériaux de constante thermoélectrique différente. Lorsqu'on applique une tension, un gradient de température apparaît alors entre les deux jonctions : une jonction refroidit tandis que la second chauffe. Le chauffage ou le refroidissement de la jonction est déterminée par la polarité de la tension appliquée, des dispositifs thermoélectriques sont des contrôleurs de température efficaces. Cet effet implique une accumulation de porteurs d'un côté du métal à proximité de la jonction chaude et une déplétion de densité de porteurs à la jonction froide.
Depuis l'apparition des premières jonctions supraconductrices de refroidissement dans

les années 90, des efforts ont été fait pour améliorer les performances des dispostitifs supraconducteur de refroidissement. En effet ces dispositifs sont plus petit qu'un pouce et assez compact par rapport à un réfrigérateur de dilution. En outre, leur fonctionnement ne nécessite pas de He3, dont la pénurie est aujourd'hui un grave problème pour l'obtention très basses températures. Les dernières versions de micro-réfrigérateurs supraconducteurs peuvent refroidir les électrons de 1K à 400 mK ou à partir de 300 mK jusqu'à 100 mK, simplement en appliquant un courant. Une telle solution est donc très intéressante pour améliorer la sensibilité des détecteurs dépendant de la température électronique, tels que les bolomètres. Enfin, l'application de ces dispositifs se soulève des enjeux technologiques et fondamentaux. Malgré des performances prometteuses de réfrigération électronique, leur température minimale réelle est loin d'atteindre les prédictions théoriques. En effet le bain électronique est couplé thermiquement à son environnement, par des voies de chauffage différentes. Comme le processus de relaxation des quasi-particules chaudes ayant tunneler du métal normal dans le supraconducteur est très lente, leur accumulation près de la jonction peut aussi diminuer l'efficacité du refroidissement électronique.

Contribution

Au cours de ma thèse, j'ai essayé de comprendre les différentes phénomènes limitatant la réfrigération électronique dans les circuits hybrides supraconducteurs. J'ai développé une méthode basée sur la théorie des circuits pour calculer la puissance thermique échangée par voie photonique à travers un cirucit par deux réservoirs à différentes températures. Cela me permet de concevoir une expérience, où le canal de chaleur photonique est négligeable, pour étudier le couplage électron-phonon dans une île du cuivre mésoscopiques, l'effet de volume et d'essayer d'observer directement le chauffage et le refroidissement des phonons. J'ai également mis en place un procédé de nanofabrication de larges jonctions NIS avec un ilôt de métal normal suspendu qui montre une amélioration de la puissance de refroidissement de l'ordre du nW. Enfin, j'ai étudié l'effet du champ magnétique perpendiculaire sur la puissance de refroidissement. En effet un petit champ magnétique permet une meilleure évacuation de chaleur des quasi-particules dans le supraconducteur. Chaque élément de mon travail de thèse est présentée dans un chapitre entier de ce manuscrit.

Plan du manuscrit

Dans le chapitre 1, je vous présente les outils et concepts essentiels pour comprendre les dispositifs à base jonctions tunnel supraconductrices. La première section est consacrée aux équations des jonctions métal Normal - Isolant - Supraconducteur (N - I - S) et le concept de réfrigération électronique. La deuxième section présente les différents couplages thermique existant dans nos dispositifs mésoscopiques le couplage électron-phonon, la résistance de Kapitza, le chauffage par les photons et le chauffage du aux

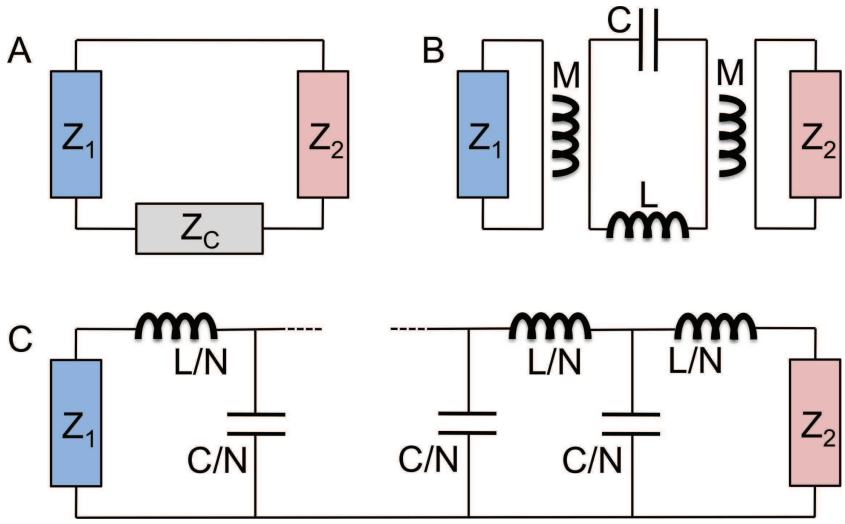

Figure 0.0.1: *Deux impédances Z_1 and Z_2 sont couplées: (A) une impédance purement réactive Z_c, (B) par l'intermédiaire d'inductances mutuelles à un îlot central purement réactif Z_c (ici un résonateur LC) ou (C) via une ligne de transmission.*

réflexions d'Andreev. Les concepts présentés dans ce chapitre constituent les requis de cette thèse.
Le deuxième chapitre présente une analyse théorique du transfert de chaleur par les photons entre deux systèmes métalliques de températures différentes couplé par un circuit contenant des impédances linéaires réactives, à savoir un circuit de couplage linéaire qui contient une inductance, un circuit résonnant ou une ligne de transmission ou un condensateur représenté Fig. 0.0.13.

Suivant une approche simple de type circuit, valable à basses températures lorsque la longueur d'onde charactéristiques des photons est plus grande que la taille de l'élément type du circuit, je traite les parties métalliques en éléments finis, caractérisées par une impédance électrique. Je montre que la densité spectrale de puissance transmise peut être écrit dans un formalisme de type Landauer-Büttiker, c'est-à-dire le produit de la différence des densité de puissance de bruit thermique de chaque élément résistif et le coefficient de transmission des photons. La figure 0.0.14 illustre le cas d'un couplage capacitif. L'analyse quantitative présentée, permet d'établir des règles utiles de conception des dispositifs, y compris les thermomètres phonons ou réfrigérateur électronique.

Les résultats obtenus décrivent très bien les observations expérimentales sur de circuits mésoscopiques [**?**, 89] et sont en accord avec les prédictions théoriques utilisant une

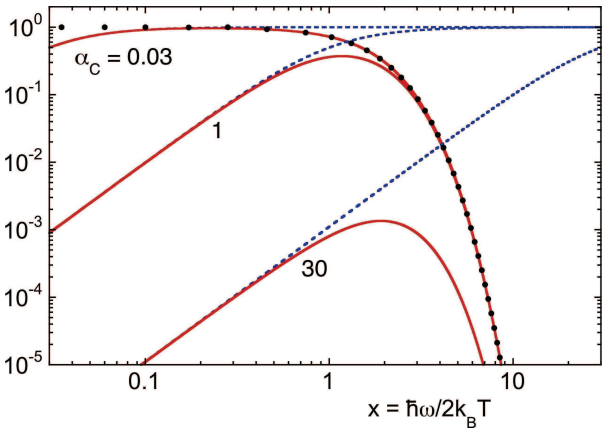

Figure 0.0.2: *Cas d'un couplage capacitif. Spectre de la densité de puissance de bruit thermique (points noirs), le coefficient de transmission de photons (pointillés bleu) et du produit des deux (fine ligne pleine rouge) en fonction de la fréquence, pour différentes valeurs du paramètreα_C. La fréquence est tracée dans les unités des fréquences $2k_BT/\hbar$.*

méthode utilisant des fonctions de Green hors équilibre pour l'étude du transistor de chaleur [53, 54]. Enfin, j'applique l'approche circuit pour prédire la chaleur photonique échangée dans le cas d'une ligne de transmission. Cette approche classique n'est pas exacte dans la limite de régime quantique puisque nous supposons que tout photon émis est absorbé.
Le chapitre 3 décrit deux différents procédés de fabrication des échantillons que j'ai utilisé ou développé durant ma thèse. Tout d'abord, j'ai conçu et fabriqué un «thermomètre à phonon». Il s'agit de deux circuits submicroniques supraconducteurs à base de jonctions tunnel galvaniquement découplés superposées. Ce dispositif requiert une première lithographie électronique alignée, suivie d'une évaporation de métal sous angle à travers un masque de résine et une seconde lithographie électronique alignée avec une précision de 50 nm à la première, terminée par une évaporation sous angle. Les deux circuits sont séparées par une couche d'oxyde de silicium. Une image SEM du dispositif est présenté Fig. 0.0.15.

Figure 0.0.3: *Image MEB du thermomètre à phonon*

Dans la deuxième partie, je présente la méthode établie avec H. Nguyen au cours de mon

doctorat pour fabriquer des jonctions tunnel supraconductrices hybrides de grandes surfaces avec une partie centrale métallique suspendue, illustré Fig. 0.0.16. Les échantillons sont fabriqués en combinant une photo-lithographie et une gravure chimique d'un dépôt multicouche supraconducteur-isolant-métal normal. Le processus comporte peu d'étapes de fabrication, est fiable et produit des jonctions tunnel d'excellente qualité. La méthode est basée sur une multicouche des métaux pré-déposée. La partie normale est suspendue lors de la première lithographie, ce qui l'isole du substrat. La seconde lithographie définit la géométrie des jonctions. Les mesures de transport de ces jonctions présentent d'excellentes caractéristiques IV, sans aucune fuite apparente. De plus en appliquant une polarisation appropriée, le dispositif montre un refroidissement électronique significatif de quelques centaines de picowatts.
Le quatrième chapitre présente les dispositifs cryogéniques et électroniques utilisés pour étudier des échantillons présentés dans les chapitres 5 et 6. Comme la température électronique est extraite des caractéristiques IV de jonctions NIS, une petite fluctuation de courant I, induit une grande fluctuation de tension V et par conséquent une grande incertitude de la température électronique. En outre, à basse température dans un système mésoscopique les électrons sont découplés du bain de phonons, ils sont donc prédisposés à refroidir mais également à chauffer facilement. Ainsi, dans le but de réduire le bruit et d'avoir une bonne thermalisation de notre système, nous avons concu en collaboration avec JL Mocellin une électronique bas bruit, limitée par le bruit thermique à température ambiante, et de faible courant (gamme pA), qui est capable de mesurer simultanément deux circuits isolés galvaniquement. J'ai aussi travaillé sur le filtrage électronique en changeant le thermocoax du porte-échantillon par un capillaire rempli d'une pâte contenant un absorbeur radiofréquence en plus d'un π-filtre et une traversée capacitive existant. Ces améliorations ont conduit à la mesure délicate du «thermomètre à phonon».
Le chapitre 5 présente l'expérience du «thermomètre à phonon» investigant sur le couplage électron-phonon et le couplage Kapitza dans un dispositif mésoscopique illustré sur la figure 5.2.1. Dans cette expérience, nous mesurons directement et indépendamment la température des électrons T_e et phonons T_{ph}. Cela permet de déterminer la loi de puissance et les préfacteurs des différents couplages thermiques.
De même que pour les expériences d'électrons chauds, une puissance est injecté dans un métal normal N_1 et la température électronique est mesurée par des SINIS jonctions. La puissance est calculée à partir du courant injecté. Le principe expérimental est schématisé par son modèle thermique figure 5.2.1.
La spécificité de cette expérience est que l'îlot de cuivre N_2 est ajouté au-dessus du fil de métal normal N_1 chauffée. Une jonction SINIS est utilisé pour sonder la température électronique N_2. L'îlot de métal normal N_2 est galvaniquement découplé de N_1 par une couche d'oxyde de silicium. L'îlot N_2 ne peut être chauffé que par le couplage électron-phonon. Ainsi, sans autre source de chaleur et en supposant que les mesures de température sont non-perturbatives, les électrons N_2 sont thermalisés aux phonons N_2.

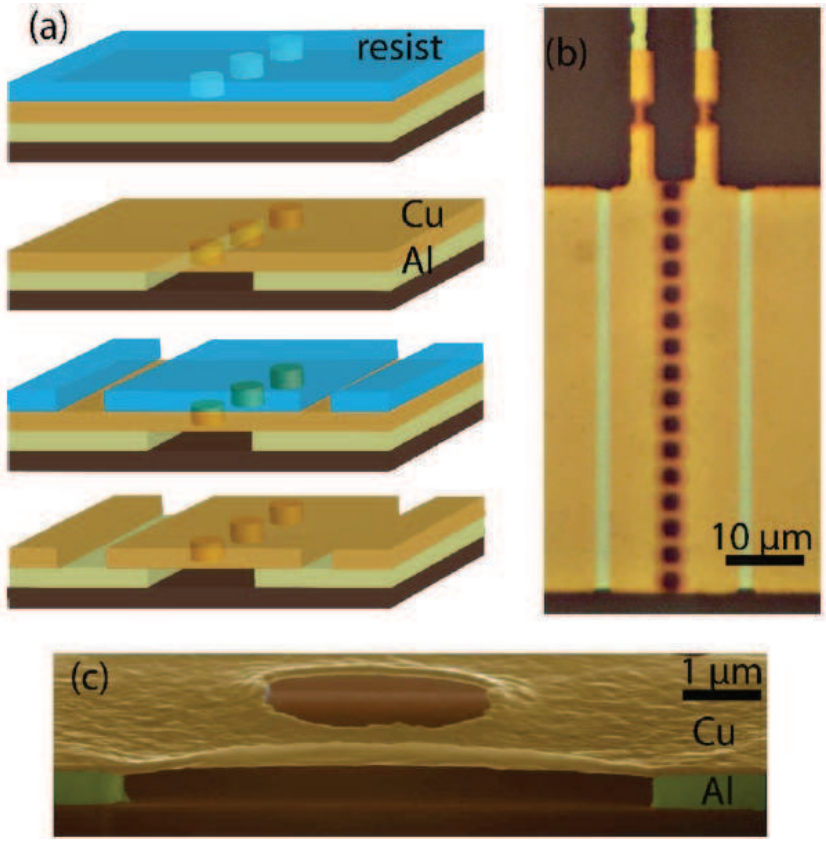

Figure 0.0.4: *(a) A partir du haut: la fabrication commence par une multicouche Al / AlOx / Cu, sur laquelle une photorésine est déposée et des plots de contact et des trous sont dessinés. Puis, Cu et Al sont successivement gravé, en laissant une membrane suspendue de Cu suivant la ligne de trous. Une seconde lithographie et une gravure définissent l'îlot central de Cu. (b) Image en microscopie optique montrant les régions en diminuant la luminosité: Al découvert, Cu sur Al, Cu suspendue et le substrat. Sur le dessus, deux jonctions thermomètre sont ajoutés. (c) micrographie électronique à balayage colorisée d'un échantillon découpé à l'aide faisceau d'ions focalisé, montrant la couche Cu suspendu au-dessus de la région des trous. L'épaisseur de Al et Cu est de 400 et 100 nm, respectivement.*

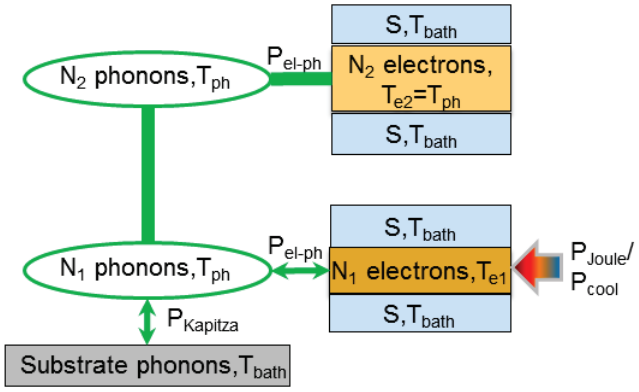

Figure 0.0.5: *Modèle thermique de l'expérience du thermomètre à phonon*

Cette expérience est très difficile en termes de fabrication, de mesures et d'interprétations. Durant ma thèse, j'ai conçu et fabriqué trois différentes générations de «thermomètre à phonon», les deux premiers sont étudiés dans ce chapitre. La première génération, représentée Fig.5.3.1, consiste en un fil de cuivre avec en son centre un thermomètre à électron SI-N_1-IS et une jonction tunnel SI-N_2 - IS au-dessus séparée par une couche d'oxyde de silicium. La figure 5.3.9 montre que l'augmentation de la température électronique par rapport à la puissance suit une loi en $P^{1/5}$ donnée par couplage électron-phonon dans des matériaux de volume. Toutefois, il existe un gradient de chaleur au niveau du fil de cuivre du à la perte de chaleur dans les plôts qui complexifie l'analyse des données.

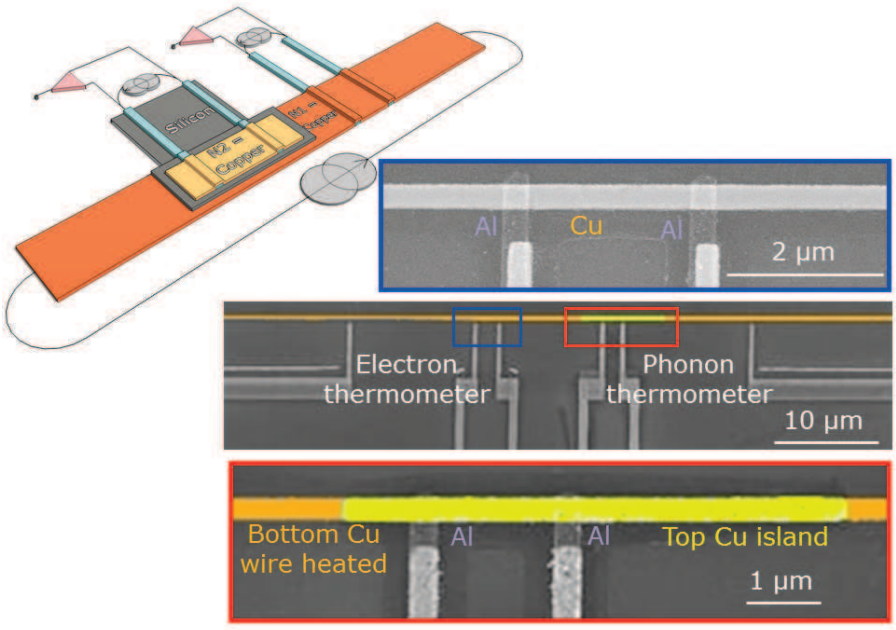

Figure 0.0.6: *Thermomètre phonon préliminaire: schéma et image MEB. L'encart bleu indique le thermomètre électronique fait d'une jonction SINIS, l'encadré rouge montre le thermomètre à phonon fait d'une jonction SINIS. En gris clair le cuivre, l'aluminium en gris et en gris foncé un substrat d'oxyde de silicium*

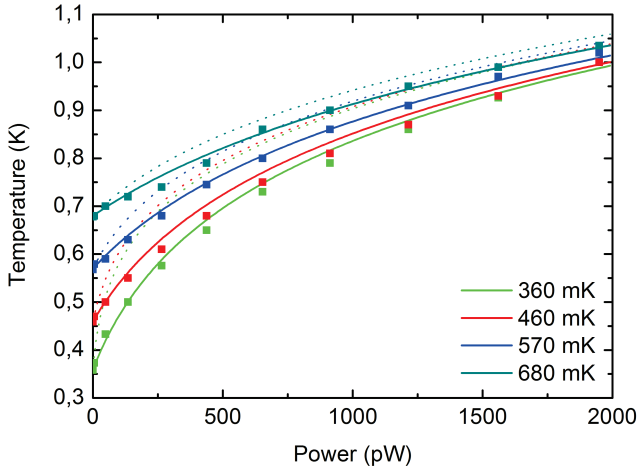

Figure 0.0.7: *Données fittées, considérant l'effet de gradient thermique. En ligne continue* $T_e = \sqrt[5]{P_{inj}/\Sigma V + T_{bath}^5}$, *en ligne discontinue* $T_{ph} = \sqrt[4]{P_{inj}/KA + T_{bath}^4}$ *avec* $\Sigma = 2000\,\mathrm{pW}.\mu\mathrm{m}^{-3}.\mathrm{T}^{-5}$ *et* $K = 44\,\mathrm{pW}.\mu\mathrm{m}^{-2}.\mathrm{T}^{-4}$

Pour simplifier le problème et avoir une température homogène électronique le long du fil de cuivre N_1, j'ai modifié le diqpositif du «thermomètre des phonons» plaçant aux extrémités de N_1 des jonctions tunnel, figures illustrées 5.4.1. Les jonctions tunnel à chaque extrémité sont polarisée en courant et de chauffe localement le fil de cuivre N_1. J'ai observé l'évolution thermique mesurée par les thermomètres à l'électron et à phonons.

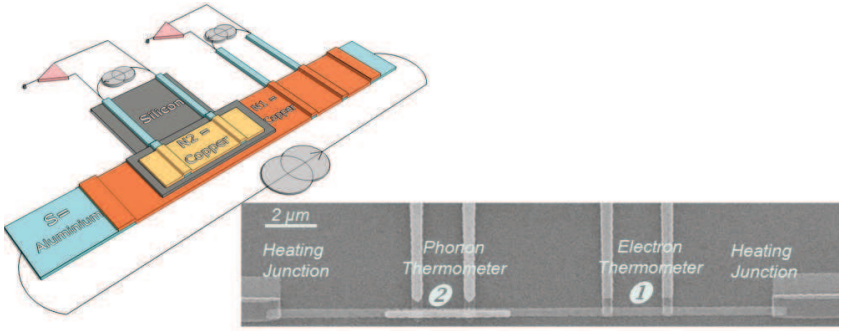

Figure 0.0.8: *En haut à gauche, un schéma de l'échantillon du thermomètre à phonons. Il ya une barrière tunnel d'oxyde d'aluminium entre les fils de cuivre (orange) et les fils d'aluminium (en bleu). le silicium recouvre entièrement le circuit du bas. En bas à droite, une image MEB du thermomètre à phonons.*

Dans la figure 5.4.8 l'évolution de T_e peut être décrite en considérant à la fois le couplage électron-phonon et le couplage de Kapitza avec $\Sigma = 2000\,\mathrm{pW}.\mu\mathrm{m}^{-3}.\mathrm{T}^{-5}$ et $K = 80\,\mathrm{pW}.\mu\mathrm{m}^{-2}.\mathrm{T}^{-4}$, alors que le comportement de T_{ph} est décrite en ne considérant que le couplage Kapitza mais avec une plus grande résistance de Kapitza $K' = 700\,\mathrm{pW}.\mu\mathrm{m}^{-2}.\mathrm{T}^{-4}$. L'îlot du haut est peut être plus couplé au substrat que prévu. En outre, le comportement thermique de T_e lorsque nous chauffons N_2 n'est pas similaire à celui de T_{ph} quand nous chauffons N_1. Pour quantifier le couplage de N_2 au substrat, comprendre l'asymétrie du comportement thermique et enfin être capable de travailler dans le régime de refroidissement, j'ai conçu et fabriqué une dernière génération où j'ai ajouté une jonction SI-N_2-IS de chauffage, j'ai raccourci la longueur de N_1 et augmenter la taille des jonctions.

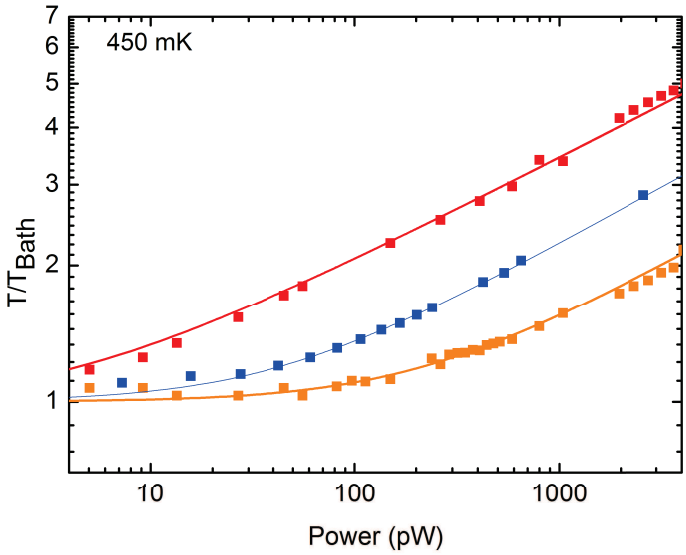

Figure 0.0.9: *Expérience faite à T_{bath}=450 mK. Données expérimentales: thermomètre à électron T_e (carré rouge) fittées par la courbe de température théorique (ligne rouge) données par* $T_e = \sqrt[5]{P_{inj}/\Sigma V + \left(P_{inj}/KA + T_{bath}^4\right)^{5/4}}$ *pour* $K = 80\,\mathrm{pW.K^{-4}}.\mu\mathrm{m}^{-2}$ *et* $\Sigma = 2000\,\mathrm{pW.K^{-5}}.\mu\mathrm{m}^{-3}$, *thermometre à phonon T_{ph} (carré orange) fittés par* $T_{ph} = \sqrt[4]{P_{inj}/K'A + T_{bath}^4}$ *(ligne orange) avec* $K' = 700, \mathrm{pW.K^{-4}}.\mu\mathrm{m}^{-2}$, *l'expérience inverse T_i (carré bleu) fittée par* $T_{ph} = \sqrt[4]{P_{inj}/K''A'' + T_{bath}^4}$ *(ligne bleu) avec* $K''A'' = 1215\,\mathrm{pW.K^{-4}}$ *où* $A'' = l_{Cu2}.w_{Cu2}$.

Enfin, le chapitre 6 présente l'étude sur la relaxation des quasi-particules dans le supraconducteur des micro-refroidisseurs SINIS sous champ magnétique, avec une analyse préliminaire. J'ai étudié les effets d'un faible champ magnétique et de la géométrie piège quasi-particules sur le refroidissement électronique d'un échantillon fourni par le groupe de Pekola Helsinki montré dans la figure 6.3.1 et mesurée dans la Sionludi de Wernsdorfer. En effet, pour un courant de polarisation donné I_{cooler} le refroidissement électronique est augmenté de près de 50% sous un faible champ magnétique de quelques Gauss 6.3.2. L'effet d'un faible champ magnétique sur le refroidissement est renforcé pour des sections 'a' larges à proximité de la jonction de refroidissement et semble insensible à 'b' et 'c', comme l'indique la figure 6.4.2. L'effet est maximal à un champ magnétique optimal B_{opt} égal au quantum de flux de B_0 soit 0,2 à 3,3 G dans nos géométries. Enfin on observe les effets de l'orientation du champ magnétique sur le refroidissement électronique.

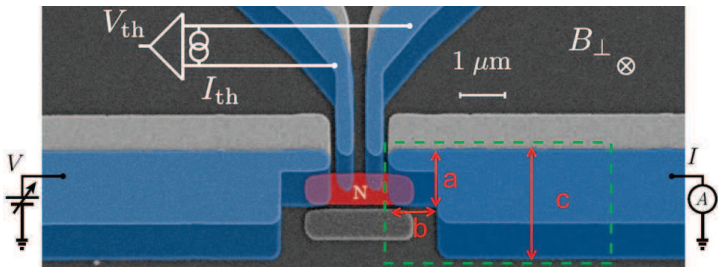

Figure 0.0.10: *SEM picture of cooler studied*

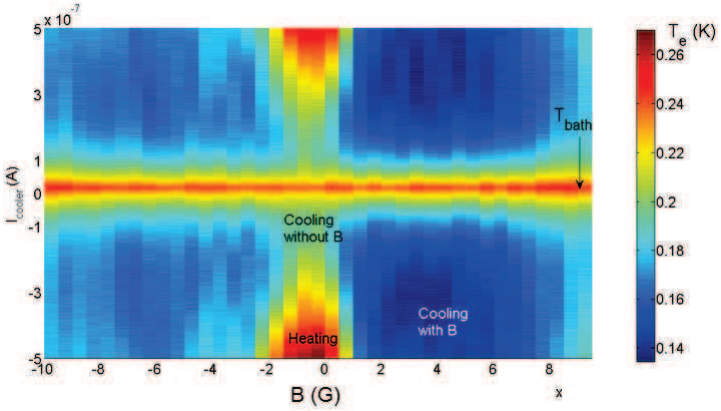

Figure 0.0.11: *Sample a25b10c5 @ T_{bath}=250 mK : map of T_e versus I_{cooler} and $B_\perp$. Color code blue to red as T_e increases.*

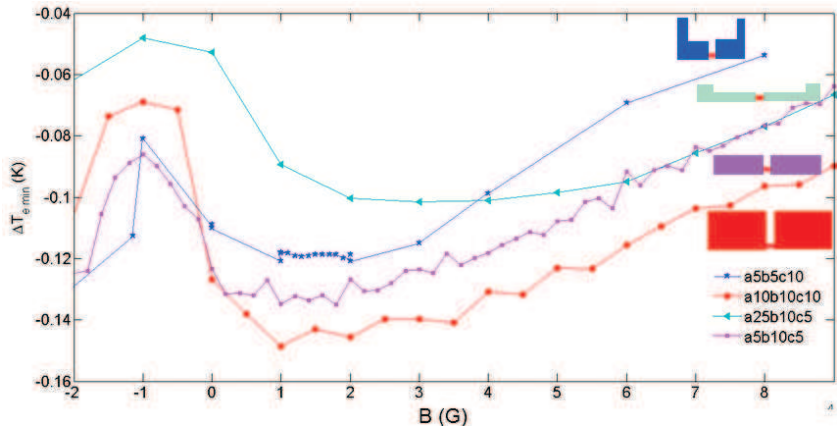

Figure 0.0.12: *Electronic refrigeration $\triangle T_{e\,min}$ under $B_\perp$ at T_{bath}= 300 mK: comparison of different qp-trap geometry: a5b5c10, a10b10c10, a25b10c5 and a5b10c5*

Introduction

Physics, coming from Ancient Greek and meaning «nature», is the general analysis of nature, conducted in order to understand how the Universe behaves. Since Antiquity, Men tried to understand their surroundings, with classical physics rules first. However, confronted to classically unsolvable problems, such as black body radiation and the related UV catastrophy, the XX^{th} century saw the advent of Quantum mechanics. It derives from the observation that some physical quantities can change only by discrete amounts, or quanta. The key-stones of quantum mechanics are the wave–particle duality of energy and matter and the uncertainty principle providing a unified view of the behavior of photons, electrons and other atomic-scale objects. At the same time, low-temperature physics was growing, enabling superconductivity discovery. Superconductivity is the property of some materials to have zero electrical resistance at sufficiently low temperature.

Let us consider now a superconducting tunnel junction, where a normal metal is separated from a superconductor by a tunnel barrier. When the junction is biased close to the energy gap, it allows the hottest quasi-particles of the normal metal to tunnel into the superconductor. Thanks to its energy gap, the superconductor actually act as a energy filter. Moreover, because of the symmetrical property of the superconducting density of states, the effect is symmetric at positive and negative voltage bias. A pictorial comparison would be when one blows on hot tea in a cup. One removes only the hottest particles at the surface, so that the tea cools.

Sometimes people are misled on superconductive tunnel cooling and consider it as a usual Peltier effect. Let us clarify this point before starting. Peltier effect happens when a couple of materials with a different thermoelectric constant is voltage-biased. A temperature gradient then appears between the two junctions: one junction cools down while the second one heats up. This effect can be used to measure a temperature or drive the temperature of objects. Because obtaining heating or cooling is determined by the polarity of the applied voltage, thermoelectric devices are efficient temperature controllers. This effect implies an accumulation of carriers on one side of the metal close to the hot junction and a depletion of carrier density at the cold junction.

Since the first superconducting cooling junctions appeared in the 90's, efforts have been done to improve superconductive cooling devices performance. Indeed such devices are smaller than 1 cm^2 and quite compact compared to a dilution fridge. Moreover, their

operation does not need any He3, whose shortage is nowadays a severe problem for very low temperature obtention. Last versions of superconducting micro-refrigerators can chill electrons from 1K down to 400 mK or from 300 mK down to 100 mK, simply by applying a current. Such a solution is thus very interesting to improve the sensitivity of detectors depending of the electronic temperature, such as bolometers. Finally the application of such devices rises technological and fundamental issues. Despite promising electronic refrigeration performances, their actual minimum reached temperature is far from the theoretical predictions. Indeed the electronic bath is thermally coupled to its environment through different heat channels. As the relaxation process of hot quasi-particles tunneling from the normal metal into the superconductor is very slow, their accumulation can also decrease the electronic cooling efficiency.

Contribution

During my thesis I have been interested in the understanding of the different limitations of electronic refrigeration. I established a method based on circuit theory to calculate the photonic heat power exchanged by to reservoir at different temperatures through a cirucit. This enables me to design an experiment, where the photonic heat channel is negligeable, to study the electron-phonon coupling in a mesoscopic copper island, the volume effect and try to observe directly the phonon heating and cooling. I also established a nanofabrication process of large N-I-S junctions with a suspended normal metal island that shows an enhancement of cooling power to nW range. Finally I studied the effect of perpendicular magnetic field on cooling power due to a better evacuation a hot quasi-particles in the superconductor. Each element of my thesis work is presented in an entire chapter of this manuscript.

Manuscript summary

In chapter 1, I introduce essential tools and concepts for understanding superconductive tunnel junctions based devices. The first section is dedicated to the Normal metal - Insulator - Superconductor (N - I - S) junctions equations and the electronic refrigeration concept. The second section presents the different thermal couplings taking place in our mesoscopic devices such electron-phonon coupling, Kapitza resistance, photon and Andreev heating. Concepts introduced in this chapter constitute the background of this thesis.
The second chapter presents a theoretical analysis of the electromagnetic heat channel in nanostructures. I calculate the heat transfer by photons between two metallic systems of different temperature coupled by a circuit containing linear reactive impedances, i.e. a linear coupling circuit that contains a capacitor, an inductance, a resonant circuit or a transmission line shown Fig. 0.0.13.

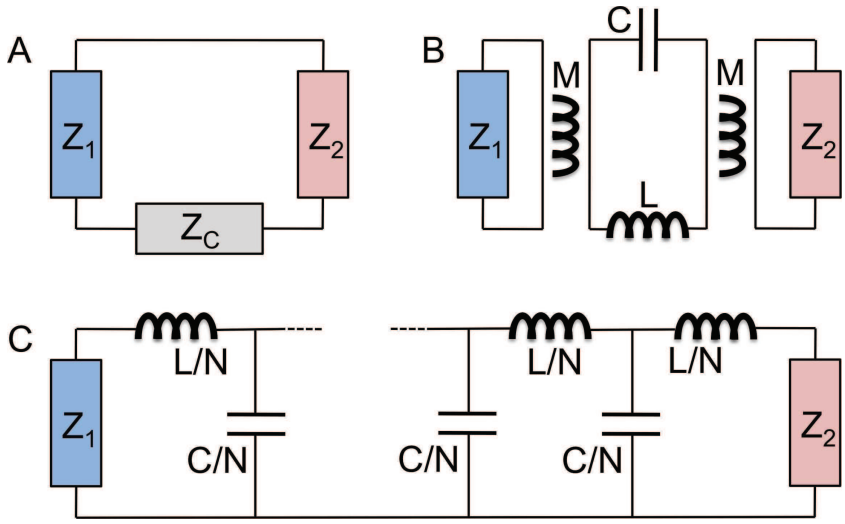

Figure 0.0.13: *Two impedances Z_1 and Z_2 are coupled by: (A) a purely reactive coupling impedance Z_c, (B) via mutual inductances to a purely reactive central circuit of total impedance Z_c (here an LC resonator) or (C) via a transmission line.*

Following a simple circuit approach, valid at low temperatures when the relevant photons have wavelengths larger than the size of the typical circuit element, I treated the metallic parts as lumped elements characterized by an electrical impedance. I show that the transmitted power spectral density can be written in a Landauer-Büttiker type formalism, product of the différence of the thermal noise power density of each element and the photon transmission coefficient. The figure 0.0.14 illustrates the case of a capacitive coupling. The quantitative analysis presented, enables to establish design rules for useful devices, including phonon thermometers or electron coolers.

The results obtained describe very well experimental observations on mesoscopic circuits [**?**, 89] and are in agreement with theoretical predictions using a non-equilibrium Green's functions method on heat transistor [53, 54]. Finally I apply the circuit approach to predict the photonic heat conducted in a transmission line. This classical approach is not accurate in the quantum regime limit since we assume that any photon emitted is absorbed.
Chapter 3 describes two different sample fabrication processes that I used or developped during my thesis. First, I designed and fabricated a «phonon thermometer» device. It is two sub-micron superconducting tunnel junctions circuits galvanically decoupled superposed to each other. This device requires a first aligned standard electron beam lithography, followed by a shadow evaporation of metal through a polymer resist mask and a second electron beam lithography aligned with a 50 nm precision to the first one,

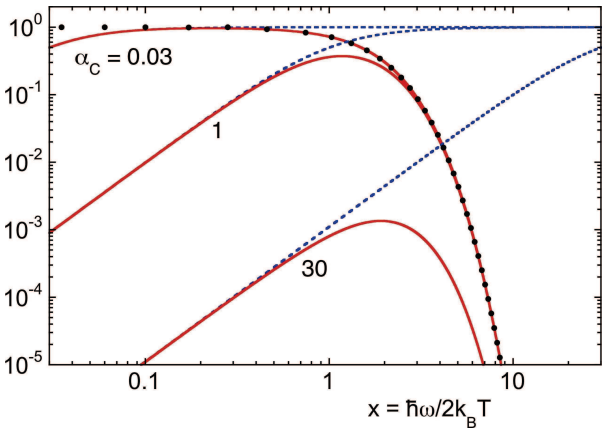

Figure 0.0.14: *Case of a capacitive coupling. Spectrum of the thermal noise power density (black dots), the photon transmission coefficient (dotted blue line) and of the product of the two (thin red full line) as a function of the frequency, for different values of the parameter α_C. The frequency is plotted in units of the thermal frequency $2k_BT/\hbar$.*

ended by a shadow evaporation. The two circuits are separated by a layer of silicon oxide deposit. A SEM picture of the device is presented Fig. 0.0.15.

Figure 0.0.15: *SEM image of phonon thermometer.*

In the second part I present the method established with H. Nguyen during my PhD to fabricate large-area superconducting hybrid tunnel junctions with a suspended central normal metal part presented Fig. 0.0.16. The samples are fabricated by combining photo-lithography and chemical etch of a superconductor—insulator—normal metal multilayer. The process involves few fabrication steps, is reliable and produces extremely high-quality tunnel junctions. The method bases on a pre-deposited multilayer of metals, which can be prepared at the highest quality. The normal part is suspended in the first lithography, which keeps it isolated from the substrate. The second lithography defines the junction area with any geometry of interest. Transport measurements on these junctions show excellent characteristics, without any leakage contribution. Under an appropriate bias, the device demonstrates a significant electronic cooling of few hundreds of picowatts.
The fourth chapter presents the cryogenic and electronic set-up used to study samples

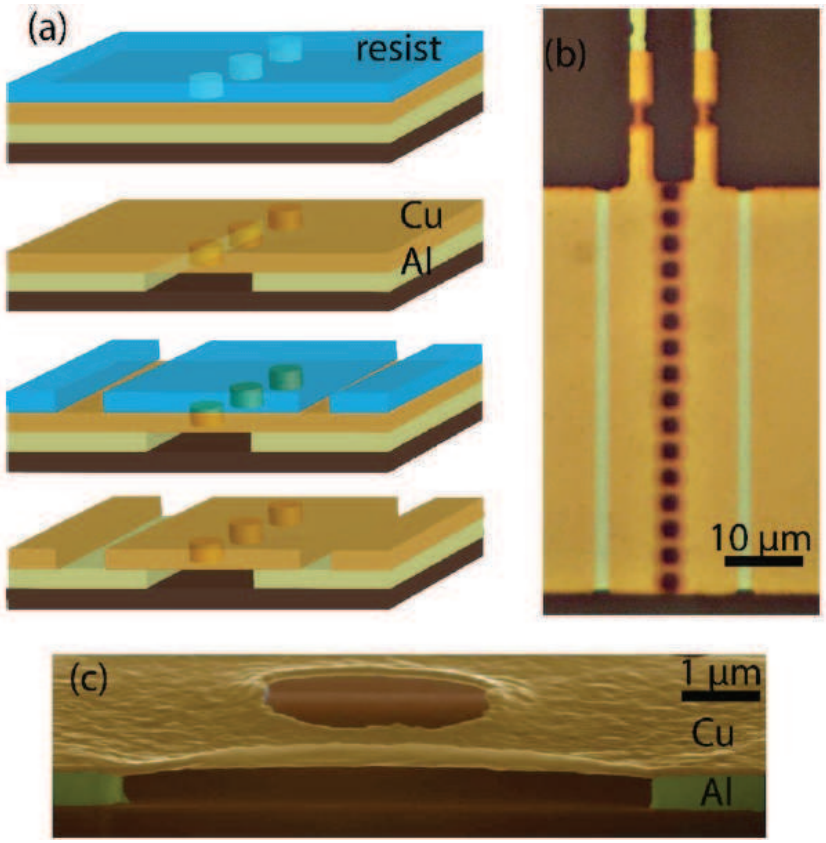

Figure 0.0.16: *(a) From top: fabrication starts with an Al/AlOx/Cu multilayer, on which a photoresist is patterned with contact pads and holes. Then, Cu and Al are successively etched, leaving a suspended membrane of Cu along the line of adjacent holes. A second lithography and etch define the Cu central island. (b) Optical microscope image showing regions by decreasing brightness: bare Al, Cu on Al, suspended Cu and substrate. On the top, two thermometer junctions are added. (c) Colorized scanning electron micrograph of a sample cut using Focused Ion Beam, showing the Cu layer suspended over the holes region. The thickness of Al and Cu is 400 and 100 nm, respectively.*

presented in chapters 5 & 6. Since the electronic temperature is extracted from the I-V characteristics of the N-I-S junction, a small fluctuation in current I implies a large fluctuation in voltage V and consequently a large incertainty on electronic temperature. Moreover at low temperature in mesoscopic device the electrons are well decoupled from the phonon bath, they are easy to cool down as well as to warm up. Thus in order to reduce the noise and thermalize properly our devices we design in collaboration with J-L Mocellin a low noise, limited by the thermal noise at room temperature, and low current (pA range) electronic box, that is able to measure simultanously two circuits galvanically isolated. I also worked on the electronic filtering by changing the thermocoax of the sample holder for a capillary filled with a two-component paste containing radiofrequency absorber over 200 cm at the cryostat base temperature in addition to a π-filter and a capacitive feedthrough. These improvements leads to the delicate measurement of «phonon thermometer».
The chapter 5 presents the «phonon thermometer experiment» investigating on electron-phonon and Kapitza coupling, established for bulk material, in a mesoscopic device illustrated on Figure 5.2.1. In this experiment we measure directly and independently the electron T_e and phonon T_{ph} temperatures and determine the power law and the prefactor of the different thermal couplings.
Similarly to hot electron experiments, a given power is injected in a normal metal N_1 and probe the electronic temperature by S-I-N-I-S junctions. The power is calculated from the current injected. The experimental principle is schematized by its thermal model in Figure 5.2.1.
The specificity of this experiment is that a copper island N_2 is added on top of the heated normal metal N_1. A S-I-N-I-S junction is used to probe the electronic temperature N_2. The N_2 island is galvanically decoupled from N_1 by a silicon oxide layer. The N_2 island can only be heated through electron-phonon coupling. Thus, without other source of heat and assuming non-perturbative temperature measurements, N_2 electrons are thermalized to N_2 phonons.

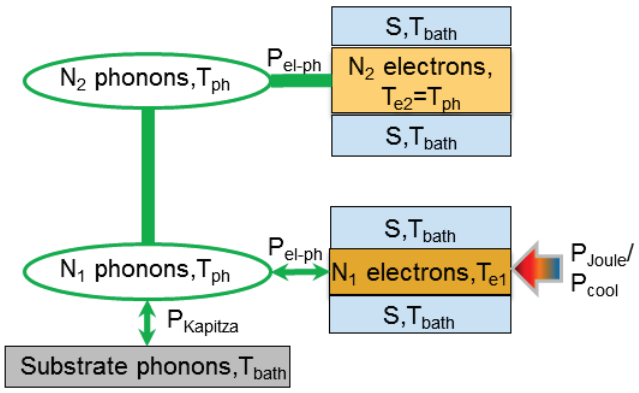

Figure 0.0.17: *Complete thermal model of the phonon thermometer experiment*

This experiment is very challenging in terms of fabrication, measurements and interpretations. During my PhD I have designed and fabricated three different generations of «phonon thermometer», the first two batches are studied in this chapter. The first generation, as depicted Figure 5.3.1, is a bottom copper wire N_1 with at its center a S-I-N_1-I-S tunnel junction as electron thermometer and an S-I-N_2-I-S tunnel junction above isolated by a silicon oxide layer. Figure 5.3.9 shows that the electronic temperature increase versus power follows a $P^{1/5}$ law given by electron-phonon coupling in bulk material. However the effect of the healing length can not be neglected and complexify the analysis because of the gradient temperature induced along the wire.

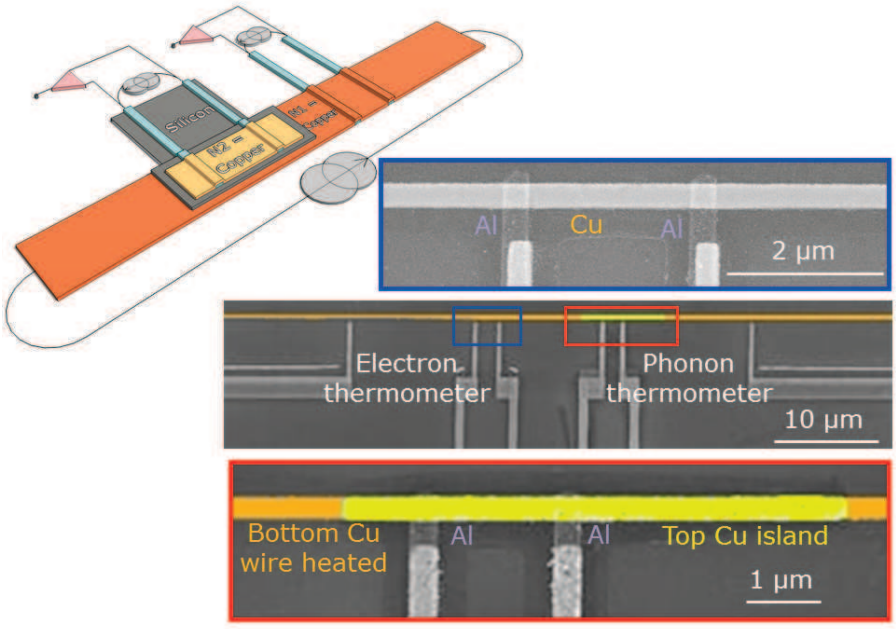

Figure 0.0.18: *Preliminary phonon thermometer: schematic and SEM image. The blue inset shows the electron thermometer made of a S-I-N-I-S junction, the red inset shows the phonon thermometer made of a S-I-N-I-S junction. In light gray is copper, gray is aluminum and dark gray is silicon oxide substrate*

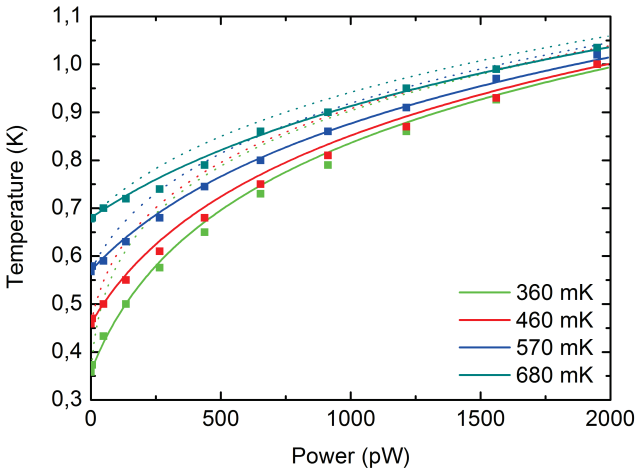

Figure 0.0.19: Data fitting including the thermal gradient effect. Continuous line is $T_e = \sqrt[5]{P_{inj}/\Sigma V + T_{bath}^5}$, dashed line is $T_{ph} = \sqrt[4]{P_{inj}/KA + T_{bath}^4}$ with $\Sigma = 2000\,\mathrm{pW}.\mu\mathrm{m}^{-3}.\mathrm{T}^{-5}$ and $K = 44\,\mathrm{pW}.\mu\mathrm{m}^{-2}.\mathrm{T}^{-4}$

To simplify the problematic and have an homogenous electronic temperature along the bottom copper wire N_1, I updated the «phonon thermometer» device by limiting the extremities of N_1 with tunnel junctions, illustrated Figures 5.4.1. The tunnel junctions at each extremities are current polarized and heat locally the copper wire N_1. I observed the thermal evolution measured by the electron and the phonon thermometers.

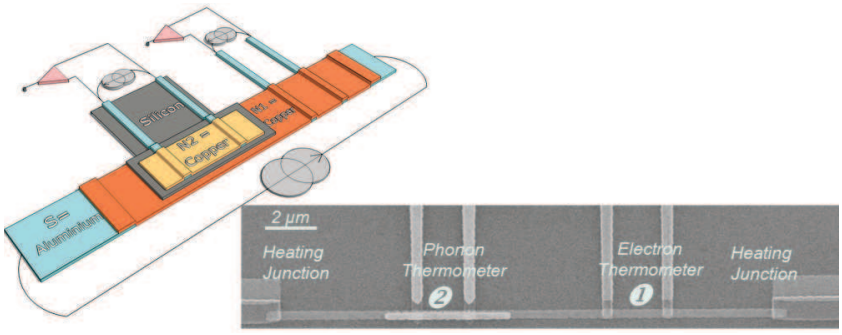

Figure 0.0.20: *At the top left, a schematic of phonon thermometer sample. There is a tunnel barrier of aluminum oxide between the copper wires (orange) and the aluminum leads (blue). Silicon covers the entire bottom circuit. At the bottom right, a SEM image of phonon thermometer.*

In Figure 5.4.8 the evolution of T_e can be described by considering both electron-phonon and Kapitza coupling with $\Sigma = 2000\,\mathrm{pW}.\mu\mathrm{m}^{-3}.\mathrm{T}^{-5}$ and $K = 80\,\mathrm{pW}.\mu\mathrm{m}^{-2}.\mathrm{T}^{-4}$, whereas the behaviour of T_{ph} is described considering only the Kapitza coupling with larger

Kapitza resistance $K' = 700\,\mathrm{pW}.\mu\mathrm{m}^{-2}.\mathrm{T}^{-4}$. Top island might be more coupled to the substrate than expected. Moreover the thermal behaviour of T_e when we heat N_2 is not similar to the one of T_{ph} when we heat N_1. To quantify the coupling of $N_2$to the substrate, to understand the assymetry of the thermal behaviour and finally to be able to work in the cooling regime I designed and fabricated a last generation where I added a S-I-N_2-I-S heating junction, I shortened the length of N_1 and increased the junctions sizes.

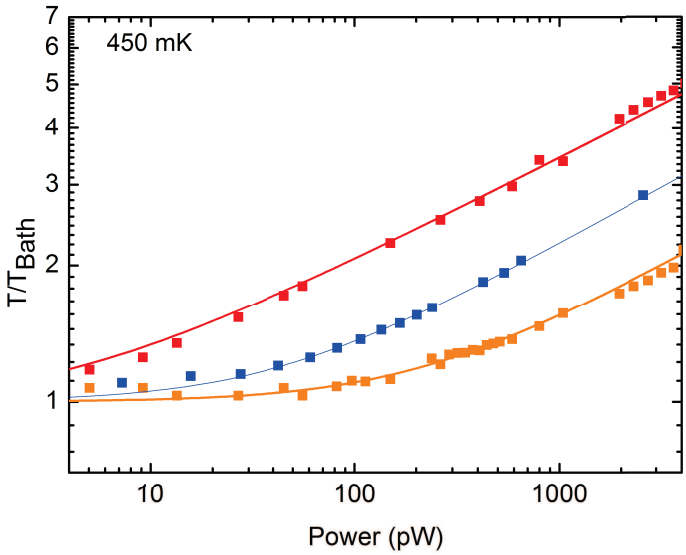

Figure 0.0.21: *Expreiment done at T_{bath}=450 mK. Experimental data: electron thermometer T_e (red symbols) fitted with the theoretical temperature evolution (red line) given by* $T_e = \sqrt[5]{P_{inj}/\Sigma V + (P_{inj}/KA + T_{bath}^4)^{5/4}}$ *for* $K = 80\,\mathrm{pW}.\mathrm{K}^{-4}.\mu\mathrm{m}^{-2}$ *and* $\Sigma = 2000\,\mathrm{pW}.\mathrm{K}^{-5}.\mu\mathrm{m}^{-3}$, *phonon thermometer T_{ph} (orange symbols) fitted by* $T_{ph} = \sqrt[4]{P_{inj}/K'A + T_{bath}^4}$ *(orange line) with* $K' = 700,\ \mathrm{pW}.\mathrm{K}^{-4}.\mu\mathrm{m}^{-2}$, *inverted experiment T_i (blue symbols) fitted by* $T_{ph} = \sqrt[4]{P_{inj}/K''A'' + T_{bath}^4}$ *(blue line) with* with $K"A" = 1215\,\mathrm{pW}.\mathrm{K}^{-4}$ where $A" = l_{Cu2}.w_{Cu2}$.

Finally, Chapter 6 presents investigations on quasi-particles relaxation in the superconductor leads of S-I-N-I-S micro-coolers under magnetic field, together with a preliminary analysis. I studied the effects of a small magnetic field and the quasi-particles trap geometry on electronic cooling on sample provided by the Pekola's group in Helsinki shown Figure 6.3.1 and measured in Wernsdorfer's fridge. Indeed at given current of polarization I_{cooler} the performance of electronic cooling is enhanced by almost 50% under magnetic field of few gauss 6.3.2. The effect of a small magnetic field improve for large

sections 'a' close to the cooling junction and looks insensitive to 'b' and 'c', as shown in Figure 6.4.2. The effect is maximum at an optimum magnetic field B_{opt} equals to the quantum of flux B_0 ie 0.2 to 3.3 G in our geometries. Finally we observed the effect of the orientation of the magnetic field on the electronic cooling.

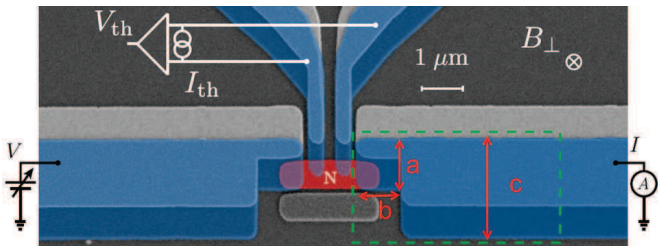

Figure 0.0.22: *SEM picture of cooler studied*

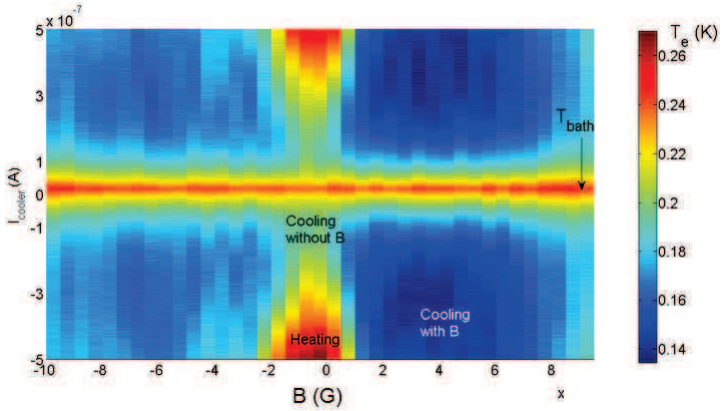

Figure 0.0.23: *Sample a25b10c5 @ T_{bath}=250 mK : map of T_e versus I_{cooler} and $B_\perp$. Color code blue to red as T_e increases.*

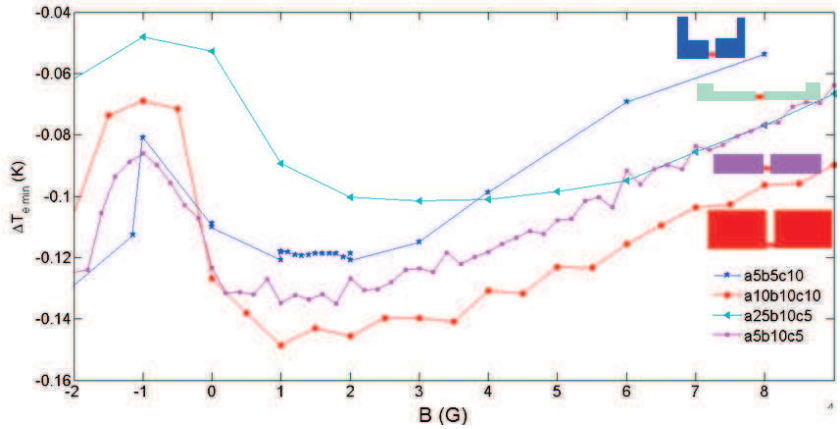

Figure 0.0.24: *Electronic refrigeration $\triangle T_{e\,min}$ under $B_\perp$ at T_{bath}= 300 mK: comparison of different qp-trap geometry: a5b5c10, a10b10c10, a25b10c5 and a5b10c5*

Chapter 1

Superconductive tunnel junctions

1.1 Introduction

In this chapter we introduce basics concepts and tools to understand the following chapters. First, we review briefly the basic properties of superconductivity and quantum tunneling that are involved in tunnel junctions devices. We explain in detail the electronic refrigeration and the electron thermometry concepts, including their limitations. Then we present the different thermal couplings taking place in mesoscopic devices and discuss in more details the case of our devices.

Historical overview

At the end of XIXth century, several physicists, among them Kamerlingh Onnes, were interested in the metallic resistance behavior in the limit of a zero temperature. In 1908, the Dutch physicist made a first breakthrough with helium liquefaction, thus providing access to temperatures of few Kelvin. It allowed him to observe that below a given temperature, i.e. 4.2 K, mercury had no electrical resistance. This phenomena was called superconductivity since the metal can carry current without dissipation. In the following years, physicists found superconductivity in numerous other materials and studied its interplay magnetic field (Meissner effect). First steps towards a microscopic theory occured only in 1950 with Frohlich's theoretical model including an attractive electron-electron interaction mediated by phonons. Seven years later, Bardeen, Cooper and Schrieffer succeeded to formulate a theory [6], well-known nowadays as BCS theory, able to account for a large number of experimental results. The next important development in this direction was done by Bogoliubov et al. who re-derived the BCS results using a net mathematical technique.
Finally, the first clear demonstration of superconductive tunneling was done in 1960 by Giaever et al [22, 21, 24, 23]. With this ground breaking experiment, Giaever did not only open a new realm of experimental work on superconductors, but also created the hope

for further discoveries about tunneling into metals, semi-metals, and semiconductors. Subsequently, experiments have been pursued to investigate the energy gap dependance with temperature, magnetic field, transport current, film thickness, and scattering rate on magnetic impurities.

1.2 N-I-S junction equations

1.2.1 BCS superconductors

Electron-phonon interaction and Cooper pairs

The difficulties to obtain a microscopic description of superconductivity lies in the small scale of the interaction energy. Indeed a type I superconductor critical magnetic field of a few hundred Gauss means a difference of energy between normal and superconducting states given by $^1/_2\mu_0 H_C^2$ of the order of 10^{-8}eV per atom, which is very weak compared to the Fermi energy of the order of 10 eV.
As already indicated above, Frohlich [18] formulated the idea of a mechanism based on electron-phonon interaction. According to this idea, an electron can be affected by the lattice deformation due to another electron. In this way, electrons exchange a virtual phonon. Describing the effect in term of wave vectors, an electron of wave vector k emits a phonon q that is afterwards absorbed by an electron of wave vector k'. It ends up that the resulting electron-electron interaction is attractive for low phonon energy $\hbar\omega_q$.
Cooper et al. [6] showed that in the presence of an attractive interaction, two electrons close to the Fermi energy can form a bound state, called afterwards a Cooper pair. The lowest energy is achieved when electrons of opposite momenta $(k, -k)$ and spins (↑,↓) couple.

Elementary excitations and the energy gap

BCS theory is based on attractive interaction between electrons. Cooper pairs follow a bosonic distribution and form a condensate at zero temperature, whereas at finite temperature quasi-particle excitations appears.
According to BCS theory, the Density Of States (DOS) at an energy E with respect to the Fermi level follows in a superconductor the expression:

$$N_s(E) = \begin{cases} \left| N_N(0) \frac{E/\Delta}{\sqrt{(E/\Delta)^2 - 1}} \right| & , \; for \; |E| > \Delta \\ 0 & , \; for \; 0 \leq |E| < \Delta \end{cases} \tag{1.2.1}$$

where $N_N(0)$ is the two-spin density of states at the Fermi level in the normal state.
As shown in Figure 1.2.5, the superconducting density of states is zero for energies lower than gap energy Δ, and presents a singularity at $E = \Delta$ containing the states

displaced from $|E| < \Delta$.
Another important result from the BCS theory is the relation between the energy gap at T = 0 K, $\Delta(0)$ and the critical temperature T_C that can be approximated by:

$$\Delta(0) = 1.764\, k_B T_C \tag{1.2.2}$$

It is also possible to extract a temperature dependance of the gap from BCS equations [90] :

$$\frac{\Delta(T)}{\Delta(0)} = \begin{cases} 1, & \text{for } T \ll T_c \\ 1.74\sqrt{1 - \frac{T}{T_C}}, & \text{for } T \sim T_c \\ 0, & \text{for } T \geqslant T_c \end{cases} \tag{1.2.3}$$

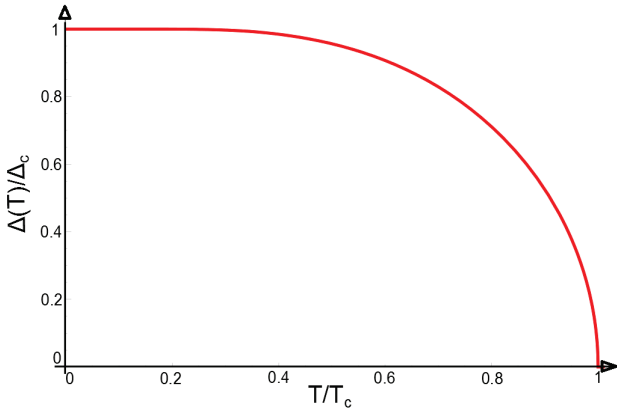

Figure 1.2.1: *The reduced energy gap as a function of reduced temperature according to BCS theory*

Quasi-particle vs normal electron : semiconductor model

To describe correctly the energetic diagram of superconductor, it makes more sense to discuss in terms of quasi-particles and Cooper pairs instead of normal and superconducting electrons. We use the so-called semiconductor model to describe quasi-particles in superconductors because of their similarities with semiconductor electron-hole pairs:
– 2Δ minimum energy to create two quasi-particles from a Cooper pair break-up.
– Quasi-particles can recombine and emit a phonon or a photon
– Quasi-particles are fermions
However, the description shall consider the singularity of the electronic DOS above and below the energy gap.

1.2.2 Tunneling effects

The concept of tunneling was born in 1928 [19] almost simultaneously with modern quantum mechanics. Basically, it is the non-zero probability for a particle moving towards a potential barrier to appear on the other side of the barrier. The probability of charge transfer decreases exponentially with the barrier strength (width and height). This applies in particular to electrons at the junction formed between two metals by a thin insulator layer.

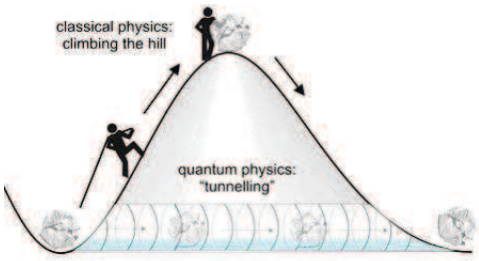

Figure 1.2.2: *Quantum tunnelling*

In many experiments of the last two decades, Normal metal - Insulator - Superconductor (N-I-S) tunnel junctions have proven to be an easy and powerful tool to probe a series of different physical quantities, including the electronic DOS, local potential, electronic temperature, electron energy distribution[22, 24, 64, 25, 26] in mesoscopic devices. Indeed an N-I-S junction is characterized by :

– The electron distribution function of Normal metal and Superconductors, following a quasi-equilibrium Fermi distribution $f_{N,S}(E,T)$ given by:

$$f_{N,S}(E,T) = \frac{1}{e^{E/k_B T_{N,S}} + 1} \tag{1.2.4}$$

where $T_{N,S}$ is the temperature of the normal metal or superconductor, E is defined to be the energy of an excitation with respect to the Fermi level, and k_B is the Boltzmann constant. A useful mathematical property of the Fermi function used in the following sections is:

$$f_{N,S}(-E) = 1 - f_{N,S}(E) \tag{1.2.5}$$

– The DOS of the Normal metal, considered as a bulk material. In the free electron model, the DOS of metal, given by $N_N(E) = \frac{1}{2\pi^2}\left(\frac{2m}{\hbar^2}\right)^{3/2} E^{1/2} \simeq \frac{2mk_F}{2\pi^2\hbar^2}$, varies slowly at the scale of the superconducting gap. Thus is considered as a constant in our calculations.

– The DOS of the Superconductor that follows BCS theory, i.e. Eq. 1.2.1.

1.2.2.1 Charge current in Normal metal 1 - Insulator - Normal metal 2

Introducing tunneling effect between two normal metals gives an easy way to establish all tunneling equations (current, power) in a tunnel junction. Let us then consider two normal metals N_1 and N_2 separated by a thin layer of insulator I or vacuum, i.e. a tunnel barrier. At thermal equilibrium without voltage bias, the Fermi levels of the two metals match, see Fig. 1.2.3. If a negative voltage V is applied to the normal metal N_1, its electron population has have an energy shifted by eV, as depicted on the energy

diagram in Figure 1.2.3.
From Fermi golden rule, the tunneling rate from N_1 to N_2, Γ_{12} is proportional to the number of occupied states in N_1, to the number of available states of N_2 and to the tunneling probability of an electron $P_{1\mapsto 2}(E)$:

$$\Gamma_{1\mapsto 2} \propto P_{1\mapsto 2}(E) N_1(E-eV) f_1(E-eV) N_2(E) \left[1-f_2(E)\right] \tag{1.2.6}$$

Similarly in the opposite direction the tunnel rate Γ_{21} is:

$$\Gamma_{2\mapsto 1} \propto P_{2\mapsto 1}(E) N_2(E) f_2(E) N_1(E-eV) \left[1-f_1(E-eV)\right] \tag{1.2.7}$$

The net current flowing from N_1 to N_2 is obtained by integrating the difference $\Gamma_{1\mapsto 2} - \Gamma_{2\mapsto 1}$ over all energy values, multiplied by the charge of an electron $-e$:

$$I_{12} = -e \int_{-\infty}^{+\infty} dE \left(\Gamma_{1\mapsto 2} - \Gamma_{2\mapsto 1}\right) \tag{1.2.8}$$

The usual approximation is to take $P_{1\mapsto 2}(E) \simeq P_{2\mapsto 1}(E) \simeq P$ independent of energy in our working range, so that we can take it out of the integral. Similarly the DOS of a normal metal varies slowly with E when $eV \ll E_F$. Each DOS approximates to a constant so that $N_1(E-eV) \sim N_1(E) = N_1(0)$ and $N_2(E) = N_2(0)$. Thus we can express the net current as:

$$\begin{aligned} I_{12} &\propto -eP N_1(0) N_2(0) \textstyle\int_{-\infty}^{+\infty} dE \ \left[f_1(E-eV)\left[1-f_2(E)\right] - f_2(E)\left[1-f_1(E-eV)\right]\right] \\ &\propto -eP N_1(0) N_2(0) \textstyle\int_{-\infty}^{+\infty} dE \ \left[f_1(E-eV) - f_2(E)\right] \end{aligned} \tag{1.2.9}$$

The net current is then given by:

$$I_{12} = e^2 V P N_1(0) N_2(0) \tag{1.2.10}$$

A $N_1 - I - N_2$ tunnel junction obeys Ohm's law i.e. $I_{12} = {}^{V}/_{R_N}$. We obtain that $P = {}^{1}/_{R_N e^2 N_1(0) N_2(0)}$, so the prefactor of the current is directly related to the normal state tunnel resistance R_N.

1.2.2.2 Charge current in Normal metal - Insulator - Superconductor junction

Let us now consider an N-I-S junction [50, 22], the main difference being that the superconducting DOS is not constant, but follows the BCS DOS. The previous constant DOS $N_2(0)$ is replaced by Expression 1.2.1 and index 1 by N and 2 by S. Thus the expression of net current flowing through the tunnel junction I is:

$$I = \tfrac{1}{eR_N} \textstyle\int_{-\infty}^{+\infty} dE \ \Re e\left[\frac{|E|}{\sqrt{E^2-\Delta^2}}\right] \left[f_N(E-eV)\left[1-f_S(E)\right] - f_S(E)\left[1-f_N(E-eV)\right]\right] \tag{1.2.11}$$

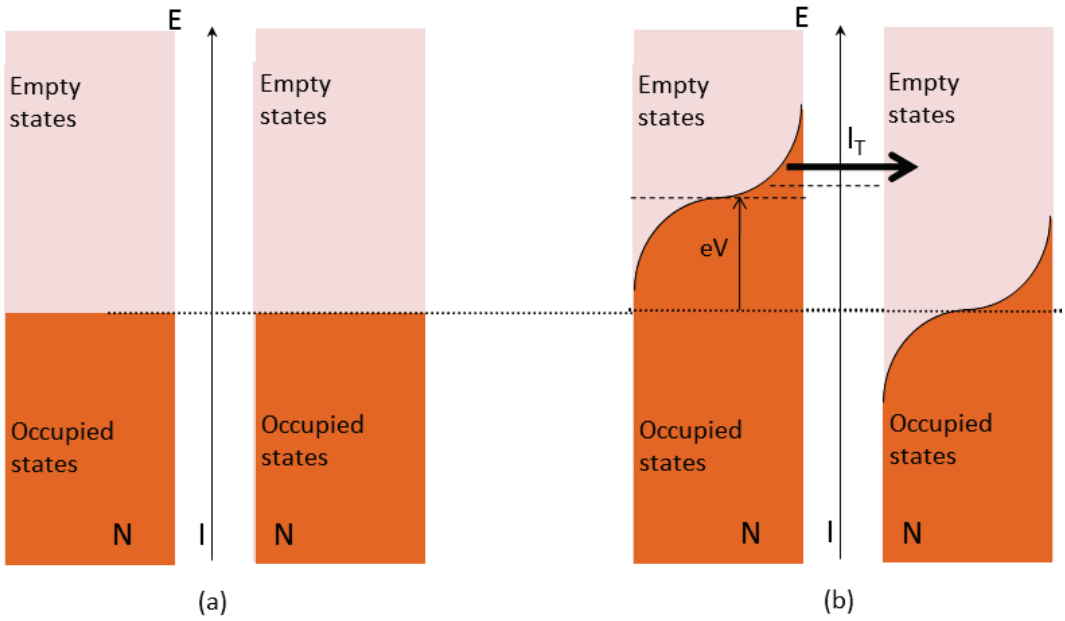

Figure 1.2.3: *Energy diagram of $N_1 - I - N_2$ junction : (a)At equilibrium (b)Junction biased at eV*

Using property 1.2.5 and the symmetry of BCS DOS, the net current I_{NS} can be simplified to :

$$I = \frac{1}{eR_N} \int_0^{+\infty} dE \, \frac{|E|}{\sqrt{E^2-\Delta^2}} \left[f_N(E - eV) - f_N(E + eV) \right] \tag{1.2.12}$$

The formula 1.2.12 shows no direct dependence to the temperature of the superconductor, but it still does depend on temperature through the temperature dependance of the energy gap Δ. Nevertheless, at low temperature $T < 0.3T_c$, we can consider the energy gap as constant $\Delta(T) \simeq \Delta(0)$.

Figure 1.2.4 shows calculated IV characteristics of a $N-I-S$ tunnel junction for different electronic temperatures. The energy diagrams, Figure 1.2.5, can describe pictorially the IV characteristics. At finite temperature T, for a low voltage most of the occupied states of the normal metal are at a lower energy than the energy gap of the superconductor, so that there are no available states for electrons occupying these states to tunnel to. Thus most of the normal metal occupied states do not contribute to tunneling current. For a bias close the gap energy $V = \Delta/e$, there is a sudden rise in current, because electrons from the Normal metal have access to the superconductor empty states just above the gap. Furthermore, they face a large density of states, namely the BCS singularity. For a large bias $V > \Delta/e$, the current still increases since more empty states of the superconductor become available for tunneling. Finally for $V \gg \Delta/e$, the IV merges to the usual resistive state of a tunnel junction, following Ohm's law.

We know that the energy distribution of electrons in a normal metal is smeared by temperature. It means that for agiven voltage bias, more current flows when the electronic

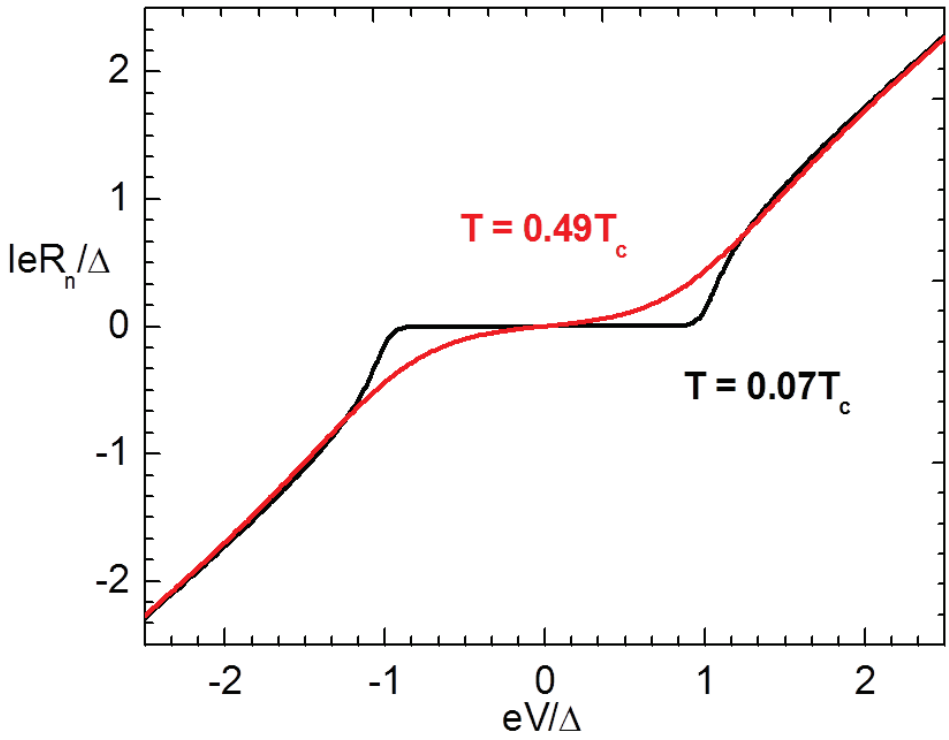

Figure 1.2.4: *IV characteristic of a N-I-S tunnel junction for different temperatures*

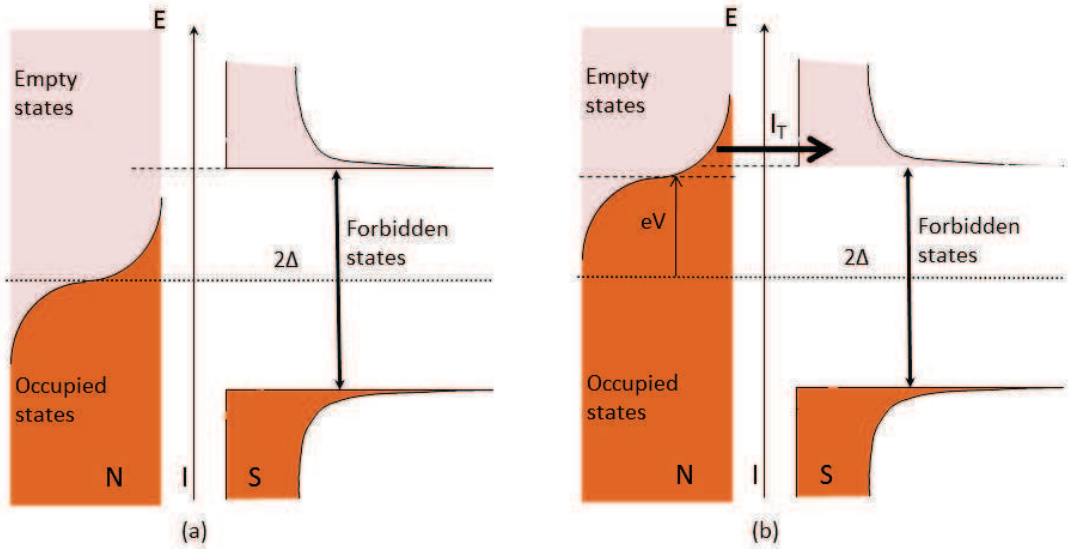

Figure 1.2.5: *Energy diagram of N-I-S junction : (a) At $T > 0$ with zero voltage bias (b) A $T > 0$ with voltage bias $V \lesssim \Delta/e$*

temperature is higher. Consequently, and as Figure 1.2.4 suggests, a N-I-S junction can be used as an electronic thermometer. This property first shown by Blackford and March [9]. This fact is the keystone of the thesis!
For $\Delta \gg k_B T_e$ and $0 \ll eV < \Delta$ the current through N-I-S junction can be written as [84]:

$$I(V) \simeq \frac{\Delta}{eR_N}\sqrt{\frac{\pi k_B T_e}{2\Delta}} e^{\frac{eV-\Delta}{k_B T_e}} \tag{1.2.13}$$

By differentiation, we obtain :

$$\frac{dI(V)}{dV} \simeq \frac{1}{R_N}\sqrt{\frac{\Delta\pi}{2k_B T_e}} e^{\frac{eV-\Delta}{k_B T_e}} \tag{1.2.14}$$

The interesting point is that under these conditions, the slope of the normalized conductance in a log-scale gives directly the electronic temperature T_e:

$$ln\,\frac{dI(V)}{dV} \propto \frac{eV}{k_B T_e} + \frac{1}{2} ln\left(\frac{\Delta\pi}{2R_N^2 k_B T_e}\right) - \frac{\Delta}{k_B T_e} \tag{1.2.15}$$

1.2.2.3 Charge current in Superconductor 1 - Insulator - Superconductor 2 junction

Even if it is not used in this thesis, I would like to present also the $S_1 - I - S_2$ case [24], where $\Delta_{S_1} < \Delta_{S_2}$, since I think that it is interesting and can be useful for future application of a « cascade cooler » and to engineer the optimum cooler in the required bath temperature range. The current flowing through the $S_1 - I - S_2$ junction is calculated similarly to the $N - I - S$ or $N_1 - I - N_2$, considering the BCS DOS of each superconductor:

$$I = \frac{1}{eR_T}\int_{-\infty}^{+\infty} dE\, \frac{|E|}{\sqrt{E^2\text{-}\Delta_{S_2}^2}} \frac{|E-eV|}{\sqrt{(E-eV)^2\text{-}\Delta_{S_1}^2}} \left[f_{S_1}(E-eV) - f_{S_2}(E)\right] \tag{1.2.16}$$

The IV characteristic and further the normalized conductance show features at $V = \frac{\Delta_{S_2}+\Delta_{S_1}}{e}$ as expected, and also at $V = \frac{\Delta_{S_2}-\Delta_{S_1}}{e}$ because of thermally excited quasiparticles at finite temperature.

Finally, to calculate the current through an S-I-N-I-S or a S-I-S'-I-S device with two junctions in series, one can calculate the current for single junction and then double the voltage: $I_{SINIS}(R_{SINIS}, V_{SINIS}) = I_{SIN}(R_{SINIS}/2, V_{SINIS}/2)$.

1.2.3 Heat transfer in superconductive tunnel junction

In the previous section, we discussed the charge current across hybrid tunnel junction-based devices. However, what we are really interested in is the heat current due to electron tunneling through the junction. Starting from the charge current expression,

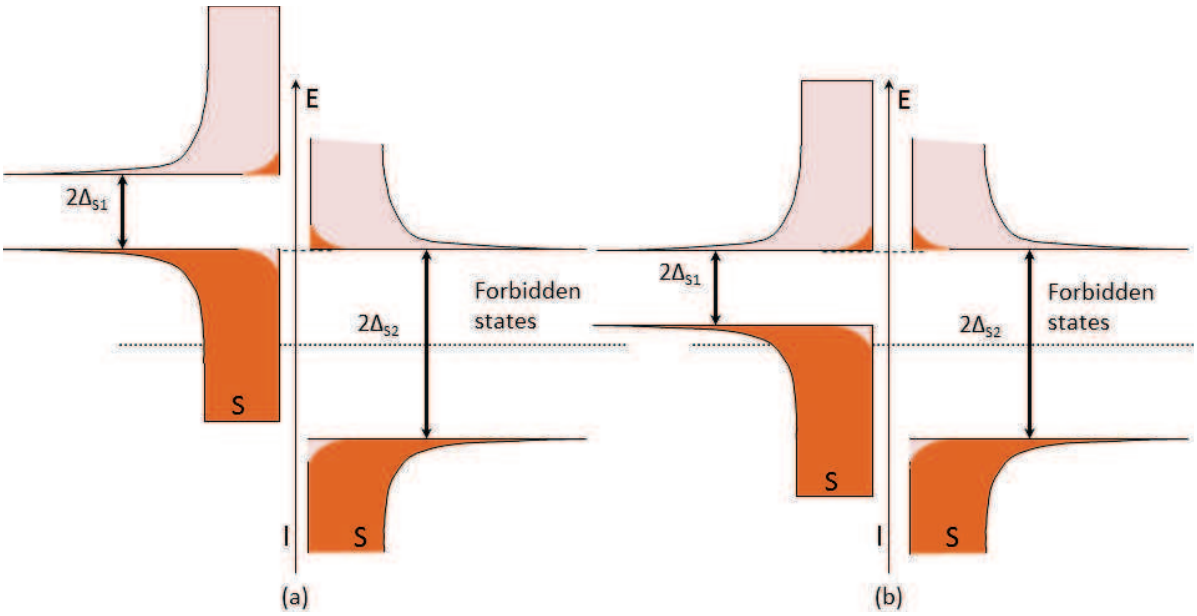

Figure 1.2.6: *Energy diagram of a S_1-I-S_2 junction: (a) A $T > 0$ with voltage bias $V \lesssim \frac{\Delta_{S_2}+\Delta_{S_1}}{e}$ (b) A $T > 0$ with voltage bias $V \lesssim \frac{\Delta_{S_2}-\Delta_{S_1}}{e}$*

to calculate the heat transfer between the two elements of the junction, we can remove a factor of the electrical charge e associated with each tunneling event, and replace it with the energy quantity deposited in the normal metal or the superconductor from a single tunneling event: E- eV.

1.2.3.1 Heat current in Normal metal 1 - Insulator - Normal metal 2

Let us bias a N-I-S junction at a voltage V, corresponding to a total work done of $IV = \frac{V^2}{R_N}$. Following Figure 1.2.3, we first calculate the energy deposited in N_1:

$$\begin{aligned}\dot{Q}_{N_1} &= \dot{Q}_{N_1\to N_2} - \dot{Q}_{N_2\to N_1} \\ &= \tfrac{1}{e^2R_N}\int_{-\infty}^{+\infty} dE\,(E-eV)\,\{f_1(E-eV)\,[1-f_2(E)] - f_2(E)\,[1-f_1(E-eV)]\} \\ &= \tfrac{1}{e^2R_N}\int_{-\infty}^{+\infty} dE\,(E-eV)\,\{f_1(E-eV) - f_2(E)\} = -\tfrac{V^2}{2R_N}\end{aligned} \tag{1.2.17}$$

Similarly we can calculate the the heat deposited in N_2:

$$\begin{aligned}\dot{Q}_{N_2} &= \dot{Q}_{N_2\to N_1} - \dot{Q}_{N_1\to N_2} \\ &= \tfrac{1}{e^2R_N}\int_{-\infty}^{+\infty} dE\,E\,\{f_2(E)\,[1-f_1(E-eV)] - f_1(E-eV)\,[1-f_2(E)]\} \\ &= \tfrac{1}{e^2R_N}\int_{-\infty}^{+\infty} dE\,E\,\{f_2(E) - f_1(E-eV)\} = -\tfrac{V^2}{2R_N}\end{aligned} \tag{1.2.18}$$

So the work applied to bias the junction is entirely and equally dissipated on both side of the junction.

1.2.3.2 Heat current in Normal metal - Insulator - Superconductor junction

Let us consider the more interesting case of the N-I-S junction [50]. The heat deposited in the Normal metal is the difference of energy transfer rate between the Normal metal and the Superconductor, described in Figure 1.2.5:

$$\begin{aligned} \dot{Q}_N &= \dot{Q}_{N\to S} - \dot{Q}_{S\to N} \\ &= \frac{1}{e^2 R_N}\int_{-\infty}^{+\infty} dE\,(E-eV)\,\frac{|E|}{\sqrt{E^2\text{-}\Delta^2}}\,\{f_N(E-eV) - f_S(E)\} \end{aligned} \tag{1.2.19}$$

where negative power means that the heat is taken out from the Normal metal. If we calculate the heat deposited in the superconductor, we find that:

$$\begin{aligned} \dot{Q}_S &= \dot{Q}_{S\to N} - \dot{Q}_{N\to S} \\ &= \frac{1}{e^2 R_N}\int_{-\infty}^{+\infty} dE\,E\,\frac{|E|}{\sqrt{E^2\text{-}\Delta^2}}\,\{f_S(E) - f_N(E-eV)\} \end{aligned} \tag{1.2.20}$$

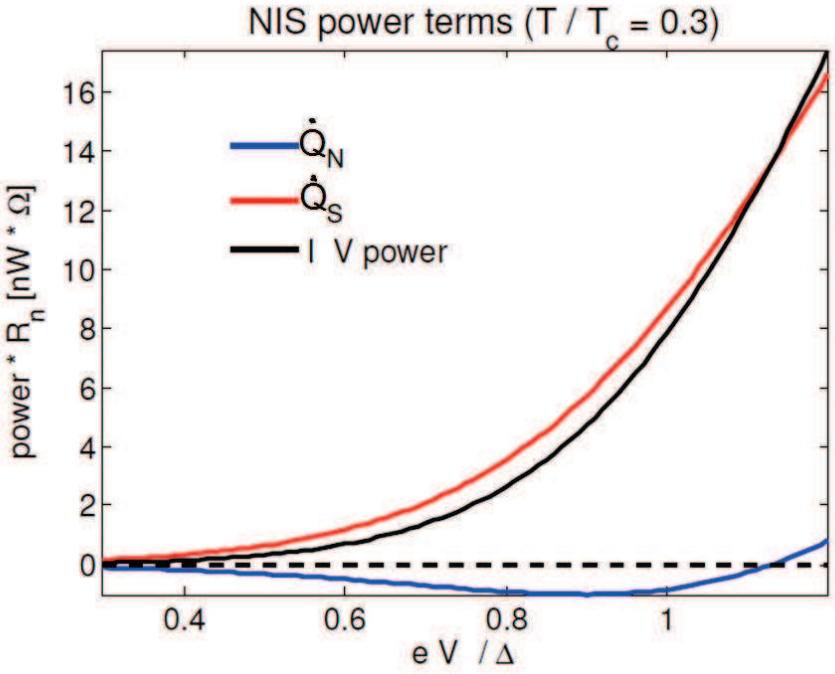

Figure 1.2.7: *Power deposited in the Normal metal, or in the Superconductor in an N-I-S junction under voltage.*[46]

Comparing to the $N_1 - I - N_2$ case, the electrical work supplied enables one to extract selectively high-energy quasi-particles out of the normal metal and deposit them in the superconductor as quasi-particle excitations (for $V \lesssim \frac{\Delta}{e}$). The removal of those hot electrons cools the metal electrode in a manner analogous to cooling a cup of coffee by evaporation [60]. Here the BCS DOS acts as an energy filter. When the junction is

biased close to the gap voltage, only electrons occupying states above the Fermi energy in the normal metal can tunnel through the barrier. As shown in Figure 1.2.7, the sum of the heat extracted from normal metal and the heat deposited in superconductor gives the Joule power of biasing the junction, so the power relation is : $IV = \dot{Q}_N + \dot{Q}_S$.
The first demonstration of the electronic micro-cooling principle, with an electronic cool-down of 15 mK, was realized by Nahum et al. [50].
It was afterwards noticed by Leivo et al. [40] that, contrary to the charge current that is odd relative to voltage polarization, the heat current is symmetric in polarization. This symmetry property helps to double the cooling power by replacing a N-I-S junction with a S-I-N-I-S junction. In Leivo et al. device made with Aluminum as S and Copper as N, electrons are cooled to 100 mK starting from 300 mK with a cooling power of 1.5 pW, see Figure 1.2.8.

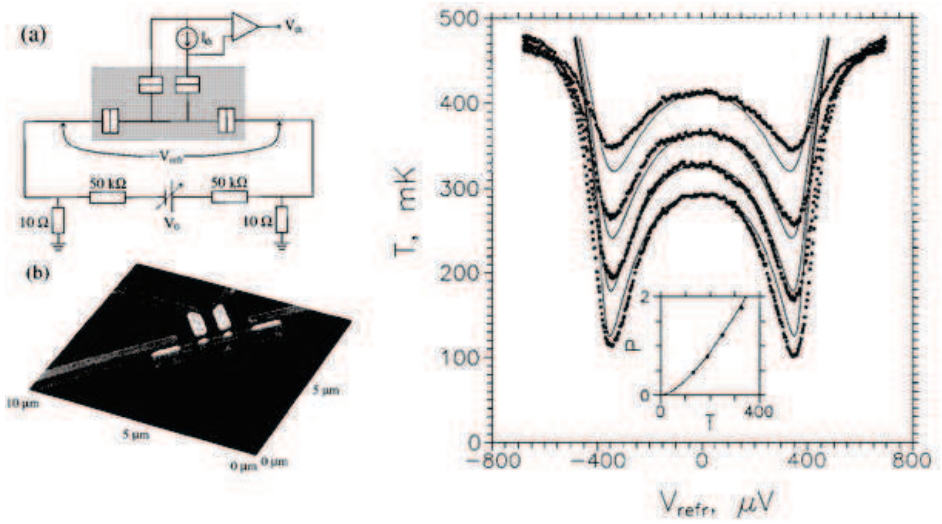

Figure 1.2.8: *First S-I-N-I-S micro-cooler [40]: SEM image of the sample and T_e vs V*

1.2.3.3 Heat current in Superconductor 1 - Insulator - Superconductor 2 junction

Let us consider the case of a $S_1 - I - S_2$ junction. The heat deposited in the S_2 is the difference of energy transfer rate between S_1 and S_2, matching the case described in Figure 1.2.6:

$$\begin{aligned}\dot{Q}_{S_1} &= \dot{Q}_{S_1 \to S_2} - \dot{Q}_{S_2 \to S_1} \\ &= \frac{1}{e^2 R_N} \int_{-\infty}^{+\infty} dE\,(E - eV) \frac{|E-eV|}{\sqrt{E^2\text{-}\Delta_{S_1}{}^2}} \frac{|E|}{\sqrt{E^2\text{-}\Delta_{S_2}{}^2}} \{f_{S_1}(E - eV) - f_{S_2}(E)\}\end{aligned} \tag{1.2.21}$$

where negative power means that heat is taken out from S_1. If we calculate the heat deposited in the S_2 we find that:

$$\begin{aligned}\dot{Q}_{S_2} &= \dot{Q}_{S_2\to S_1} - \dot{Q}_{S_1\to S_2} \\ &= \frac{1}{e^2 R_N}\int_{-\infty}^{+\infty} dE\, E \frac{|E-eV|}{\sqrt{E^2-\Delta_{S_1}{}^2}} \frac{|E|}{\sqrt{E^2-\Delta_{S_2}{}^2}} \{f_{S_2}(E) - f_{S_1}(E-eV)\}\end{aligned} \tag{1.2.22}$$

Indeed Manninen et al. [44] extended electronic refrigeration to a superconductor with a $S_1 - I - S_2 - I - S_1$ junction, where S_2 was Titanium, cooled down by a tunnel junction with aluminum= S_1. The cooling power characteristics appears as different from a $S - I - N - I - S$ cooler. The authors succeeded to cool the Titanium island with a $T_{c_2} = 0.51\,K$ from $1.02\,T_{c_2}$ down to $0.7\,T_{c_2}$.
More recently, on the same principle, Quaranta et al. [67] fabricated a cooler of V-I-Al-I-V, see Figure 1.2.9, cooling Aluminum from 1 K down to 400 mK.

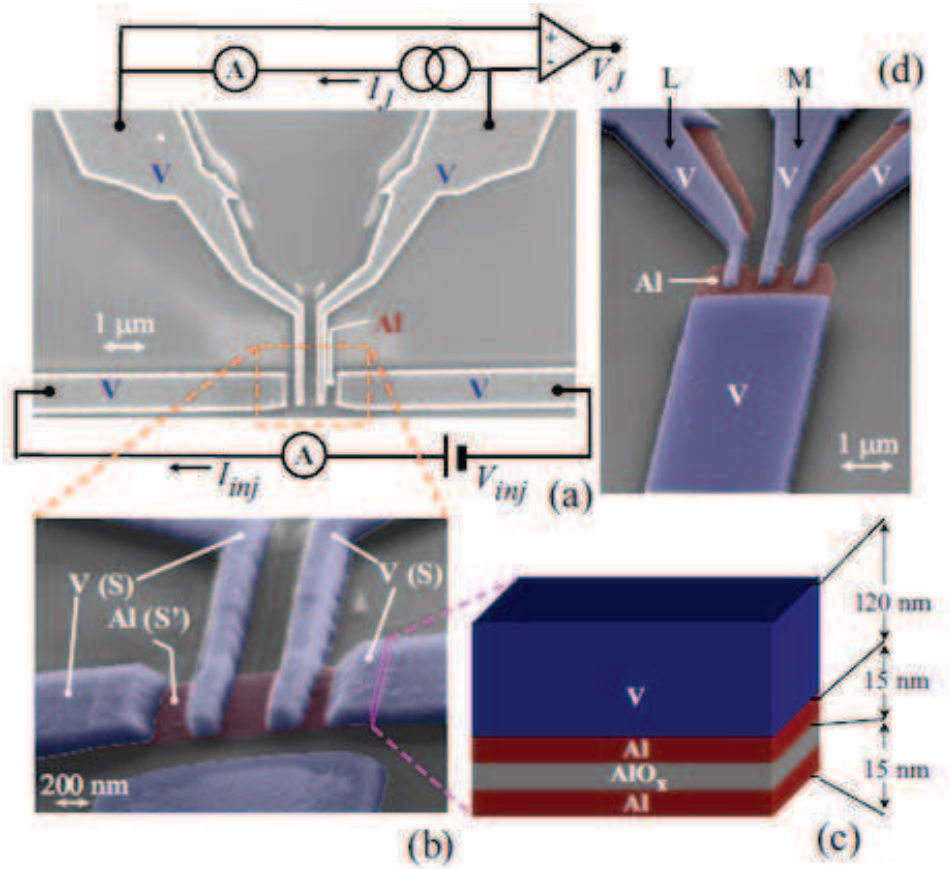

Figure 1.2.9: *Vanadium-Aluminum-Vanadium micro-cooler* [67]

1.2.4 Towards a maximum cooling power

Parameter dependance

For each bath temperature T_{bath}, there is an optimal cooling power $P_{cool}^{max} \equiv \dot{Q}_N^{min}$. In the low temperature limit, $T_e < T_S \ll \Delta/k_B$, the optimum voltage V_{opt} is given by:

$$V_{opt} \simeq \frac{\Delta - 0.66 k_B T_e}{e} \tag{1.2.23}$$

When the junction is biased close to the gap voltage, only electrons occupying states above the Fermi energy in the normal metal can tunnel through the barrier. The removal of those hot electrons cools the metal electrode in a manner analogous to cooling a cup of coffee by evaporation [60]. The optimum voltage V_{opt} is reached when the «hotter electrons» carrying the highest energy have access to unoccupied states of the superconductor, just above the gap.
The charge current flowing through a N-I-S junction at the optimum bias V_{opt} can be approximated as:

$$I_{opt} \approx \frac{\Delta}{eR_N}\sqrt{\frac{k_B T_e}{\Delta}} \tag{1.2.24}$$

According to Ref. [41, 39], it corresponds to a maximum power of:

$$P_{max} = \frac{\Delta^2}{e^2 R_N}\left[0.59\left(\frac{k_B T_e}{\Delta}\right)^{3/2} - \sqrt{\frac{2\pi k_B T_S}{\Delta}} e^{-\frac{\Delta}{k_B T_S}}\right] \tag{1.2.25}$$

We see that the different parameters as T_{bath}, R_N, and Δ affect the efficiency of the electronic refrigeration. The cooling power increases as tunnel resistance R_N decreases. However $R_N \propto 1/\boldsymbol{T}A$ where $\boldsymbol{T}$ is the tunnel barrier transparency and A the junction area. If we increase the transparency of the barrier, leakage sub-gap currents can appear, as described in the next section, and prevent an efficient cooling. Thus the practical solution is to increase junction surface. However scaling-up tunnel junction size means increasing the probability to have pin-holes in the tunnel barrier, leading to sub-gap current leakage. One direction to solve this problem is use epitaxial thin films.

Sub-gap current leakage

Most of N-I-S junctions exhibit a leakage current when biased below the gap (sub-gap) especially at very low temperature. A leakage current is identified by a saturation of the conductance at sub-gap voltage. Usually, the two different ways used to account for the observed sub-gap leakage are the Dynes smearing and a parallel leakage resistance.
– Dynes smearing

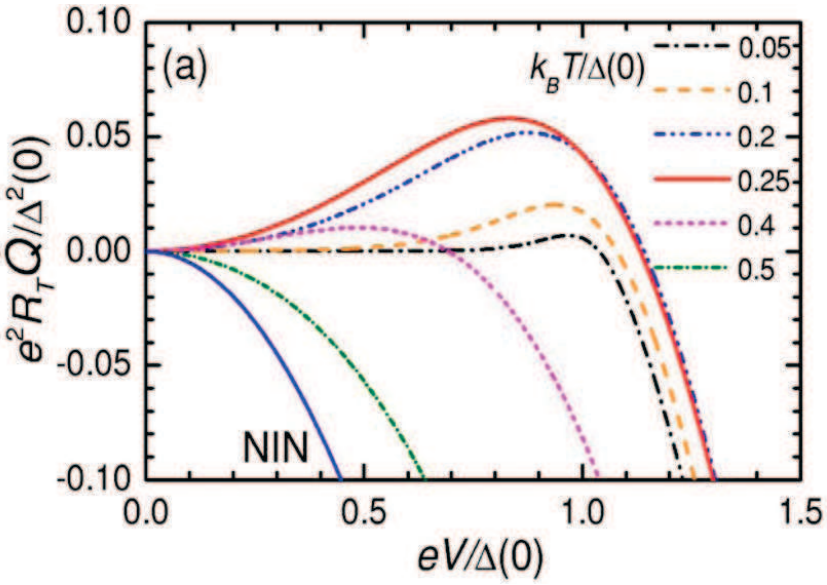

Figure 1.2.10: *Influence of bath temperature on the cooling power*

Dynes et al. [17] introduced a modification of the BCS density of states function that smears it and allow for states below the gap. The modified superconductor DOS with the Dynes parameter γ is expressed as:

$$N_s(E, \gamma) = Re\left[\frac{|E - i\gamma|}{\sqrt{(E - i\gamma)^2 - \Delta^2}}\right] \tag{1.2.26}$$

The additional imaginary term reduces the peak at the gap edge and adds sub-gap states, but does not change the total number of states. Recent investigations [58] on the origin of the Dynes parameter showed that the effectiveness of the fit using Dynes DOS actually originates from the influence of the electromagnetic environment of a tunnel junction, and does not necessarily indicate a property of the superconductor itself.

– Parallel leakage detector

Non-ideal junctions can also be modeled as an N-I-S junction of normal resistance R_{leak} in parallel with a leakage normal resistor R_{leak}. This is equivalent to adding a constant offset to the DOS.

1.2.5 Perspectives of electronic cooling

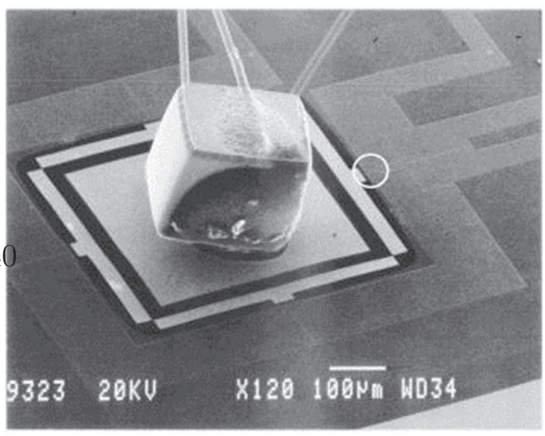

Using N-I-S junctions, Clark et al. demonstrated the refrigeration a bulk object [12] from 320 mK down to 225 mK, see Fig. *1.2.11*. The object was a bulk ger-

manium detector glued on a metallic island deposited on a SiN membrane. The metallic island thermalized phonons and electrons to the same temperature. Each corner of the membrane included a N-I-S cooler junction extended by metallic cold fingers onto the membrane.
In a mesoscopic device realized on a bulk SiO_2 substrate depicted on Fig. 1.2.12a, Rajauria et al. demonstrated that the electronic cooling performance was enhanced by phonon cooling [70].
Figure 1.2.12b shows the plot of the measured electron temperature and the theoretical electron temperature T_e (continuous line) and phonon temperature T_{ph} (dashed line) for different bath temperature T_{bath}= 275, 470, and 570 mK. The nice fit is based on a thermal model taking into account the electron-phonon coupling and the Kapitza coupling, shown on Fig. 1.2.13.

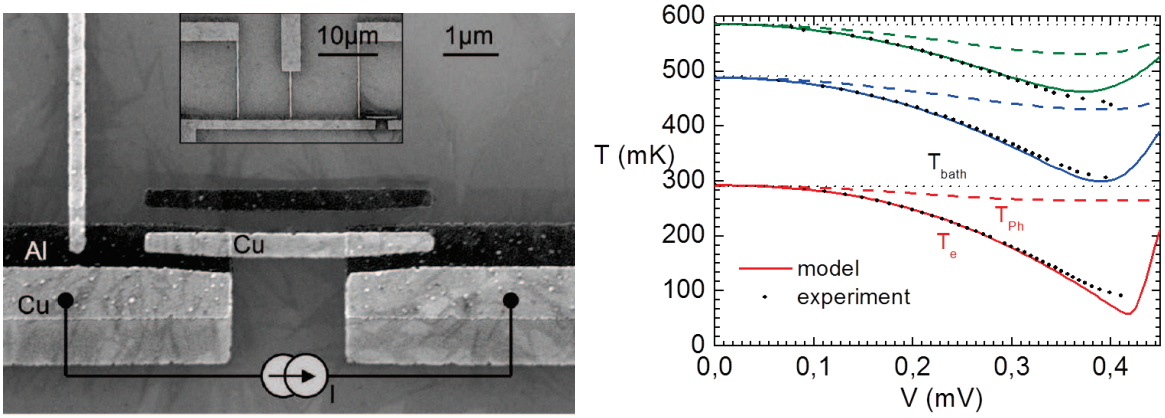

(a) (b)

FIGURE 1.2.12: *(a) SEM image of a micro-cooler with two large area Al-AlOx-Cu cooling junctions in series with external probe thermometer, (b) Dependence of Te (dots) on the cooler bias for different bath temperatures. The full and dashed lines give the calculated electron and phonon temperatures, respectively, obtained from the model for* $\Sigma = 2\ nW\mu m^{-3}K^{-5}$, $KA = 66\ pW\ K^{-4}$.*[70]*

Mesoscopic cooler devices emphasize issues about the different thermal couplings involved in small scale. It is an established fact that at sub-Kelvin temperatures the thermal coupling between conduction electrons and the lattice vanishes [20].

Fundamental questions linked to electronic refrigeration performance, such as quasi-particle relaxation and diffusion in superconductor, Andreev current heat as well as thermal couplings and influence of the system dimension on them are worth to study [34, 32, 35, 31, 33, 36, 28]. In the following section, we will present some of these issues.

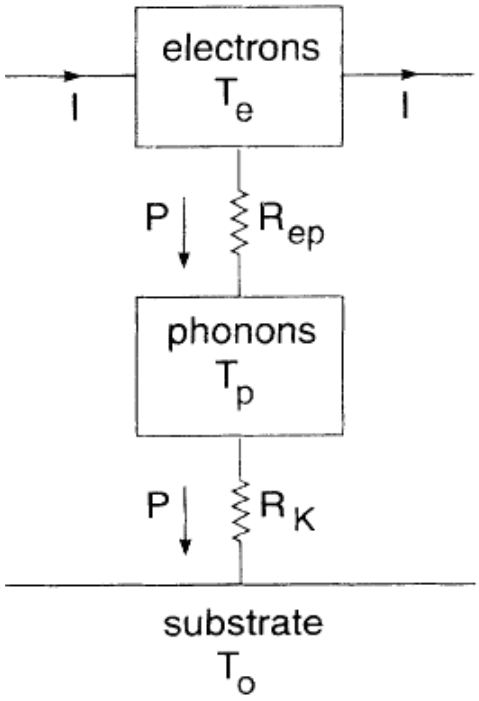

Figure 1.2.13: *From Ref. [95], Coupling between thermodynamic subsystems : Power P dissipated in the electron gas by current I flows into the phonon bath via a thermal resistance R_{ep} mediated by the electron-phonon interaction and then into the electrically insulating substrate via a Kapitza resistance R_K*

1.3 Thermal couplings in a mesoscopic metal

Now that basic N-I-S equations are introduced, we will present the different thermal couplings involving electrons that determine their temperature in the normal metal of an N-I-S junction. At temperatures below 1K, the electron-phonon coupling weakens, which can lead to a significant temperature difference between the electrons and the lattice. This decoupling is actually a necessary condition for electron cooling in an N-I-S junction. We now must treat electrons and phonons as separate populations at different temperatures. Let us recall the different temperature definitions used in this thesis:
T_e= normal metal electron temperature.
T_{ph}= normal metal phonon temperature.

T_S= superconductor temperature.
T_{bath} = bath temperature. The substrate is assumed to be thermalized at the bath temperature.
Hot electron experiments [75, 76, 94, 95, 86], operating at dilution temperature, investigated the electron-phonon scattering rate. They provide information on the electron-phonon coupling in a bulk material that can be compared to theory [72, 95, 80]. The Kapitza resistance was neglected.
The electron-phonon coupling power was demonstrated to follow a T^n law, where $4 \leq n \leq 6$ depending of the purity of the metal, and neglect the Kapitza coupling. Extensive work has been done thermal conductance, and diffusion of electron. More recently work has been done on thermal conductance of membrane, reaching the thermal conductance quanta $K_Q = \frac{\pi k_B^2 T}{6h}$ [79], theoreticalliy predicted [63].
In this chapter we will present a comprehensive thermal model developed by Rajauria et al, completing the hot electron theory to higher temperatures. We first introduce the different component of this model the electron-phonon coupling and Kapitza coupling.

1.3.1 Electron-Electron interaction

Extracting a temperature from a electron population in a Normal metal supposes that they are at thermal quasi-equilibrium. A Normal metal cooled or heated by electron tunneling is, a priori, an out-of-equilibrium situation. Experiments carried by Pothier et al. [64] demonstrated out-of equilibrium electronic distribution in a metallic wire. The electronic energy distribution equilibrates towards a Fermi distribution by electron-electron inelastic scattering. Then the electron-phonon coupling thermalizes the electron population to the phonon temperature of the metal. Hence, different cases appear depending of the relative values of the tunnel injection rate, the electron-electron and electron-phonon scattering rates:
– if the electron-electron scattering rate and the electron-phonon scattering rate are smaller than the injection rate, the electronic population follows a non-equilibrium distribution, staircase-shaped, instead of the usual Fermi function, that is gate shaped.
– if the electron-electron scattering rate is larger than the injection rate, the electron distribution can be described as an equilibrium Fermi function $f_e(E, T_e)$. Then depending of the electron-phonon rate compared to the electron-electron scattering rate; electrons are at equilibrium $T_e = T_p$ if electron-phonon scattering rate is larger than electron-electron scattering, otherwise electrons are at quasi-equilibrium, their distribution being characterized by a T_e different from $T_e = T_p$.
In order to identify the relevant regime, we can first calculate the product $\tau_e\Gamma$, τ_e being the electron relaxation time and Γ is the injection rate. If $\tau_e\Gamma \gg 1$, the distribution function in the normal metal does not follow a Fermi distribution. If $\tau_e\Gamma \ll 1$, the distribution function in the normal metal follows a Fermi distribution, hence we can

define an electronic temperature T_e. The residency time Γ is given by:

$$\Gamma^{-1} = \frac{2}{N_N(E_F)R_N V e^2}, \tag{1.3.1}$$

where V is the volume of the normal metal, R_N is the tunnel resistance, $N_N(E_F)$ is the non-normalized density of states and e is the charge.

1.3.2 Electron-phonon coupling

In this paragraph, we will calculate the energy loss rate between electrons and phonons to end up with the formula of electron-phonon coupling [95], including the degree of power law and the origin of electron-phonon coupling constant Σ.
First to simplify the calculations we consider the following assumptions :

1. Phonons are considered at a temperature (T_{ph}) smaller than the Debye temperature (T_D). Consequently we neglect optical phonons and consider only acoustic phonons. At low energy, they follow a linear dispersion relation $\varepsilon_q = \hbar v_s q$, where q is phonon wave vector. We assume also that the phonon distribution is spatially uniform.
2. Allowed phonon state spectrum is assumed to be the 3D continuum since the metal film's thickness is larger than average phonon wavelength.
3. Electron-phonon coupling is represented by a scalar deformation potential. It implies that we neglect transverse phonons and consider that only longitudinal phonons couple to electrons.

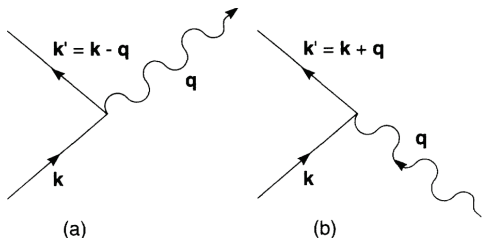

Figure 1.3.1: (a) Emission of a phonon (b) Absorption of a phonon

The energy transfer process from electrons to phonons is represented in Figure 1.3.1. By emitting or absorbing a phonon at wave vector q and energy ε_q, an electron at wave vector k and energy E_k changes, respectively, to wave vector $k' = k - q$ or $k' = k + q$ and energy $E_{k'}$. The process is considered inelastic since Umklapp process is neglected. Applying the Fermi's golden rule formula, we write the rate of phonon emission process, which is proportional to the density of final states:

$$\tau^{-1}_{k,k-q} = \frac{2\pi}{\hbar} M^2 \delta(E_k - E_{k'} - \varepsilon_q)[1 - f(E_{k'})][n(q) + 1], \tag{1.3.2}$$

where $M^2 = (\hbar q/2\rho v_s \Omega)(2\varepsilon_F/3)^2$ is the square of the matrix element of electron-phonon coupling, ρ is the mass density, Ω is the volume of the metal, ε_F is the Fermi energy, $f(E_k) = (e^{\beta_e E_k} + 1)^{-1}$ is the Fermi-Dirac distribution for the electron, $n(q) = (e^{\beta_{ph}\varepsilon_q} - 1)^{-1}$ is the Bose-Einstein distribution for the phonons with $\beta_i \equiv (k_B T_i)^{-1}$. The factor $(1 - f)$ is the probability that the final electron state is empty and the factor $(n + 1)$ accounts for the stimulated and spontaneous emission rate for the phonons. The rate at which the electron looses energy in this transition can be written as $\varepsilon_q \tau^{-1}_{k,k-q}$.
The electrons transfer energy to phonons at the rate:

$$P_e = \int dE_k N(E_F) f(E_k) \int d^3q D_p(q) \varepsilon_q \tau^{-1}_{k,k-q}. \tag{1.3.3}$$

Here $D_q(q)$ is the phonon density of states, in general for 3D phonons $D_q(q) = V/(2\pi)^3$ with V the volume of the system and $N(E_F)$ is the density of states for electrons at the Fermi level.

$$P_e = \frac{V}{\hbar(2\pi)^2} \int dE_k N(E_F) f(E_k) \int d^3q M^2 \varepsilon_q \delta(E_k - E_{k-q} - \varepsilon_q)[1 - f(E_{k-q})][n(q) + 1], \tag{1.3.4}$$

Correspondingly, electrons absorb energy from phonons at the rate:

$$P_a = \frac{V}{\hbar(2\pi)^2} \int dE_k N(E_F) f(E_k) \int d^3q M^2 \varepsilon_q \delta(E_k - E_{k+q} - \varepsilon_q)[1 - f(E_{k+q})] n(q), \tag{1.3.5}$$

Net heat flux between electrons and phonons can be expressed as:

$$\dot{Q} = P_e - P_a, \tag{1.3.6}$$

We integrate over the angle θ between the electron and the phonon wave vectors. In spherical coordinates, $\int d^3q \to 2\pi \int_0^\infty dq q^2 \int_{-1}^1 d(cos\theta)$. Moreover, we consider $k \simeq k_F$ and $q \ll k_F$ that leads to the approximation $E_{k\mp q} = \frac{\hbar^2(k\mp q)^2}{2m} \simeq E_k \mp \frac{\hbar^2 k_F}{m} q\cos\theta$ with $E_k = \frac{\hbar^2 k^2}{2m}$.
We rewrite Expression 1.3.4 considering these last remarks:

$$\begin{aligned} P_e = \tfrac{V}{\hbar 2\pi} \quad & \int dE_k N(E_F) f(E_k) \int_0^\infty dq q^2 M^2 \varepsilon_q \int_{-1}^1 d(\cos\theta) \delta(\tfrac{\hbar^2 k_F}{m} q\cos\theta - \varepsilon_q) \\ & \times [1 - f(E_k - \tfrac{\hbar^2 k_F}{m} q\cos\theta)][n(q) + 1] \end{aligned} \tag{1.3.7}$$

$$P_e = \frac{mV}{k_F \hbar^3 2\pi} \int dE_k N(E_F) f(E_k) \int_0^\infty dq q^2 M^2 \varepsilon_q [1 - f(E_k - \varepsilon_q)][n(q) + 1], \tag{1.3.8}$$

Remembering assumption 3 implies $M^2 = M_0^2 q$, we write $\varepsilon \equiv \varepsilon_q = \hbar v_s q$, we drop the

index k and obtain:

$$P_e = \frac{mVM_0^2N(E_F)}{k_F\hbar^6v_s^3 2\pi}\int dEf(E)\int_0^\infty d\varepsilon\varepsilon^3[1-f(E-\varepsilon)][n(q)+1], \tag{1.3.9}$$

Similarly we re-express Eq. 1.3.5:

$$P_a = \frac{mVM_0^2N(E_F)}{k_F\hbar^6v_s^3 2\pi}\int dEf(E)\int_0^\infty d\varepsilon\varepsilon^3[1-f(E+\varepsilon)]n(q), \tag{1.3.10}$$

Considering Eqs 1.3.9 and 1.3.10, expression 1.3.6 of the net heat flux between electron and phonon gives:

$$\dot{Q} = \frac{mVM_0^2N(E_F)}{k_F\hbar^6v_s^3 2\pi}\int_0^\infty d\varepsilon\varepsilon^3\Big\{\int_{-\infty}^{+\infty} dEf(E)[1-f(E-\varepsilon)] + n(q)\Big[\int_{-\infty}^{+\infty} dEf(E)[1-f(E-\varepsilon)] - \int_{-\infty}^{+\infty} dEf(E)[1-f(E+\varepsilon)]\Big]\Big\} \tag{1.3.11}$$

Using the identity the symmetry property $f(-E) = 1-f(E)$, and $\int_{-\infty}^{+\infty} dE[f(E)-f(E+\varepsilon)] = \varepsilon$, expression 1.3.11 simplifies into :

$$\dot{Q} = \frac{mVM_0^2N(E_F)}{k_F\hbar^6v_s^3 2\pi}\int_0^\infty d\varepsilon\varepsilon^4\left\{\frac{1}{e^{\beta_e\varepsilon}-1} - \frac{1}{e^{\beta_{ph}\varepsilon}-1}\right\}, \tag{1.3.12}$$

Integrated over the energy the expression becomes :

$$\dot{Q} = \frac{12\varsigma(5)mVM_0^2N(E_F)}{k_F\hbar^6v_s^3 2\pi}(\beta_e^{-5} - \beta_{ph}^{-5}), \tag{1.3.13}$$

It amounts to the well-known expression :

$$P_{el-ph} = \Sigma V(T_e^5 - T_{ph}^5) \tag{1.3.14}$$

where, by identification,

$$\Sigma = \frac{12\varsigma(5)mM_0^2N(E_F)k_B^5}{k_F\hbar^6v_s^3 2\pi} \tag{1.3.15}$$

Here we have demonstrated the power law and the expression of Σ in electron-phonon coupling in a bulk material, since we consider 3D phonons. Nevertheless, a more complete theory of electron-phonon coupling in a pure metal, developed by Reizer [73], has been extended to impure metals [80], taking into account quantum interference due to static impurities. Considering the different regimes (i.e. amount of disorder, tempera-

ture), the most general expression of electron-phonon thermopower would be:

$$P_{e-ph} = \Sigma_n V(T_e^n - T_{ph}^n) \tag{1.3.16}$$

where V is the volume of normal metal, $4 \leqslant n \leqslant 6$, and $\Sigma_n \sim 1\text{nW.}\mu\text{m}^3 K^n$ is the material-dependent electron-phonon coupling constant. A criteria to define the different regimes, presented on Table 1.1, is based on the product of the dominant thermal phonon wave vector $q_T = 4k_B T/\hbar c$, c being the sound velocity, and the elastic electron mean free path l. Furthermore Σ_n is approximated to $1/c^{n-1}$.

$q_T l \to \infty$	pure limit	$n = 5$
$q_T l > 1$	clean limit	$4 < n < 5$
$q_T l < 1$	impure/dirty limit	$4 < n < 6$

Table 1.1: Electron-phonon coupling regimes in a bulk metal

Using this consideration, Underwood et al. [91] investigated the influence of substrate on electron-phonon coupling. Their experiment consists on an hot electron experiment on two different substrates: silicon and silicon oxide. In their study, they heated a normal metal, and measure the IV characteristics of a pair N-I-S junctions placed on the metal as described by the inset in Fig.1.3.2. Then they can extract the electronic temperature T_e from the IV characteristics using Eq. 1.2.11. The experimental data is then fitted to Eq. 1.3.16. Finally n and Σ versus T_e are plotted in Fig. 1.3.2, featuring no important difference on behaviour between the different substrates. However, we notice a decrease of the exponent as the bath temperature increase. Contrary to Al:Mn that contains a high concentration of impurities, in a bulk copper the electron-phonon coupling follows a power law such that $n = 5$ and $\Sigma_5 \sim 2\text{nW.}\mu\text{m}^{-3} K^{-5}$[35].

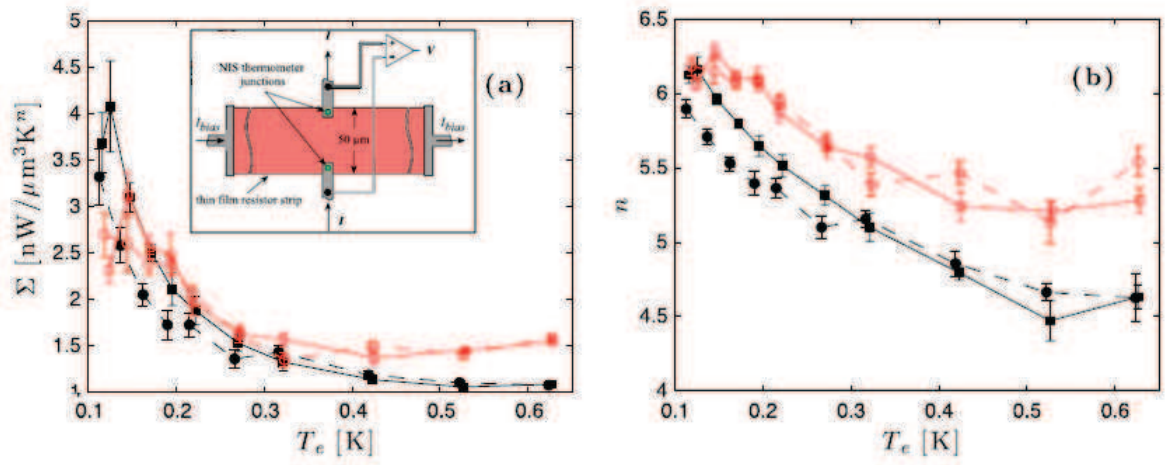

Figure 1.3.2: *Experiment Ref. [91]: evolution of (a) measured Σ and (b) n vs electron temperature T_e for Al:Mn resistors on Si (red, open symbols) and SiO2 (black, filled symbols) substrates. The dashed and solid lines for each color represent different samples from the same wafer. Inset: Schematic of NIS thermometer/heater device and measurement arrangement. Red resistor strip is Al: Mn. Gray current injection electrodes are superconducting Al. The resistor length is 500 μm.*

1.3.3 Kapitza coupling

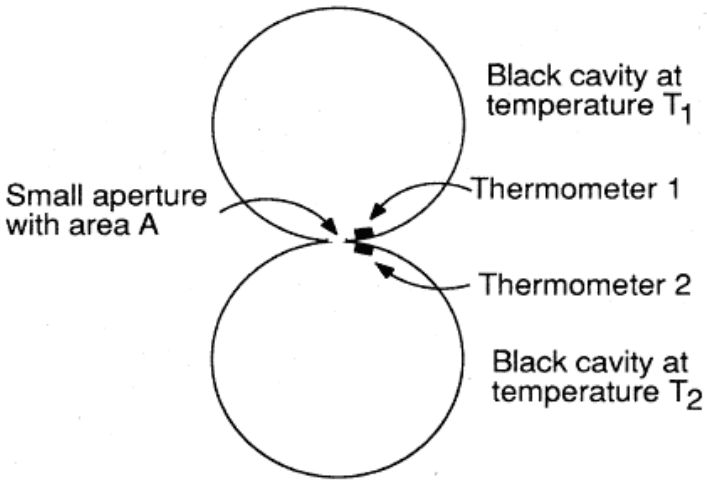

Figure 1.3.3: *Simple model for Kapitza coupling calculation [87].*

At the boundary between two materials with different densities and sound speeds, phonons traveling towards the boundary will be reflected and refracted. To calculate

Kapitza coupling, we simplify the problem to two bosonic populations at two different temperatures in interaction. The interaction can be written as a relaxation of the N metal phonons to the substrate phonons with a characteristic time $\tau_{ph-subst} = {}^{\eta d}/_{v_s}$ where v_s is the velocity of sound in the N-metal, d is the thickness of the N-metal and η is a numerical factor (<1), which accounts for the lattice mismatch between the two materials [87]. At thermal equilibrium, we can calculate the power exchanged between N-metal normal phonons bath, characterized by a distribution n_q, and an effective phonon temperature T_{ph}, and the substrate phonons bath following a distribution $n_q(T_{bath})$:

$$P_{ph-subst} = \int d^3q D_p(q) \varepsilon_q \tau^{-1}_{ph-subst}(n_q(T_{ph}) - n_q(T_{bath})), \tag{1.3.17}$$

Similarly to electron-phonon coupling, $D_q(q) = V/(2\pi)^3$ is the 3D-phonon density of states with V being the volume of the system and $n_q(T_i) = (e^{\beta_i \varepsilon_q} - 1)^{-1}$ the Bose-Einstein distribution for the phonons with $\beta_i \equiv (k_B T_i)^{-1}$. Considering the same assumptions as paragraph 1.3.2 we re-write expression 1.3.17 as:

$$P_{ph-subst} = \frac{Ad}{2\pi^2} \frac{v_s}{\eta d} \int dq q^2 \varepsilon_q (n_q(T_{ph}) - n_q(T_{bath})), \tag{1.3.18}$$

$$P_{ph-subst} = \frac{A}{2\pi^2} \frac{1}{\eta \hbar^3 v_s^2} \int_0^\infty d\varepsilon \left(\frac{\varepsilon^3}{e^{\varepsilon/k_B T_{ph}} - 1} - \frac{\varepsilon^3}{e^{\varepsilon/k_B T_{bath}} - 1} \right), \tag{1.3.19}$$

We change variable from ε to $x = \frac{\varepsilon}{k_B T}$:

$$P_{ph-subst} = \frac{A}{2\pi^2} \frac{1}{\eta \hbar^3 v_s^2} \left[(k_B T_{ph})^4 \int_0^\infty dx \frac{x^3}{e^x - 1} - (k_B T_{bath})^4 \int_0^\infty dx \frac{x^3}{e^x - 1} \right], \tag{1.3.20}$$

We integrate and we obtain an expression similar to Kapitza coupling:

$$P_{ph-subst} = A \frac{k_B^4 \pi^4}{30 \pi^2 \eta \hbar^3 v_s^2} (T_{ph}^4 - T_{bath}^4), \tag{1.3.21}$$

The above expression does not depend of N-metal thickness, but only on the area A of the interface. By identification, we obtain $K = \frac{k_B^4 \pi^2}{30 \eta \hbar^3 v_s^2}$ depending of parameters v_s and η. If we assume $\eta = 1$ and in copper $v_s = 4400\ m/s$, we obtain a constant $K \sim 550\,\mathrm{pW\mu m^{-2}K^{-4}}$. The coefficient η is a phenomenological parameter depending on the two materials and quality of the interface. Indeed we can write:

$$P_{ph-subst} \equiv P_{Kapitza} = AK(T_{ph}^4 - T_{bath}^4), \tag{1.3.22}$$

This approach is simplistic, and open to criticism. Indeed, we consider the power ex-

changed between two 3D phonon bath at two different temperatures without consideration on the different sound velocity between the two systems. Nevertheless this approach give a good power law T^4 between the different phonon baths, and the dependance to the interface area A.

1.3.4 Andreev heating

Andreev current is due to Andreev reflections, first uncovered by St James and Andreev [1, 77]. Andreev reflection is a second order tunneling process, taking place at N-S interface, where a Normal metal electron is retro-reflected as a hole and creates a Cooper pair in the Superconductor. Blonder, Tinkham and Klapwijk have formulated a theory [10] (BTK theory) for the transport through a N-I-S with the transparency being the main parameter. However many experiments have deviations from BTK predictions, in particular the appearance of a zero bias conductance. Van Wees et. al. [92] gave the first qualitative picture of this zero-bias anomaly by considering the quantum coherence of the electron and the disorder in the electrodes. Fig. 1.3.4 shows the schematic of the N-S junction with disorder/impurities in the electrodes. The electron with energy $E < \Delta$ is incident from N towards the barrier. Since the probability of Andreev reflection is very small, the electron gets mainly specularly reflected from the barrier. Nevertheless, the specularly reflected electron undergoes elastic scattering from impurities (stars in Fig. 1.3.4) leading to trajectories re-directed towards the barrier. The electrons and holes amplitures are opposite and therefore adds coherently. Therefore, disorder increases the probability of transfer of an electron pair across the N-S junction.
Rajauria et al. [69, 5] demonstrated both theoretically, following the Hekking and Nazarov formalism [27], and experimentally that the Andreev current induces dissipation in the normal metal. They showed that the Andreev current can limit the attainable cooling significantly even at the optimum bias point. In this effect, the phase-coherence length L_φ plays a central role, as suggested by NS-SQUID experiment [65]. In all of our differential conductance at dilution temperature a peak rises at low voltage, that is assumed to be due to this phenomena. Recently NIST Boulder group [43] compared the zero bias peaks in the differential conductance from junctions of different resistance and size. Their results confirmed the previous experiment and Hekking and Nazarov theory, namely the current due to Andreev reflections depends on the junction area and the junction resistance area product.
The impurity averaged Andreev current through N-I-S junction can be written as :

$$I_A = \int dE I(E) \left[f\left(\frac{E}{2} - eV\right) - f\left(\frac{E}{2} + eV\right) \right]$$

where $I(E)$ is the spectral current as

$$I(E) = \frac{h}{8e^3\nu(0)} \frac{G_{NN}^2}{N} \left[1 + \frac{N-1}{2}\right] [P_E(0) + P_{-E}(0)]$$

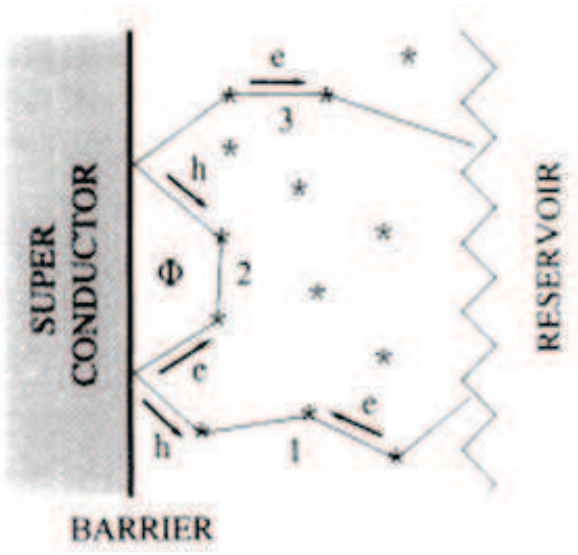

Figure 1.3.4: *Van Wees et. al. qualitative model of the excess conductance in a S-I-N tunnel junction at low temperature. It consists of three sections: the pure superconductor, the pure normal metal reservoir and the section near the junction with impurities.*

The work performed by the current source feeding the circuit with an extra current due to Andreev reflection I_A generates a Joule heat $P_A = -I_A V$ [69, 5]. This induced dissipation due to the Andreev current is deposited entirely in the N metal and does not perturb the superconductor. Hence, the net cooling power of the S-I-N junction due to the tunneling of hot single quasiparticle out of the N metal will be reduced by the Joule heat deposited into N by the Andreev current. The net cooling power of the device is re-defined as, $P_{net} = P_{cool} - P_A$. The Andreev current induced dissipation depends strongly on the temperature and transparency of the junction. For low transparency and at intermediate temperature (T $>$ 300 mK) the phase-coherent Andreev current contribution is negligible in comparison to the single quasiparticle current. Thus the Joule heat dissipation in N-island is small. At very low temperature and low bias, the cooling power is negligible in comparison to the induced Andreev power. The induced dissipation will then subjugate the quasiparticle cooling and lead to heating of the electrons in N-island. Figure 1.3.5 shows the quantitative comparison of the cooling power (P_{cool}) due to single quasiparticle tunneling (red dotted dash line) and the Andreev current (blue dotted line) induced dissipation (P_A) at very low temperature. Due to the absence of quasiparticles, Pcool is almost zero near zero bias and attains its maximum near the gap. However the phase-coherent Andreev current induces the dissipation as a Joule heat ($I_A V$) in the N metal, which increases sharply near the zero bias. At a bias close to the gap voltage, the cooling power out-does the dissipation due to the Andreev current. As Andreev current induced dissipation depends on the transparency of

the junction, it surpasses the single quasiparticle cooling at a varying temperature. For our cooling device with a low transparent tunnel barrier (10^{-5}), the Andreev current dissipation becomes relevant only at low temperature (T < 200 mK).

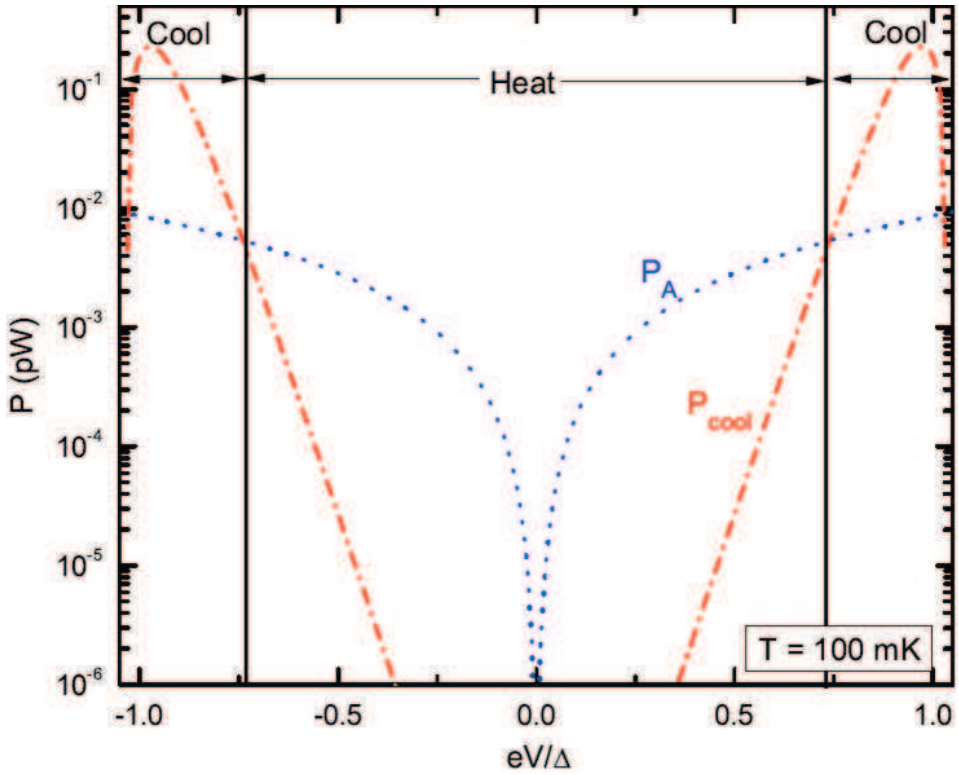

Figure 1.3.5: Calculated power due to quasiparticle cooling (P_{cool}) and the heat dissipation due to Andreev current (P_A) as a function of voltage bias at T_{bath} = 100 mK.

1.3.5 Photon heat channel

In 2004, Meschke et al. [45] demonstrated, as suggested by Schmidt et al. [78], that at low temperature where electron-phonon coupling and normal electronics heat conduction vanishes, heat is transfer by photon radiation between electrons and their environment. In their experiment, as depicted in Fig. 1.3.6, two normal metal islands are connected to one to the other only via superconducting leads, which are ideal insulators against conventional thermal conduction. Each superconducting lead is interrupted by a switch of electromagnetic radiation in the form of a DC-SQUID (Superconducting QUantum Interferometer Detector, i.e. a superconducting loop with two Josephson tunnel junctions). Meschke et al have studied the heat conduction G_n between the pieces of normal

metal while they modulated the flux flowing through DC-SQUID. They found that the thermal conductance between the two metal islands mediated by photons approaches the expected quantum limit of G_Q for a single mode heat conduction $G_Q = \frac{\pi k_B^2}{6h}$ [63].

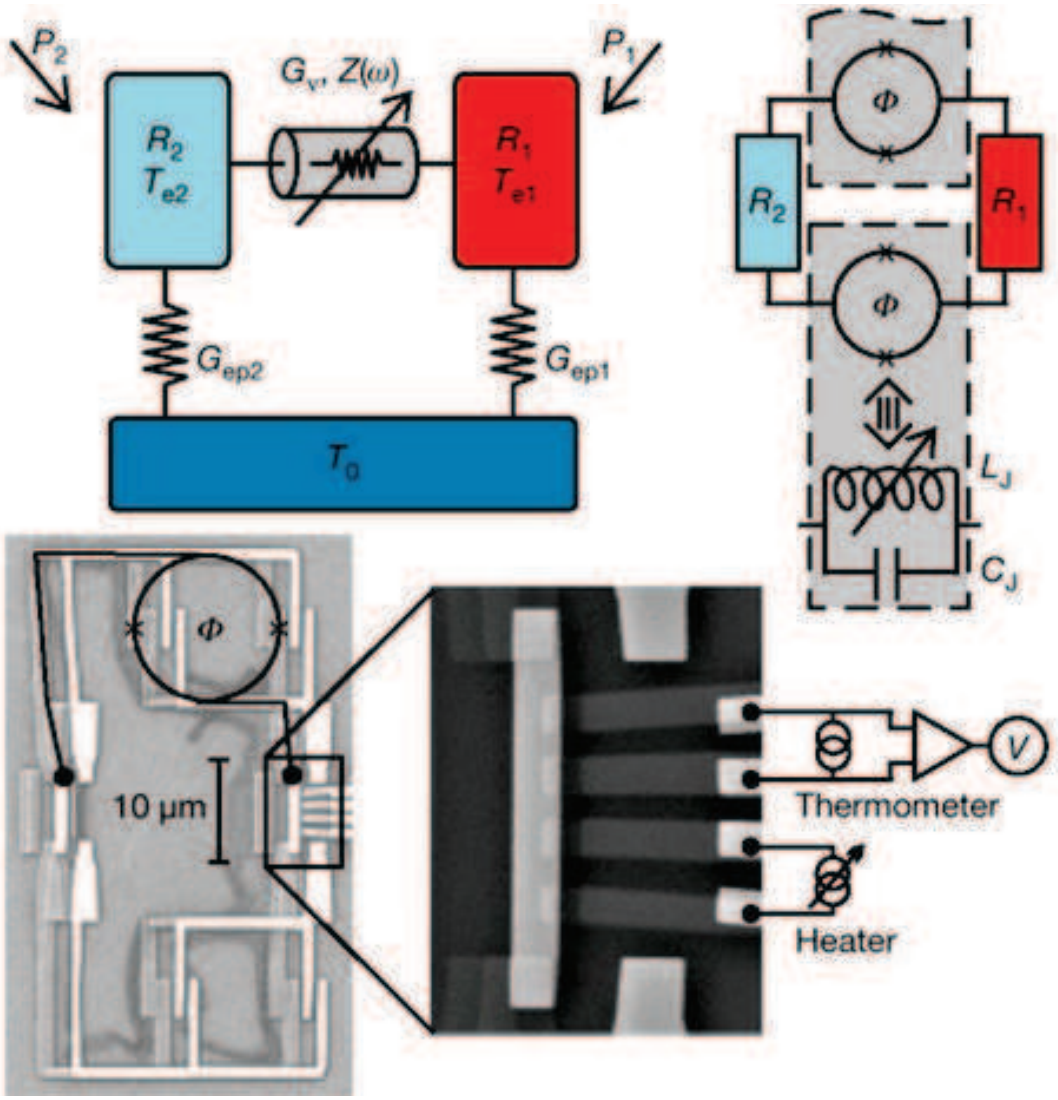

Figure 1.3.6: *Experiment Ref. [45]: at the top, thermal (left) and electrical (right) models; at the bottom, a scanning electron micrograph of the device (left), and a magnified view of resistor 1 with four adjoining NIS and two NS contacts (right)*

More recently, Timofeev et al. [89] demonstrated electronic refrigeration through a photon channel. On the same principle as Ref. [45], they design two N-I-S junctions-based devices, where two resistances at two different temperatures can exchange heat through a superconducting line. As shown in Fig. 1.3.8 in sample A, two normal islands

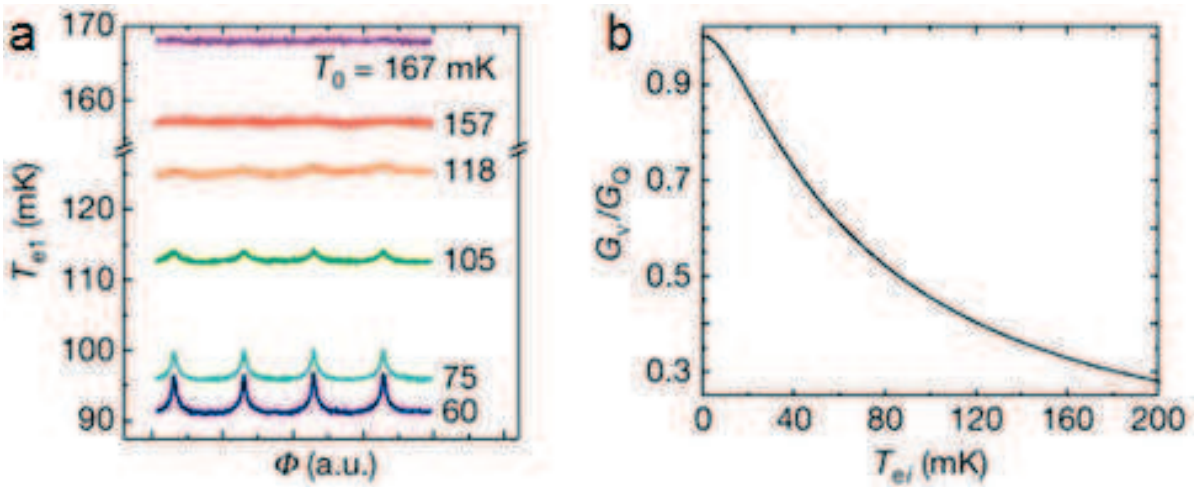

FIGURE 1.3.7: *Experiment Ref. [45] : (a) Flux modulation of T_e recorded at the values of T_{bath} indicated, (b) The ratio of the photonic thermal conductance G_n in the circuit at $\phi = 0$ and the quantum of thermal conductance G_Q as a function of the electron temperature T_e.*

are connected through two surperconducting lines. A contrario, in sample B the normal pieces are connected by only one superconducting line. This creates an impedance mismatch in the circuit closed through the capacitances to the ground of the two metallic islands. In the experiment, the authors have cooled down the electron of one island and measured the electronic temperature of both islands. In sample A with a matched impedance they observed electronic refrigeration of the other island with a matched impedance, whereas the sample B with mismatched impedance showed electronic heating of the other island, see Fig. 1.3.9. It is noteworthy that Timofeev et al. succeeded to observe electronic refrigeration at a 50 µm distance through superconducting leads.

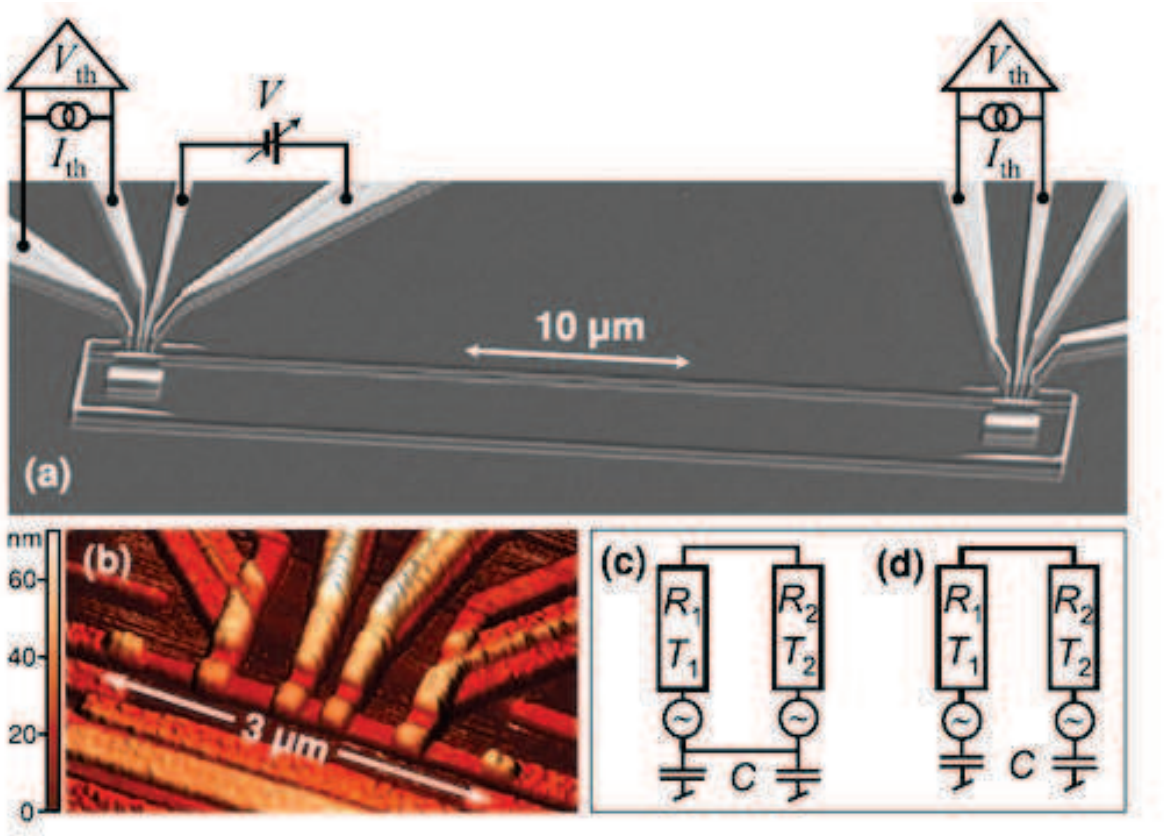

Figure 1.3.8: *Experiment Ref. [89]: (a) Electron micrograph of sample A (matched impedances). Two normal islands are connected with superconducting lines into a loop to match the impedance between them and enable remote refrigeration. (b) Colored atomic force microscopy image of the island. The four NIS junctions, contacting each island in the middle part, are used to perturb and to measure the island temperature. (c) Equivalent electrical circuit of the matched (sample A) and (d) the mismatched (sample B) structures.*

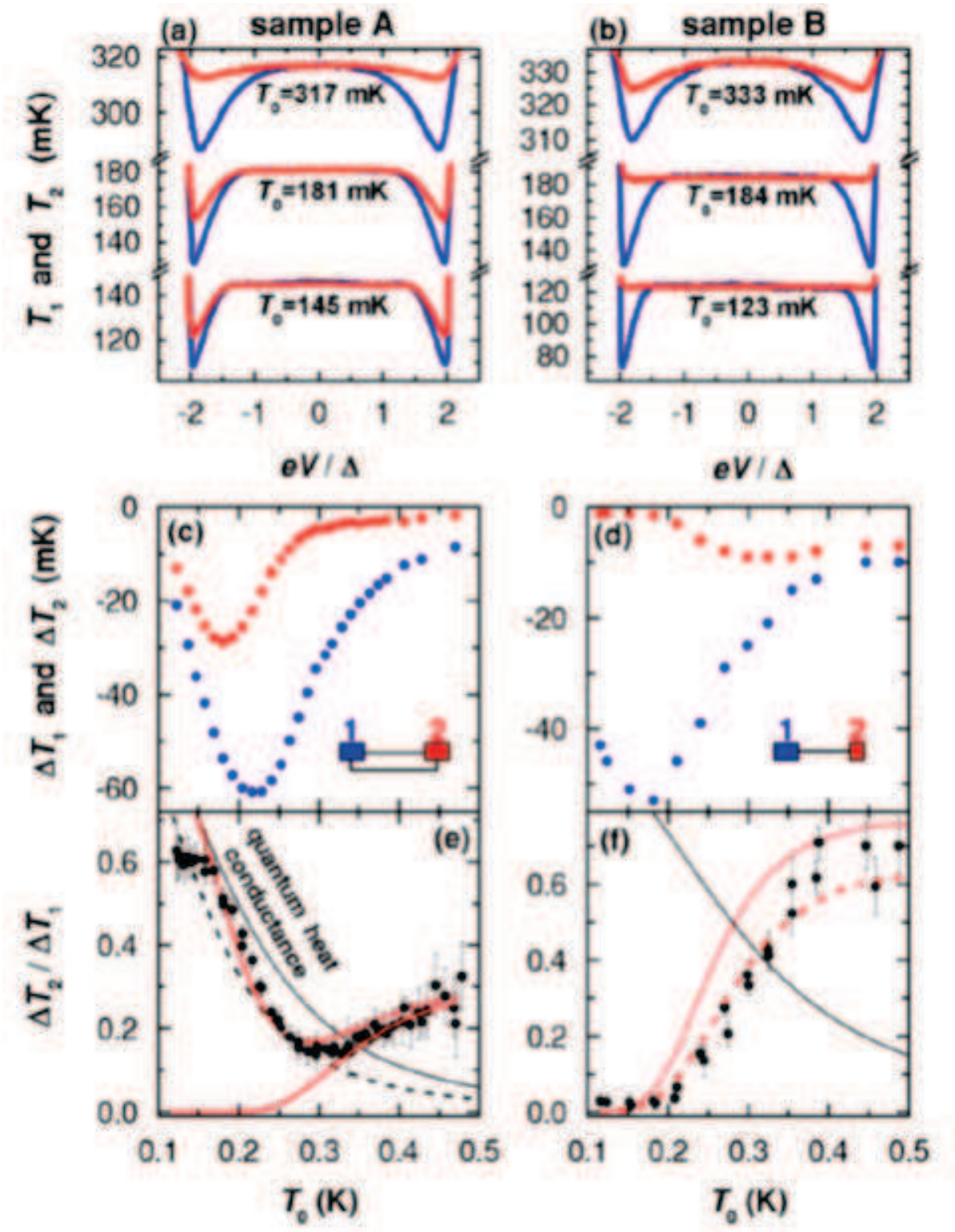

Figure 1.3.9: *Experiment Ref. [89]: Measured data of sample A (a),(c),(e) and sample B (b),(d),(f) and results from the thermal model. (a), (b) Measured island temperatures T_1 (blue line) and T_2 (red line) vs bias voltage V at three bath temperatures T_{bath}. (c),(d) Absolute temperature changes ΔT_1 (blue dots) and ΔT_2 (red dots) measured at T_{bath}= 120–500 mK. (e),(f) Relative temperature changes at T_{bath}= 120–500 mK (dots).*

In another experimental design called the Brownian refrigerator [57, 61] one cold resistor cool down the other one, hotter, due to fluctuations of the resistor. Nevertheless, in this conceptual idea, the authors did not take into account the fact that the hot resistor will heat through photon channel the cold one. Theoretically, Ojanen et al. [54, 53] derived, by applying non-equilibrium Green's function methods, a formally exact Meir-Wingreen-Landauer- type formula of the photon heat exchange between two bodies of different temperature, which is controllable by the circuit coupling them.

1.4 Quasi-particles relaxation

During electronic refrigeration, hot electrons are removed from the Normal metal and injected as quasi-particle excitations into the Superconductor. These quasi-particles can stay close to the tunnel barrier and locally enhance the superconductor temperature.
Pekola et al. [56] demonstrated that a normal metal reservoir close to the barrier, called «quasi-particle trap», helps for quasi-particles excitation relaxation and enhances the electronic refrigeration. Efforts has been made theoretically [93] to understand the decay mechanism of excess quasi-particle population in a superconducting electrode, as well as their diffusion in the superconductor. The out-of-equilibrium electronic population injected at an energy above the gap, relaxes slowly by recombination and pair-breaking. The size of device worsens the effect by restricting the accessible volume to an almost uni-dimensional space, so that quasi-particles staying close to the barrier have a non zero probability to tunnel back into the normal metal and thus weaken the efficiency of the micro-cooler. More recently Rajauria et al.[68] extend the Rothwarf-Taylor equation for the relaxation of non-equilibrium quasi-particles. Experimentally we studied [71] the diffusion of out-of equilibrium quasi-particle trap, by injecting quasi-particle excess into the superconductor through an N-I-S junction and measuring a few micrometer further apart the superconductor temperature.
Recently, Peltonen et al. [62] showed that a small perpendicular magnetic field improves significantly the electronic refrigeration efficiency with a decrease of the minimum temperature of approximately 50 mK in presence of a magnetic field. This effect is attributed to an enhancement of quasi-particle relaxation within the superconductor, where magnetic vortices induced by the field are created, locally suppress the superconducting gap and drain the quasi-particles.

1.5 Conclusion

In this chapter, we have established concepts and tools that we shall use in the following chapters. It also helped to describe the framework of electronic refrigeration. Experimentally the theoretical prediction of electronic cooling have not been reached. Nevertheless, a lot of improvements and understandings of the phenomena has been

made and are very promising. The main problematic of this thesis is to understand the thermal couplings and physical phenomena involved in a micro-cooler device. Indeed, this thesis reports an experiment called «phonon thermometer». The purpose of this experiment is to verify a thermal model based on electron-phonon and Kapitza coupling. It also rises the question of heat conducted by photon, which is the object of an theoretical work. Finally we also present the effect of small magnetic field on electronic micro-cooling depending of the cooler geometry.

Chapter 2

Circuit approach to photonic heat transport

During the conception of the phonon thermometer experiment and before designing the sample, we investigate the heat transfer by photons between two metals coupled by a circuit containing linear reactive impedances. Indeed in our «phonon thermometer» experiment, we heat a copper wire and measure its electronic temperature and the electronic temperature of a circuit galvanically decoupled. We anticipate the possiblility of an extra-channel due to electromagnetic fluctuations of the hot metal heats the cold metal. Using a simple circuit approach [96], we calculate the spectral power transmitted from one metal to the other and find that it is determined by a photon transmission coefficient, which depends on the impedances of the metals and of the coupling circuit. We study the total photonic power flow for different coupling impedances, both in the linear regime, where the temperature difference between the metals is small, and in the non-linear regime of large temperature differences.

2.1 Introduction

In metallic systems, heat conduction can be achieved by electrons, phonons and also photons [30, 52, 78]. The photonic channel was recently revealed experimentally [45, 89] at very low temperature in devices including superconducting transmission lines. In a superconductor, electrons are paired into Cooper pairs so that the electron-phonon coupling is vanishing [88], just as the electronic heat conductance. Therefore, only photons can contribute to the heat transfer at zero temperature. With a good matching between the source and the drain, the conductance of a superconducting transmission line is equal to the thermal conductance quantum [63]: $K_Q = k_B^2 T\pi/6\hbar$.
The photonic channel for heat transfer can in principle couple metallic systems that are galvanically isolated, e.g. through a capacitor. This effect can be beneficial in some cases, but also detrimental when one wants to maintain two electronic populations at

different quasi-equilibrium temperatures. An inductance can also be present in some realistic configurations, due to the wiring geometry.
In this chapter, we investigate the photonic heat transfer through a general reactive impedance, i.e. a linear coupling circuit that contains a capacitor, an inductance, a resonant circuit or a transmission line. We follow a simple circuit approach, valid at low temperatures when the relevant photons have wavelengths larger than the size of the typical circuit element. The metallic parts can then be treated as lumped elements characterized by an electrical impedance. We present a quantitative analysis, enabling us to establish design rules for useful devices, including phonon thermometers or electron coolers.

2.2 Circuit approach

We consider the circuits A, B and C shown in Fig. 4.2.4. These configurations contain two impedances $Z_i(\omega)$ $(i = 1, 2)$, kept at different temperatures T_i such that $T_2 > T_1$. We wish to analyze heat flow between these elements driven by the temperature difference only, i.e. in the absence of any voltage or current source. In configurations A and C, the two impedances belong to *the same* circuit and are coupled through a purely reactive coupling element with impedance $Z_c(\omega)$ or a transmission line. Configuration A is a generalization of the one considered in Ref. [78]. In configuration B, the two impedances belong to *two different* circuits, both coupled via a mutual inductance M to a third linear circuit that mediates the heat transfer. Again we assume this coupling circuit to contain reactive elements only with a total impedance $Z_c(\omega)$. Configuration B was analyzed in Ref. [54] with non-equilibrium Green function techniques; here we will show that our circuit approach yields the same results. To the best of our knowledge, configuration C has not been analyzed until now.
In the absence of voltage or current sources, electromagnetic fluctuations are responsible for the heat flow between impedances. We therefore start our analysis by analyzing the current and voltage fluctuations induced by the various circuit elements. Following Ref. [7], we decompose the fluctuating current ΔI_i through the ith element into two parts:

$$\Delta I_i = \delta I_i + (1/Z_i)\Delta V_i. \tag{2.2.1}$$

The quantity ΔV_i is the voltage fluctuation across the element i. The fluctuation δI_i is the intrinsic fluctuation produced by the element due to Johnson-Nyquist noise with spectral function

$$\langle \delta I_i(\omega)\delta I_i(\omega')\rangle = 2\pi\delta(\omega+\omega')C_i^{(2)} \tag{2.2.2}$$

where $\langle ...\rangle$ denotes a thermal average and

$$C_i^{(2)} = \hbar\omega Re[1/Z_i(\omega)]\coth(\frac{\beta_i\hbar\omega}{2}), \tag{2.2.3}$$

with $\beta_i = 1/k_B T_i$ being the inverse temperature of element i. The δ-function in Eq. (2.2.2) reflects the fact that we consider noise in the stationary limit; Eq. (2.2.3) is the fluctuation-dissipation theorem[42], written in a form appropriate for Johnson-Nyquist noise generated by an impedance Z_i, kept at an inverse temperature β_i.
We consider fluctuations at low frequencies ω such that the wavelengths $\lambda_\omega \propto 1/\omega$ of the relevant electromagnetic waves are larger than the typical size of the circuit. At 1 Kelvin, this corresponds to a maximum circuit size of about 1 cm; this limit scales as $1/T$. It means that Kirchhoff's laws can be applied to the fluctuations ΔI_i and ΔV_i. For instance in circuit A, current conservation implies

$$\Delta I_i = \Delta I_j \equiv \Delta I$$

Similarly,

$$\sum_i \Delta V_i = 0$$

for any element $i, j = 1, 2, c$
We assume these constraints to be satisfied simultaneously for each element. We will be interested in the net power $P_i(t)$ absorbed by the element $i = 1, 2$ as a function of the temperature difference $\Delta T = T_2 - T_1$ between them. This quantity is given by $P_i(t) = \langle \Delta I_i(t) \Delta V_i(t) \rangle$. It can be expressed in terms of the frequency-dependent correlation function $\langle \Delta I_i(\omega) \Delta V_i(\omega') \rangle$:

$$P_i(t) = \int \frac{d\omega}{2\pi} \int \frac{d\omega'}{2\pi} e^{-i\omega t} e^{-i\omega' t} \langle \Delta I_i(\omega) \Delta V_i(\omega') \rangle. \tag{2.2.4}$$

We will calculate and analyze this quantity in detail below for circuits A, B and C.

2.3 Calculation of the heat exchange

2.3.1 Heat exchange with direct coupling

Let us first consider circuit A in Fig. 4.2.4, for the simple case where the reactive coupling element is absent, $Z_c(\omega) = 0$. Imposing the Kirchhoff laws on ΔI_i and ΔV_i, we obtain $\Delta V_1(\omega) = -\Delta V_2(\omega) = Z_1(\omega) Z_2(\omega) [\delta I_2(\omega) - \delta I_1(\omega)] / [Z_1(\omega) + Z_2(\omega)]$. Using Eq. (2.2.2) and the fact that the current noise in different elements is uncorrelated, $\langle \delta I_1 \delta I_2 \rangle = 0$, we find after some elementary algebra,

$$\begin{aligned} \langle \Delta I_1(\omega) \Delta V_1(\omega') \rangle = \; & -\langle \Delta I_2(\omega) \Delta V_2(\omega') \rangle \\ & 2\pi \delta(\omega + \omega') \frac{Z_1(\omega') Z_2(\omega')}{Z_t(\omega) Z_t(\omega')} \times [Z_2(\omega) C_2^{(2)}(\omega) - Z_1(\omega) C_1^{(2)}(\omega)] \end{aligned} \tag{2.3.1}$$

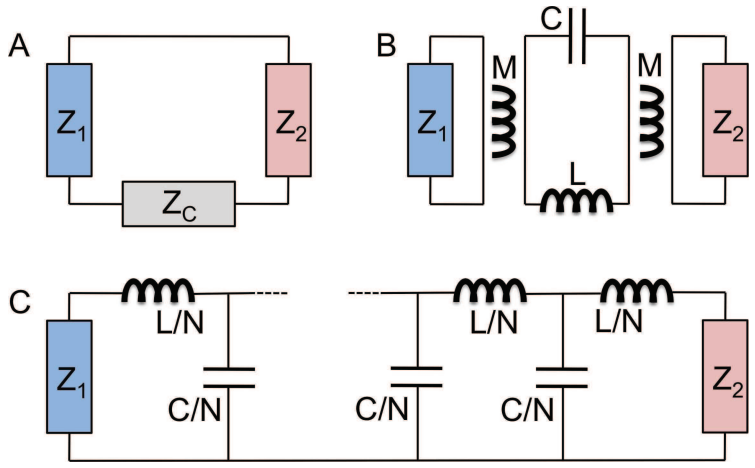

Figure 2.2.1: *Top left panel, circuit A: two impedances Z_1 and Z_2 are coupled by a purely reactive coupling impedance Z_c. Top right panel, circuit B: two impedances Z_1 and Z_2 are coupled via mutual inductances to a purely reactive central circuit of total impedance Z_c (here an LC resonator). Bottom panel, circuit C: two impedances Z_1 and Z_2 are coupled via a transmission line.*

Here $Z_t(\omega) = Z_1(\omega) + Z_2(\omega)$ is the total series impedance of the two elements. Substituting Eq. (2.3.1) into Eq. (2.2.4), using Eq. (2.2.3) and integrating over ω', we find

$$P_1(t) = \quad -P_2(t) = \quad \int_{-\infty}^{+\infty} \frac{d\omega}{2\pi} \frac{2\hbar\omega Re[Z_1(\omega)]Re[Z_2(\omega)]}{\mid Z_t(\omega) \mid^2} [n_2(\omega) - n_1(\omega)] \tag{2.3.2}$$

where we made use of the relation $Z(-\omega) = Z^*(\omega)$ as well as of the identity $\coth x = 1 + 2n(x)$, with $n(x) = [e^x - 1]^{-1}$. The result reflects energy conservation: the power emitted by one of the elements is absorbed by the other.
If we define an effective photon transmission coefficient

$$\mathcal{T}(\omega) = \frac{4\Re\mathrm{e}[Z_1(\omega)]\Re e[Z_2(\omega)]}{\mid Z_t(\omega) \mid^2}, \tag{2.3.3}$$

and use the fact that the integrand is an odd function of ω to restrict the integration to positive frequencies only, we can write:

$$P_1(t) = -P_2(t) = \int_0^{\infty} \frac{d\omega}{2\pi} \hbar\omega \mathcal{T}(\omega)[n_2(\omega) - n_1(\omega)]. \tag{2.3.4}$$

Note that this expression is similar to the one used to discuss heat transport in electron [82] and phonon systems [2] within the scattering approach. The net heat current is obtained as the difference of the two heat-currents emanating from impedances 1 and 2, that serve as photonic reservoirs each characterized by an equilibrium Bose-Einstein

distribution function at temperature $T_{1,2}$. Part of the total heat current injected by the photonic reservoirs can be reflected back, due to a mismatch between impedances Z_1 and Z_2. The amount of back-reflection can be frequency dependent; it is described by the frequency-dependent transmission coefficient $\mathcal{T}(\omega) \leq 1$.
Interestingly, as we will show below, Eqs. (2.3.3) and (2.3.4) describe the heat transfer between impedances 1 and 2 *for arbitrary configurations A, B and C, as long as the coupling elements are purely reactive*. The corresponding total impedance Z_t will be a configuration-dependent function of Z_1, Z_2 and the impedance of the coupling element. We will be interested in the heat transfer between elements 1 and 2 as a function of the temperature difference $\Delta T = T_2 - T_1$. For later use we define $\Delta\beta = \beta_1 - \beta_2$ and $\beta = (\beta_1 + \beta_2)/2$; then Eq. (2.3.4) can be rewritten as

$$P_1(t) = -P_2(t) = \int_0^\infty \frac{d\omega}{2\pi}\hbar\omega\mathcal{T}(\omega)\frac{\sinh \Delta\beta\hbar\omega/2}{\cosh \beta\hbar\omega - \cosh \Delta\beta\hbar\omega/2}. \tag{2.3.5}$$

If the temperature difference $\Delta T = T_2 - T_1$ is small compared to T_1 or T_2, we can expand the integrand to first order in $\Delta\beta$. The expression (2.3.6) then reads

$$P_{1,2}(t) = \pm \int_0^\infty \frac{d\omega}{2\pi}\hbar\omega\mathcal{T}(\omega)\frac{\Delta\beta\hbar\omega/2}{\cosh \beta\hbar\omega - 1}, \tag{2.3.6}$$

and can be further simplified to:

$$P_{1,2}(t) = K\Delta T = \frac{Tk_B^2}{\pi\hbar}\int_0^\infty d\mathrm{x}\mathcal{T}(\mathrm{x})\frac{\mathrm{x}^2}{\sinh^2(\mathrm{x})}\Delta T. \tag{2.3.7}$$

where $T = (T_1 + T_2)/2$ is the average temperature and K is the thermal conductance. Furthermore, if the two impedances 1 and 2 are two identical resistances, so that $R_1 = R_2 = R$, the photon transmission coefficient $\mathcal{T} = 1$ and the thermal conductance K is given by its quantized value,

$$K = K_Q = \frac{k_B^2 T\pi}{6\hbar}.$$

For instance for $\mathcal{T} = 1$, the thermal conductance is estimated to approximately 1 pW/K at 1 K. For mismatched resistances $R_1 \neq R_2$, the photon transmission coefficient $\mathcal{T}$ is smaller than 1 and the thermal conductance K will be less than K_Q.

2.3.2 Heat exchange with reactive coupling

Let us now consider the more general case of circuit A with a non-zero reactive coupling impedance, following the same approach. Since no noise is generated in a purely reactive element, the spectral noise current through it is simply given by

$$\Delta I_c = \Delta V_c / Z_c. \tag{2.3.8}$$

Imposing the constraint on ΔI_i we then find

$$\Delta I(\omega) = [Z_1(\omega)\delta I_1(\omega) + Z_2(\omega)\delta I_2(\omega)]/Z_t(\omega). \tag{2.3.9}$$

Now $Z_t(\omega)$ includes the coupling impedance,

$$Z_t(\omega) = Z_1(\omega) + Z_2(\omega) + Z_c(\omega). \tag{2.3.10}$$

The constraint on ΔV_i leads to

$$\Delta V_1(\omega) + \Delta V_2(\omega) = -Z_c(\omega)\Delta I(\omega). \tag{2.3.11}$$

Moreover,

$$Z_1(\omega)\Delta V_2(\omega) - Z_2(\omega)\Delta V_1(\omega) = Z_1(\omega)Z_2(\omega)[\delta I_1(\omega) - \delta I_2(\omega)]. \tag{2.3.12}$$

This system of equations can be solved for ΔV_1 and ΔV_2. The purely reactive impedance will neither emit nor absorb any power, we therefore obtain

$$P_1(t) = \langle \Delta I_1 \Delta V_1 \rangle = -\langle \Delta I_2 \Delta V_2 \rangle = -P_2(t). \tag{2.3.13}$$

A straightforward calculation then yields Eqs. (2.3.3) and (2.3.4), with the appropriate re-definition of the total series impedance $Z_t = Z_1 + Z_2 + Z_c$. This result generalizes the one presented in Ref. [45].

2.3.3 Heat exchange with mutual inductive coupling

In this subsection, we consider configuration B, see Fig. 4.2.4. The mutual inductance M relates the current fluctuations ΔI_c in the central coupling circuit to the voltage fluctuations in the two outer circuits,

$$\Delta V_{1,2}(\omega) = i\omega M \Delta I_c(\omega), \tag{2.3.14}$$

hence we have:

$$\Delta I_i(\omega) = \delta I_i(\omega) + i\omega M \Delta I_c(\omega)/Z_i(\omega). \tag{2.3.15}$$

On the other hand, the current fluctuations ΔI_1 and ΔI_2 in the outer circuits are related to the fluctuation ΔI_c in the central circuit, according to the relation $\Delta I_c(\omega) = i\omega M[\Delta I_1(\omega) + \Delta I_2(\omega)]/Z_c(\omega)$, where $Z_c(\omega)$ is the total series impedance of the elements in the central circuit, which we assume to be entirely reactive. Combining these observations, we conclude that

$$\Delta I_c(\omega) = \frac{i\omega M[\delta I_1(\omega) + \delta I_2(\omega)]}{Z_c(\omega) + \omega^2 M^2[1/Z_1(\omega_1) + 1/Z(\omega_2)]}. \tag{2.3.16}$$

We substitute this result into the expressions for $\Delta I_i(\omega)$ and $\Delta V_i(\omega')$, multiply them and obtain the power absorbed by the impedance Z_i upon the appropriate Fourier transformation according to Eq. (2.2.4). Using the fact that $Z_c(\omega)$ is purely imaginary, we again find Eqs. (2.3.3) and (2.3.4) to hold, but with the total impedance given by:

$$Z_t(\omega) = Z_1(\omega) + Z_2(\omega) + Z_c(\omega)\frac{Z_1(\omega)Z_2(\omega)}{\omega^2 M^2}. \tag{2.3.17}$$

This is in agreement with the result obtained in Ref. [54] based on Meir-Wingreen-Landauer type formula by applying nonequilibrium Green's function methods. Indeed the photon heat depends of the mutual inductance and the characteristics of the central island. However, we wish to note it is obtained here from quite simple circuit considerations, without the need of a Green function formalism. In reality, most of mesoscopic metallic devices can be described as combination of capacitances, inductances and resistors. Then the circuit theory, easier to compute relatively to other methods, gives an easy approach of the photonic heat transport.

2.3.4 Heat exchange through a transmission line

Let us finally study case C, see Fig. 4.2.4. A transmission line is represented by a series of N cells, each composed by an inductance L/N and a capacitance C/N. Considering again a photon wavelength larger than the size of a typical circuit element, we apply Kirchhoff's law locally and find a recurrence equation between the potential V_n at element n and the ones for the neighboring cells V_{n-1} and V_{n+1}:

$$V_{n-1} + V_{n+1} + \left(\omega^2 \frac{LC}{N^2} - 2\right) V_n = 0. \tag{2.3.18}$$

Writing the local voltage as a plane wave $V_n \propto e^{i(kn-\omega t)}$ we obtain the dispersion relation

$$\cos k = 1 - \frac{\omega^2 LC}{2N^2}, \tag{2.3.19}$$

describing propagating waves with a wave-vector dependent group velocity, thus taking into account retardation effects in the line. Writing the expression of the current at both extremities of the transmission line, we find:

$$\Delta I_1 = -\frac{\Delta V_1}{Z_A} + \frac{\Delta V_2}{Z_B}, \tag{2.3.20}$$

$$\Delta I_2 = -\frac{\Delta V_2}{Z_A} + \frac{\Delta V_1}{Z_B}, \tag{2.3.21}$$

with the characteristic line impedances Z_A and Z_B defined as

$$Z_A = \frac{i\omega L}{N(1-\cos k+\sin k\cot kN)}, \tag{2.3.22}$$

$$Z_B = -i\omega\frac{L}{N}\frac{\sin kN}{\sin k}. \tag{2.3.23}$$

Identifying the above expressions with Eq. (2.2.1) enables us to write the voltages V_1 et V_2 at the resistors 1,2 as a function of the intrinsic current fluctuations δI_1 et δI_2:

$$\Delta V_2 = \frac{Z_B^2\tilde{Z}_2}{\tilde{Z}_1\tilde{Z}_2-Z_B^2}\delta I_2+\frac{Z_B\tilde{Z}_1\tilde{Z}_2}{\tilde{Z}_1\tilde{Z}_2-Z_B^2}\delta I_1, \tag{2.3.24}$$

$$\Delta V_1 = \frac{Z_B^2\tilde{Z}_1}{\tilde{Z}_1\tilde{Z}_2-Z_B^2}\delta I_1+\frac{Z_B\tilde{Z}_1\tilde{Z}_2}{\tilde{Z}_1\tilde{Z}_2-Z_B^2}\delta I_2, \tag{2.3.25}$$

where we have defined:

$$\frac{1}{\tilde{Z}_{1,2}}=\frac{1}{Z_{1,2}}+\frac{1}{Z_A}. \tag{2.3.26}$$

Using Eq. (2.2.4) while writing the quantities $\Delta V_i(\omega)$ and $\Delta I_i(\omega)$ in terms of the current fluctuations δI_i gives the expression of the power absorbed by the impedance Z_i. We again obtain Eqs. (2.3.3) and (2.3.4) to hold, with the total impedance given by:

$$\begin{aligned} Z_t(\omega) = {} & i\omega\frac{L}{N}\frac{\sin kN}{\sin k}+\frac{\cos k(N-1/2)}{\cos k/2}\left[Z_1+Z_2\right] \\ & +\frac{Z_1Z_2N}{i\omega L}\left[\left(\frac{\cos k(N-1/2)}{\cos k/2}\right)^2-1\right]\frac{\sin k}{\sin kN} \end{aligned} \tag{2.3.27}$$

As far as we know, it is the first time that heat transport, mediated by electromagnetic fluctuations, is calculated in the transmission line, especially using circuit theory.

2.4 Results

2.4.1 Direct inductive coupling

To be specific, let us first consider the case of circuit A with an inductive coupling, $Z_c = i\omega L$, coupling two identical resistors, $Z_1 = Z_2 = R$, kept at a small temperature difference ΔT. Eq. (2.3.7) then provides the expression for the thermal conductance K_L upon substitution of

$$\mathcal{T}_L(\mathrm{x}) = \frac{\alpha_L^2}{\alpha_L^2+\mathrm{x}^2}, \tag{2.4.1}$$

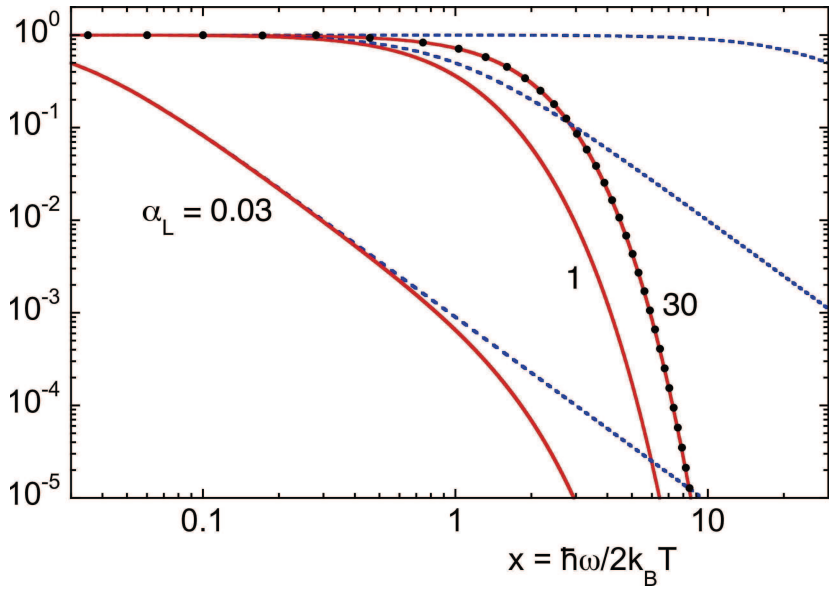

Figure 2.4.1: *Case of an inductive coupling. Spectrum of the thermal noise power density* $x^2/\sinh^2 x$ *(black dots), the photon transmission coefficient* $\mathcal{T}_L(x) = \alpha_L^2/(\alpha_L^2 + x^2)$ *(dotted blue line) and of the product of the two (thin red full line) as a function of the frequency, for different values of the parameter* α_L *= 0.03, 1 and 30 from top to bottom. The frequency is plotted in units of the thermal frequency* $2k_BT/\hbar$*. We consider the case of perfect resistance matching* $R_1 = R_2 = R$*.*

which is the relevant photon transmission coefficient as a function of the dimensionless frequency $\mathrm{x} = \hbar\omega/2k_BT$. The parameter

$$\alpha_L = \frac{\hbar R}{L k_B T} \tag{2.4.2}$$

defines the crossover between the low-frequency regime $\mathrm{x} \ll \alpha_L$ where the inductance is transparent and the corresponding photon transmission coefficient $\mathcal{T}_L(\mathrm{x})$ is close to 1 and the high-frequency regime $\mathrm{x} \gg \alpha_L$ where the inductance becomes opaque and $\mathcal{T}_L(\mathrm{x}) \sim \alpha_L^2/\mathrm{x}^2 \ll 1$. The result (2.4.1) for the photon transmission coefficient can thus be understood as originating from a low-pass LR filter composed of the resistance R and the coupling inductance L that filters the photonic thermal spectrum. The cut-off frequency is given by α_L in units of the thermal frequency $2k_BT/h$, at frequencies beyond the cut-off frequency the transmission decays as $1/\mathrm{x}^2$.
We have calculated the spectral density of the photonic heat transferred from one resistor to the other for several values of the parameter α_L. Fig.2.4.1 displays the spectrum of the thermal noise current $\mathrm{x}^2/\sinh^2(\mathrm{x})$, the photon transmission coefficient $\mathcal{T}_L(\mathrm{x})$ and of the product of the two. The integral of the latter quantity gives the power transmitted

by photons $P_{1,2}$. In the limit $\alpha_L \gg 1$ of a small inductance, i.e. a negligible coupling impedance, the photon transmission coefficient equals to unity over the whole thermal spectrum. The integral is then equal to $\pi^2/6$ and one again recovers the quantum of conductance, $K_L = K_Q$. In the opposite limit $\alpha_L \ll 1$ of a large inductance, the photon transmission coefficient decays when the frequency is increased. The photonic signal is then strongly suppressed: $K_L \ll K_Q$.

2.4.2 Direct capacitive coupling

Let us now consider the case of circuit A with a capacitive coupling element $Z_c = 1/i\omega C$. We assume again that the two impedances 1 and 2 are pure resistors with a small temperature difference. The thermal conductance K_C is given by Eq. (2.3.7) taking into account the photon transmission coefficient:

$$\mathcal{T}_C(\mathrm{x}) = \frac{\mathrm{x}^2}{\mathrm{x}^2 + \alpha_C^2}. \tag{2.4.3}$$

The cross-over frequency is now determined by the parameter

$$\alpha_C = \frac{\hbar}{4RCk_BT}; \tag{2.4.4}$$

it separates a low-frequency regime $\mathrm{x} \ll \alpha_C$ where the capacitor is opaque and $\mathcal{T}_C(\mathrm{x}) \sim \mathrm{x}^2/\alpha_C^2 \ll 1$ from a high-frequency regime $\mathrm{x} \gg \alpha_C$ where the capacitor is transparent and $\mathcal{T}_C(\mathrm{x}) \sim 1$.
Fig. 2.4.2 displays information similar to that of Fig. 2.4.1 but for the case of a capacitance coupling the two resistors, yielding the photon transmission coefficient $\mathcal{T}_C$, Eq. (2.4.3). The limit $\alpha_C \ll 1$ means that the capacitance is large, i.e. it has a negligible impedance over most of the thermal spectrum. The transparency $\mathcal{T}_C$ is then equal to unity and one recovers $K_C = K_Q$. In the limit $\alpha_C \gg 1$, the photonic signal is strongly suppressed by the RC filter composed of the series capacitance and the receiver resistance, leading to $K_C \ll K_Q$.

2.4.3 Mutual coupling to an LC-resonator

We now turn to circuit B, for the case where the central coupling circuit is an LC-resonator, as indicated in Fig. 4.2.4. This means that $Z_c(\omega) = i\omega L + 1/i\omega C$, the resonant frequency is given by $\omega_0 = \sqrt{1/LC}$. Assuming again $R_1 = R_2 = R$ and a small temperature difference ΔT, the thermal conductance K_M is given by Eq. 2.3.7 with the photon transmission coefficient:

$$\mathcal{T}_M(\mathrm{x}) = \frac{1}{1 + \alpha_M^2(\mathrm{x}/\gamma - \gamma/\mathrm{x})^2\mathrm{x}^{-4}}. \tag{2.4.5}$$

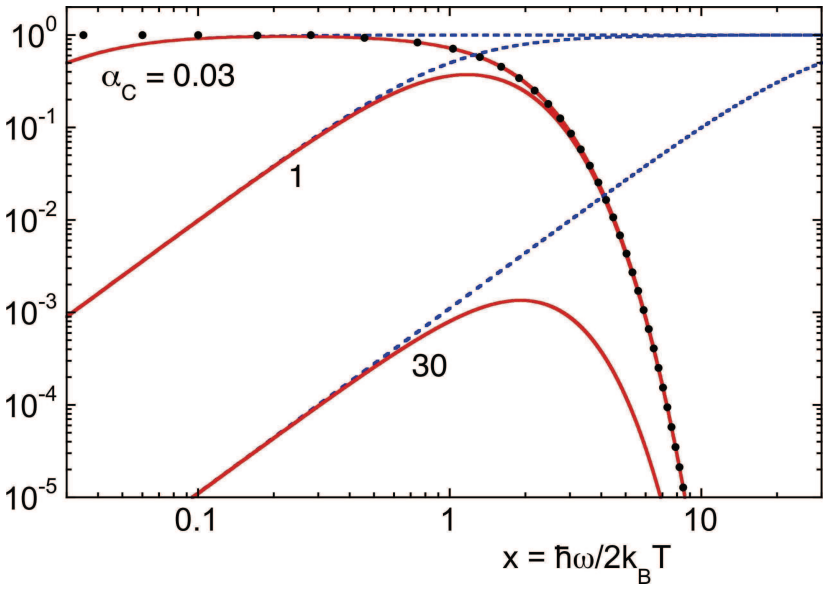

Figure 2.4.2: *Case of a capacitive coupling. Spectrum of the thermal noise power density* $x^2/\sinh^2 x$ *(black dots), the photon transmission coefficient* $\mathcal{T}_C(x) = x^2/(x^2+\alpha_C^2)$ *(dotted blue line) and of the product of the two (thin red full line) as a function of the frequency, for different values of the parameter* α_C *= 0.03, 1 and 30 from top to bottom. The frequency is plotted in units of the thermal frequency* $2k_BT/\hbar$*. We consider the case of perfect resistance matching* $R_1 = R_2 = R$*.*

Here

$$\alpha_M = \frac{R}{2}\sqrt{\frac{C}{L}}\left(\frac{L}{M}\right)^2\gamma^2 \tag{2.4.6}$$

and

$$\gamma = \hbar\omega_0/2k_BT. \tag{2.4.7}$$

As shown on figure 2.4.3, the photon transmission coefficient is characterized by a resonance at ω_0, the width of which is governed by the parameter α_M: the larger α_M, the narrower the resonance. For small values of α_M, the transmission coefficient is close to 1 over the thermal spectrum frequency range and we find $K_M \lesssim K_Q$.

2.4.4 Coupling through a transmission line

We finally deal with circuit C, with two pure resistors R_1 and R_2 separated by a transmission line that behaves like a low pass filter with a cut-off frequency $\omega_c = 2/\sqrt{LC}$. In

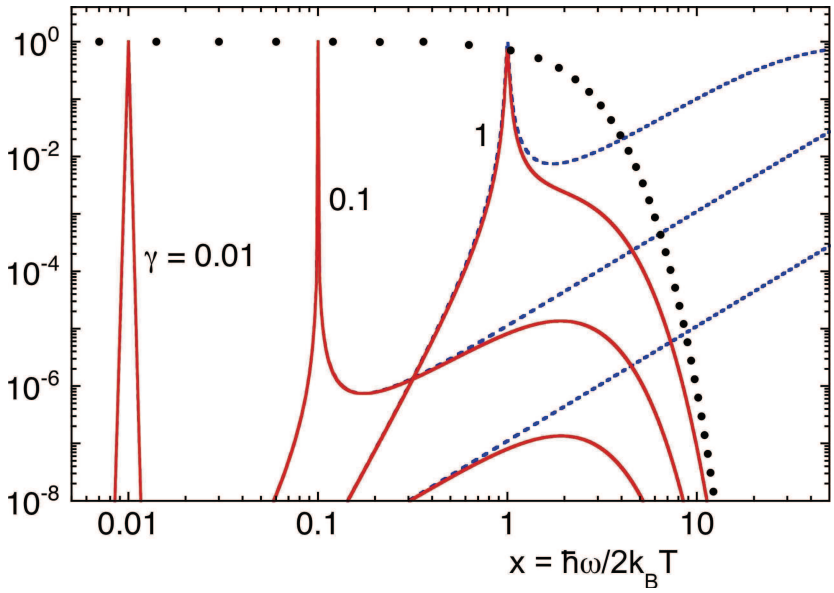

Figure 2.4.3: *Case of a mutual coupling via an LC-resonator circuit. Spectrum of the thermal noise power density* $x^2/\sinh^2 x$ *(black dots), the spectral transmission factor* $\mathcal{T}_M(x)$ *(dotted blue line) and of the product of the two (thin red full line) as a function of the frequency, for different values of the parameter* $\gamma = 0.01$*, 0.1 and 1 from top to bottom. The frequency is plotted in units of the thermal frequency* $2k_BT/\hbar$*. We consider the case of perfect resistance matching* $R_1 = R_2$ *and a parameter* $\alpha_M = 30$*.*

the limit of very low frequency $\omega \ll \omega_c$, the total impedance Z_t is

$$Z_t(\mathrm{x}) = \quad (R_1 + R_2)\cos(N\alpha_{TL}\mathrm{x}) + \quad i\sin(N\alpha_{TL}\mathrm{x})\sqrt{\frac{L}{C}}\left[1 + R_1R_2\frac{C}{L}\right] \tag{2.4.8}$$

where

$$\alpha_{TL} = 4k_BT/\hbar\omega_c. \tag{2.4.9}$$

For frequencies below ω_c, the impedance Z_t features a series of resonances, which is the ratio between λ_ω and the transmission line length. These resonances come from the first real part of Z_t, Eq. 2.4.8, and match the number cells used for discretization of the transmission line. In the formula, the length of transmission line is given by the product between the number of cells and their typical cell size, needed to apply Kirchhoff's law between the nearest cells. In reality, the length of transmission line is much larger than size cell. In the limit of infinite number of elements, $N \to \infty$, the resonnances disappear, and the transmission line spectrum shows gate fonction acting as a efficient low-pass filter. At every resonance including the zero-frequency case, the transmission line is fully transparent and the impedance Z_t is equal to $R_1 + R_2$.

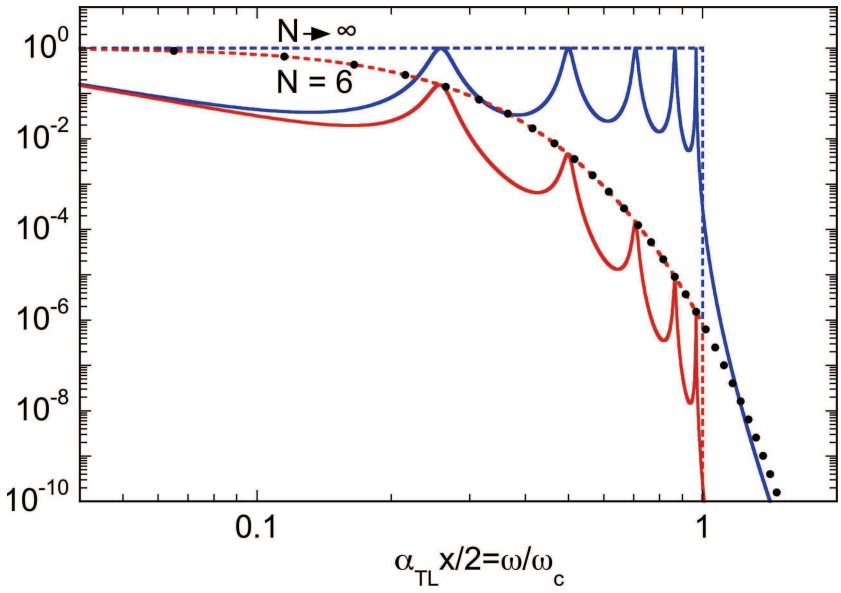

Figure 2.4.4: *Case of a coupling through a transmission line. Spectrum of the thermal noise power density $x^2/\sinh^2 x$ (black dots), the photon transmission coefficient $\mathcal{T}_{TL}(x)$ (dotted and full blue lines) and of the product of the two (dotted and full red lines) as a function of the frequency. The full lines stand for a number of cells $N = 6$ and the dotted lines for N infinite. The frequency is plotted in units of the cut-off frequency ω_c. We consider a temperature T so that $\alpha_{TL} = 0.2$ and the case of perfect resistance matching $R_1 = R_2$ with $R == 0.1\sqrt{L/C}$.*

At frequencies well above the cut-off frequency $\omega \gg \omega_c$, we can make the approximation $\cos k \simeq -\omega^2 LC/2N^2$. The wave-vector k is then complex. The total impedance is purely imaginary and diverging at high frequency as:

$$Z_t = i\alpha_{TL}\mathrm{x}\sqrt{\frac{L}{C}}[-\mathrm{x}^2\alpha_{TL}^2]^{N-1}. \tag{2.4.10}$$

From Eq. 2.3.3, the transmission coefficient $\mathcal{T}_{TL}$ is related to the line impedance Z_t as: $\mathcal{T}_{TL}(\omega) = 4R_1R_2/\mid Z_t(\omega)\mid^2$. Fig.2.4.4 shows the transmission coefficient for a number of cells $N = 6$ and $N = \infty$, in the case $R_1 = R_2 = 0.1\sqrt{L/C}$, $\alpha_{TL} = 0.2$. For a finite $N = 6$, we observe a series of resonance peaks, featuring a maximum transmission equal to unity. The case $N = \infty$ corresponds to the continuum limit, where the discretization necessary for the calculation vanishes. In this case, the impedance Z_t is constant and equal to $R_1 + R_2$ over the full bandwidth $[0, \omega_c]$ and infinite above. The transmission is then unity within the bandwidth (if $R_1 = R_2$) and zero above.

2.4.5 Total photonic power with reactive coupling

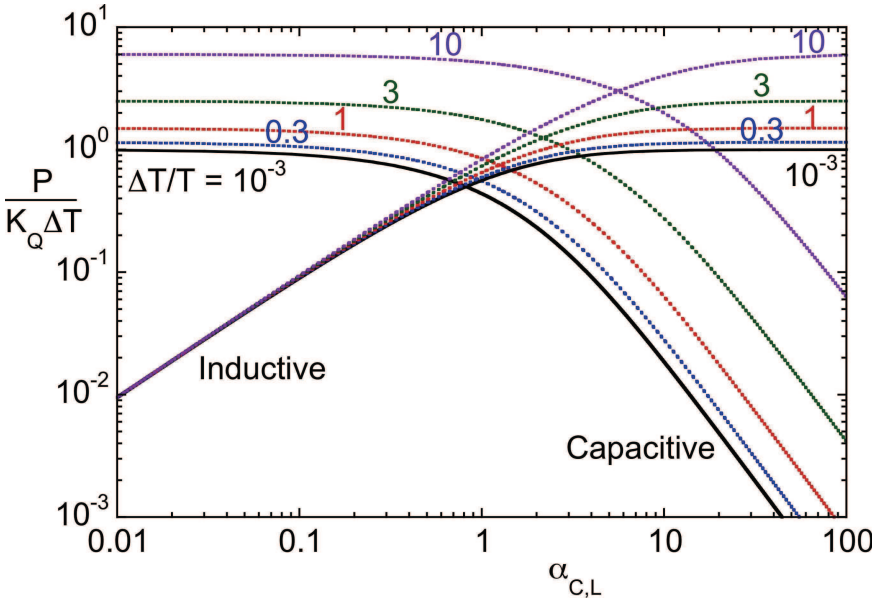

Figure 2.4.5: *Dependence of the photonic power through a capacitive or inductive coupling impedance on the parameters α_C or α_L for different values of the relative temperature difference $\Delta T/T$, in units of $K_Q \Delta T$, the maximum photonic power in the case of a linear response.*

Finally, we have calculated the total photonic power, integrated over the full frequency range, as a function of the parameter α_L or α_C in the respective cases of an inductive or capacitive coupling. We compare both linear and nonlinear response, changing the values of the relative temperature difference $\Delta T/T$, see Fig. 2.4.5. In the limit of a small temperature difference and with an inductive coupling, the photonic power decays as α_L when α_L is small. For a capacitive or mutual coupling, the total power is maximal for small $\alpha_{C,M}$; it decays as $1/\alpha_{C,M}^2$ when $\alpha_{C,M}$ is large.
A cross-over between the linear regime $P \propto \Delta T$ and the non-linear regime occurs at $\Delta T/T \approx 1$. When the temperature difference is large, the photonic thermal conductance is larger than the quanta K_Q, because of the broader frequency range of the emitted photons. Only in the case of a significantly inductive coupling $\alpha_L > 1$, which cuts the high frequencies induced by the higher source temperature, does the thermal conductance not depend on the temperature difference.
In the cases of a coupling through a resonator or a transmission line, the behavior of the total photonic power as a function of the relevant parameter α_M or α_{TL} is similar to the capacitive case.

2.5 Conclusion

In summary, we have introduced a simple circuit approach of the photonic heat transport that can be applied to a variety of experimentally-relevant situations. We would like to stress that this approach operates within a very simple formalism, thus providing an intuitive understanding of photonic thermal conduction channel. This approach enabled us to investigate the phonic heat transfer through a reactive transmission line.
To conclude, let us discuss the possibility to practically use the photonic channel discussed above to transmit power between two electronic circuits that are galvanically isolated. This can be achieved by coupling two resistors through two capacitances. From the above discussion, the maximum efficiency can be attained when the source and receiver impedance are well matched and with a parameter α_C below about 0.1. With impedances of 50 Ω, this corresponds to a capacitance value larger than 0.1 pF at a temperature of 4 K or 10 pF at 40 mK, which is significantly higher that the 1-10 fF capacitance of typical submicron scale junctions. In Ref. [89], the estimated 10 fF ground capacitance gives a α_C parameter value of about 38 at a temperature of 100 mK. From Fig. 2.4.5, one extracts that this results in a heat transfer rate divided by about 1000 compared to the full value, which is consistent with experimental results [89]. In a real thermal circuit, large series capacitances can easily be integrated using available microfabrication technologies and ensure a fully-efficient photonic channel thermal coupling, while maintaining galvanic insulation. The related thermal conductance is about 1 pW/K at 1 K and scales linearly with the temperature. This approach is thus compatible with the cooling of small objects well decoupled from the thermal bath, like for instance membranes .
As discussed above, photonic heat can also be transmitted through a transmission line, provided that its cut-off frequency is larger than the thermal spectrum bandwidth. Let is consider for instance a superconducting line of width 1 μm and thickness 50 nm. Its kinetic inductance is about 10 pH/mm and its capacitance to the ground about 0.5 fF/mm. The related cut-off frequency is then about 1.7 K for a line length of 10 mm.
Finally, it is interesting to discuss the present results in connection with the "brownian refrigeration" of a cold normal metal in contact with a superconductor via a capacitively shunted tunnel barrier, subjected to the thermal noise generated in a hot resistor [57]. For typical system parameters, an optimum exists where a hot resistor of resistance $R = 10R_K$ with $R_K = h/e^2$ gives rise to heat extraction currents of about $10^{-3}\Delta^2/e^2R_T$, where Δ is the superconducting gap and R_T is the tunnel barrier normal-state resistance. However, at the same time, the photon heat channel discussed in the present work will be active, inducing a heat current from the hot resistor *towards* the cold normal metal. This was not included in Ref. [57], where the resistance R_N of the normal metal was set to zero. We can estimate the effect of the photon heat current by modeling the set-up as in A-type circuit: a series combination of the hot and cold resistors of resistance R and R_N, respectively, coupled by a capacitance C. Using typical parameters of Ref. [57]

and assuming a resistance mismatch $R_N/R = 0.01$, the direct photon heat current can be estimated to be $10^{-3}\Delta^2/e^2R_K$, which is comparable to or larger than the heat extraction current if $R_T \gtrsim R_K$. In order to recover a net cooling of the cold resistor, it is not possible to reduce R_T below R_K, as spurious higher order tunneling processes in the junction would reduce the heat extraction current. One can however increase the resistance mismatch: the photon heat current is proportional to R_N/R. We conclude that the heat extraction mechanism of Ref. [57] outweighs possible direct photon heating only for metals with resistances R_N of a few Ohms or less.
To answer to the initial issue, let us discuss the present results applied to the "phonon thermometer" with a hot normal metal in contact with a cold normal metal via a silicon insulating layer, subjected to the thermal noise generated in a hot resistor. Could the cold resistor cool down the hot resistor ? We can estimate the effect of the photon heat current by modeling the set-up as a A-type circuit, see Fig. 4.2.4: a series combination of the hot and cold resistors of resistance $R \sim 50$ - $100\ \Omega$ and $R_N \sim 5\ \Omega$, respectively, coupled by a capacitance $C \sim 5$ fF. Using typical parameters of our design and assuming a weak resistance mismatch $R_N/R \simeq 0.1$. Even if we exagerate to $\Delta T/T \sim 10$, we obtain ${}^{P}/_{K_Q \Delta T} \sim 10^{-2}$ with our parameters. Consequently the direct photon heat current can be estimated to be of the order of femtowatt. This is smaller than the cooling power, which is in the range of picowatt. In our study, we are thus able to neglect this photonic heat channel. If the conditions of experiment are changed, we can in every case calculate it with the method devised in this chapter.

Chapter 3

Sample fabrication

3.1 Introduction

A well-controlled sample is the keystone to perform a mesoscopic physics experiment and study its the quantum behavior at a scale barely smaller than the thickness of an hair. In the framework of the semi-conductor electronics industry, machines have been invented and improved in order to fabricate devices with a resolution of the order of few nanometers. Thanks to these technological breakthroughs, researchers are able to design circuits matching the drastic specifications necessary to demonstrate quantum phenomena. The more a sample design is well-defined, the easier it will be to fit experimental results to a theory or define a model.
There are different techniques of fabrication: bottom-up or top-down. Among all the top-down techniques, we used the lift-off technique involving e-beam lithography and a combination of photo-lithography and chemical etch of a multilayer. The different types of lithography available in Grenoble, especially at Nanofab platform where we make our samples, are UV-lithography (resolution of the order of a micron), Deep Ultra-Violet lithography (resolution of half a micron), e-beam lithography (resolution of few a nanometers). Since our samples are hybrid superconducting devices, we need aluminum, copper, silicon and an oxygen line to make the tunnel barrier. There are different possibilities to evaporate these materials. Sputtering system allows to deposit conformly a metal, insulator or semi-conductor at ambiant temperatures. Joule and e-beam evaporators are more suitable to perform angle shadow evaporations since the deposition is directive. In a Joule evaporator, the current flowing through the crucible heats the material so that it evaporates. In a e-beam evaporator, an electronic beam targets the crucible so that it boils locally and evaporates.
The two techniques used during this thesis to fabricate our samples are presented in this chapter. The first one is the traditionnal shadow evaporation technique [16] with large angles that make junctions of micrometer maximum size, the second is an over-etching technique that make junctions of micrometer minimum size. These are two very different

but complementary ways to fabricate hybrid superconducting devices.

3.2 Large angles shadow evaporation technique

For most of our samples, we use the well-known lift-off technique with angle shadow evaporation. It consists in patterning a circuit in a positive resist, where the exposed zone goes away during the development, depositing the metal and lifting-off the resist with a solvant. This technique has been brought to its limits in order to pattern our samples so-called phonon thermometers. Indeed this particular design is made of two main steps, which are two aligned electronic lithographies.

Principle of the Niemeyer-Dolan technique

The Niemeyer-Dolan technique [16] also called the shadow evaporation technique is a neat way to fabricate controlled high-quality tunnel junctions with an alignment of different deposit of the scale of tens nanometers. Instead of two electronic lithographies aligned with a precision of 50 nm maximum (~ few days work), this well-known technique allows to control the shift in x or y between the two deposits (~few hours work). It relies on a bilayer resist. Each layer is made of a different electrosensitive resist for instance PMMMA-MAA 33% at the bottom and PMMA 4% at the top. Since the bottom resist is more sensitive to electrons and also to developer than the top one, the bilayer presents after development an undercut as described on the right of figure 3.2.1. During the metal evaporation through the suspended resist mask, the pattern is projected on the substrate. The pattern evaporated with an angle α from the source gives an deposit shifted on the substrate by s = (h + e). tan α where h is the thickness of the bottom layer and e is the thickness of the top layer, as described on the left sketch 3.2.1. The evaporation is made in the convenient axes of the scketch where one is able to control the overlap between the depositions. With a good design and basic spatial representation skills it allows to fabricate complex circuits.
Nevertheless, this neat technique is not universal because of few drawbacks. The first one is the size limitation of shifted elements and the second one is the ghost marks that are problematic for successive lithographies as our samples request. The fabrication of our samples is described in the following paragraphs. The goal is to obtain two perfectly superposed circuits galvanically decoupled. We perform each electronic lithography with alignment on golden marks realized by optical lithography.

3.2.1 Paterning of alignment marks by optical lithography

The lithography mask

The optical mask is made of quartz and coated by the negative pattern in chromium. As shown in figure 3.2.2, the mask presents nine chips. Each chip has three types of

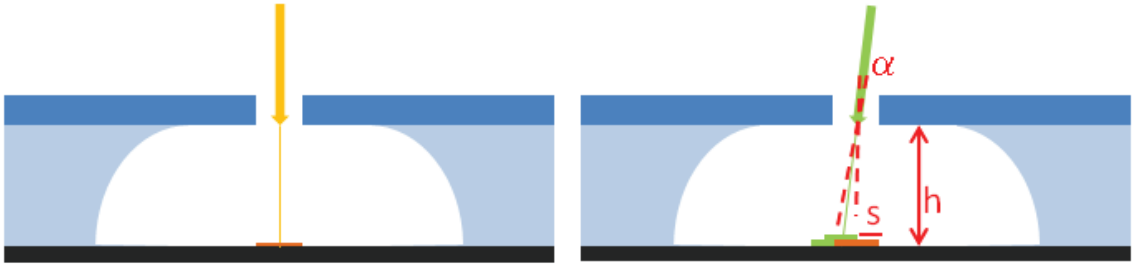

Figure 3.2.1: *Shadow evaporation technique without angle on the left, and with an angle α on the right giving a deposit translated from the pattern mask by a shift s=(h+e).tan α with h the thickness of bottom layer, α angle between the crucible and the substrate.*

marks. There is a set of 4 marks at each corner defining the local coordinates, two marks (blue outline) helps to align the different fields globally and eight marks on each sample : one for each scan direction, each field and each lithography. The figure 3.2.2 presents in detail the mask we use. Notice that this mask is not centro-symetric so we take care of the orientation given by the alignment fields marks.

Substrate preparation

The starting point is a 2 inches silicon wafer with 500 nm of SiO_2 from Siltronix[1]. In order to suppress any organic residues from the surface, we introduce the wafer in the chamber of a Reactive Ion Etching (RIE) machine for 2 minutes in a 50 W RF power plasma and a pressure of 2.10^{-1} mbar.

Optical lithography process

After cleaning the wafer, the optical marks used to align the different e-beam lithographies are realized by DUV lithography with 0.5 µm resolution. All the steps of optical lithography from resist coating to development are summarized in the following table 3.1.

1. Characteristics : Ø2", N-Phosphorous doped, 0.001-0.005 Ω.cm, thickness 250 - 300 µm, orientation (100) ±0.5°, processus Czochralski, 500 nm thermal wet oxide.

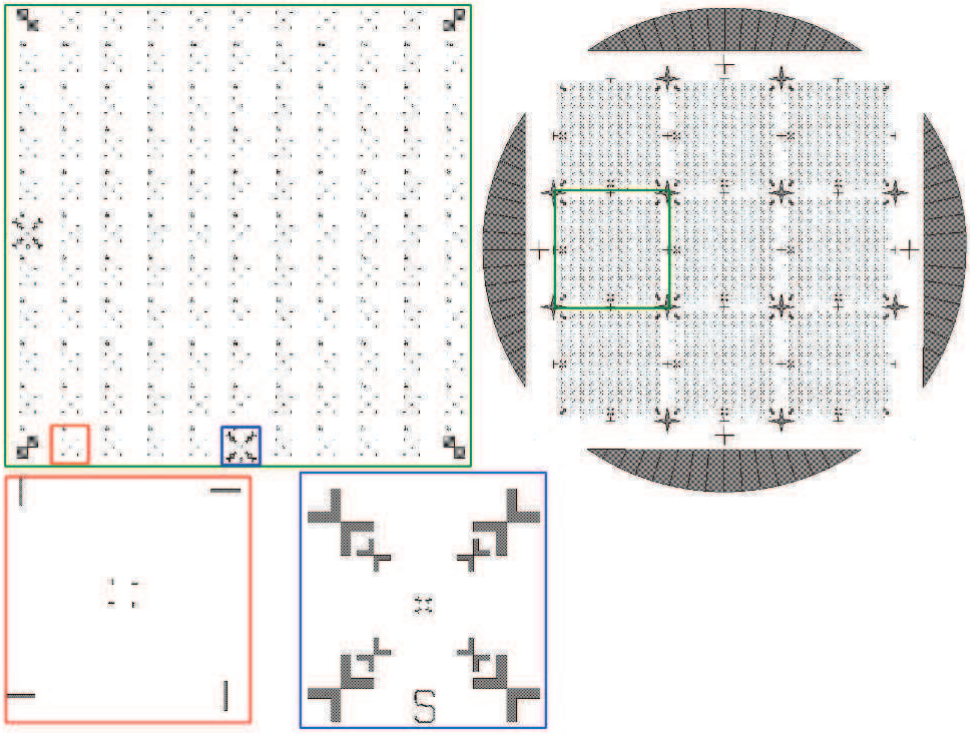

Figure 3.2.2: *Optical lithography mask for patterning alignment marks: it presents 9 chips, each chip (green outline) has 115 alignment chip mark sets (red outline) and two marks to align the field on the wafer (blue outline)*

step	process	equipment	parameters / remarks
1	wafer cleaning	RIE oxygen plasma	«Res» program : 1' - 2 10^{-1}mbar - RF power 50W
2	resist deposition «UV3»	spin-coater	4000 rpm - 2000 rpm/s - 30"
3	soft bake	hot-plate	1 minute at 130°C
4	exposure	MJB3 DUV aligner	5.5" CI 475W
5	hard bake	hot-plate	1 minute at 130°C
6	development	pure LDD26W or pure MFCD26 beaker	30" Warning : develop faster when temperature increases
7	rincing	flowing DI water	2'
8	drying	nitrogen gun	no tweezers gun perpendicular to the wafer blowing from the bottom to the top
	$\Longrightarrow$resist thickness = 500 nm		

Table 3.1: *Optical lithography process*

Metal deposition with lift-off technique

The different steps of metal deposition and lift-off are presented in Table 3.2. Titanium is used to stick gold on the wafer. The alignment marks are in gold because of its higher atomic number compared to aluminium and copper. It is then more easy to see the alignment marks with a SEM. For a clean lift-off, the deposited metal thickness needs to be less than one third of the resist thickness.

step	process	equipment	parameters / remarks
1	Titanium deposition	Plassys e-beam evaporator	10 nm - $\alpha = 0°$ - v = 2 Å /s
2	Gold deposition	Plassys e-beam evaporator	90 nm - $\alpha = 0°$ - v = 2 Å /s
3	lift-off	aceton beaker	30' minimum
4	lift-off	ultra-sound bath	1' (10%)
5	rincing	ethanol	
6	drying	nitrogen gun	gun perpendicular to the wafer
7	wafer cleaning	RIE oxygen plasma	«Res» program

Table 3.2: *Spin-coating, insolation and development of UV3 optical resist on MJB3 aligner @ Nanofab*

3.2.2 Superconducting hybrid device fabrication

E-beam lithography process

After that process, the wafer is ready to carry out the first e-beam lithography process. The bilayer made of PMMMA-MAA 33% [2] and PMMA 4% [3] is deposited by following the different steps shown on table 3.3. The bake evaporates solvants and solidifies the polymer.
We pattern the resist by exposing it to a beam of electrons accelerated to 20 keV. The e-beam exposure is done with a LEO 1530 Field Emission Scanning Electron Microscope (FESEM) piloted by a RAITH Elphy plus system. The e-beam lithography is used to write both the fine structure of the pattern, that will define the hybrid superconducting junction circuit within a write field of 120×120 µm², and the wires and bonding pads using a write field of 1 × 1 mm². The typical parameters of the e-beam exposure are

2. ARP 617-09 Allresist
3. ARP 679-04 Allresist

presented in Table 3.3. Because of the pocket diffraction, the electron beam is scattered within the bottom resist layer and it exposes a larger volume than the top layer, where the beam is still well focussed. We tried also a lithography at 30 keV to control the undercut and decrease the proximity effects [15]. After the development the residual resist is cleaned by an oxygen plasma. We first used «Res» program that is directive and fast to etch the resist (∼2 nm/s) then we used «Descum 3» more homogenous with an etching rate of 0.2 nm/s. This a priori insignificant step is in reality important for the lift-off, the quality and the aging of tunnel barriers .

step	process	equipment	parameters / remarks
1	PMMA-MAA 33% diluted in 9% 1-methoxy-2-propanol	spin-coater	2000 rpm - 2000 rpm/s - 60 s ⇒890 nm
2	bake	hot-plate	5 minutes at 180°C
3	PMMA diluted 4% in Ethyl-Lactate	spin-coater	5000 rpm - 5000 rpm/s - 60 s ⇒200 nm
4	bake	hote-plate	30 minutes at 160°C
6	exposure high resolution	LEO 1530 FESEM Raith Elphy+ system	⊘7.5µm, WF : 120×120 µm², i : 20 pA, pixel size : 4.6 nm, v :1.5 mm/s, dose : 230 µC/cm²
7	exposure low resolution	LEO 1530 FESEM Raith Elphy+ system	⊘120µm, WF : 1×1 mm², i : 4.8 nA, pixel size : 60 nm, v : 20 mm/s, dose : 230 µC/cm²
8	development	MIBK/IPA 1:3 beaker	30 s
9	rincing	IPA beaker	10 s
10	rincing	IPA beaker	60 s
11	drying	nitrogen gun	no tweezers gun perpendicular to the wafer
12	resist residues cleaning	RIE oxygen plasma	«Res» program : 2” «Descum 3» program : 2” - 3 10^{-1}mbar - RF power 10W

Table 3.3: *First e-beam lithography step using bilayers*

Metal deposition with lift-off technique

Then the shadow evaporation is done in a UHV e-beam evaporator presented figure 3.2.3. The chamber base pressure reaches 10^{-10} Torr. It is featured to make high quality deposit of niobium, aluminum, copper and silicon at a pressure around 10^{-8} Torr and

to heat the substrate for epitaxial deposit. The load-lock chamber permits very precise oxidations in a large range from 10^{-3} to 1 mbar and to perform ion beam etching.

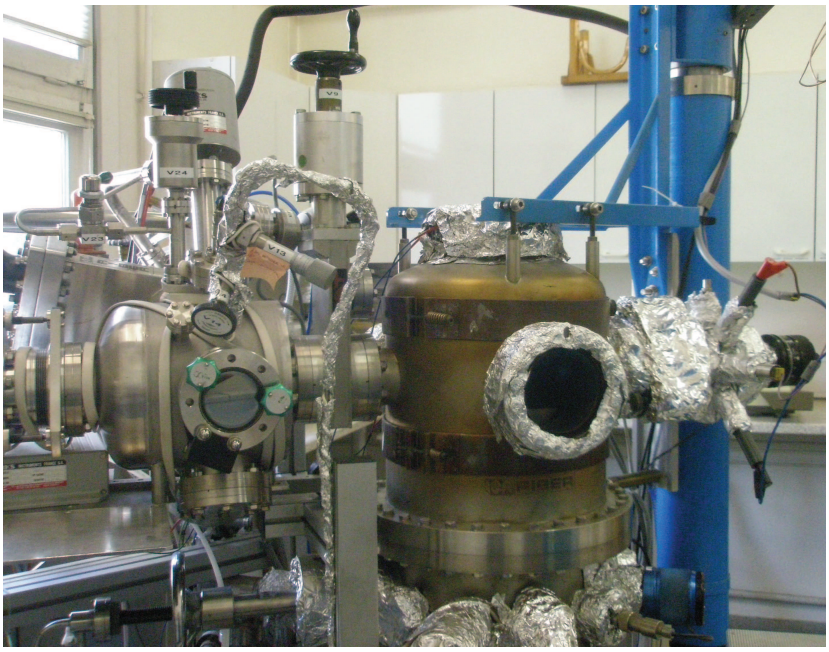

Figure 3.2.3: *UHV system: on the left the load-lock with argon and oxygen lines respectively for IBE and oxidation, on the left the UHV chamber with 4 crucibles and a tiltable sample holder that can be heated.*

Contrary to the usual shadow evaporated scheme, we want to avoid ghost deposits so that the second lithography and deposition work well. Thus we increase the angle of evaporation in order to deposit aluminum on the side of the resist and lift-off it easily. The parameters of deposition and oxidation are presented in the table 3.4. We first deposit aluminum, which is easy to oxidize, giving homogenous tunnel barriers and then the counter electrode, here copper. Notice that it can be interesting for the stability and quality of the tunnel barrier to deposit a few nanometers of aluminum between oxidation and counter electrode [67]. Eventually we deposit silicon with the angle of aluminum and then copper to protect the tunnel junction during the process of the second lithography. For the fabrication of the phonon thermometer sample, the wafer cleaning is followed by a deposition of silicon similar to the fourth step of table 3.4. This silicon layer is used to isolate electrically the bottom from the top circuit and to conduct heat through phonons between the two stages. At this point, half of the sample is realized, which means the stage that we call electron thermometer and cooler. The next section describe the end of «phonon thermometer» samples fabrication, with its upper part containing four N-I-S junctions (a thermometer and a cooler) completely aligned on the bottom circuit.
The process is then similar to the first e-beam lithography process presented in the table 3.3 and the metal deposition in Table 3.4, except the aluminum deposition angle is +50°.

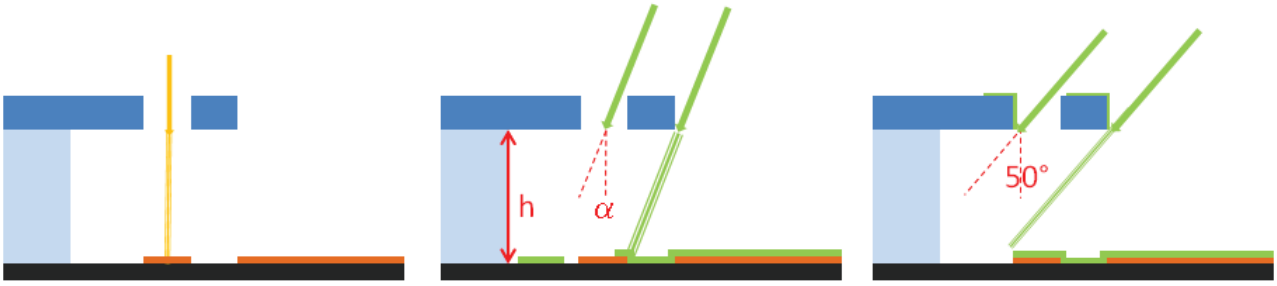

Figure 3.2.4: *Shadow evaporation technique at 0°, small and large angle*

step	process	equipment	parameters / remarks
1	Aluminum deposition	UHV e-beam evaporator	30 nm, angle: -50°, speed: 1 Å/s, current: 200 nA, P: 3.10^{-9} Torr
2	oxidation	loadlock of UHV oxygen line	Pressure : 1.5 10^{-1}mbar - 5 minute
3	Copper deposition	UHV e-beam evaporator	40 nm, angle: 0°, speed: 1 Å/s, current: 90 nA, P: 3.10^{-9} Torr
4	Silicon deposition	UHV e-beam evaporator	30 nm, angle: 50°, speed: 0.7 Å/s, current: 50 nA, P: 3.10^{-9} Torr 20 nm, angle: 0°, speed: 0.7 Å/s, current: 50 nA, P: 3.10^{-9} Torr
5	lift-off	NMP beaker	1 hour at 80°
6	lift-off	Ultra-Sound	1' at 10% of power
7	rincing	ethanol	
8	drying	nitrogen gun	
9	wafer cleaning	RIE oxygen plasma	«Res» program

Table 3.4: *Metal deposition process of the first e-beam lithography*

The shadow evaporation technique enables to fabricate circuits with submicron size tunnel junctions but it reveals to be impossible to make larger junctions without increasing the coupling to the substrate [38]. Although Pekola et al. tried to use mecanical masks [59], presenting a higher distance between the mask and the substrate, to obtain larger tunnel junctions. Researchers succeed in suspending a normal metal beam with tunnel junctions [49, 37, 47, 48, 46], the results are impressive but not a convincing solution to improve significatively electronic refrigeration with tunnel junction. We have devised a process to increase the size of junctions without increasing the surface between the copper and the wafer is called the over-etching technique. We obtain an S-I-N-I-S with a suspended Normal, thus the coupling to the substrate vanishes.

3.3 Etching large area suspended tunnel junction

Comparing with the shadow evaporation approach, the new technique, developped in the following section, tackles the following challenges for N-I-S cooling junctions:
(i) Both electrons and phonons in the normal metal are coupled to the thermal environment that is at a higher temperature. An efficient cooling relies therefore on a thermal decoupling from the environment, including the substrate.
(ii) The heat current from the normal metal to the superconductor is proportional to the tunnel barriers conductance. Reducing the oxide barrier thickness as to increase their conductance leads to the appearance of two-particle Andreev reflection processes at low energy, which deposit heat in the normal metal. A too high junction transparency is therefore prejudicial to cooling. The obvious alternative is to increase the junction area at a constant transparency, which leads however to the next point.
(iii) If not epitaxial, large-area solid state tunnel barriers are subject to local fluctuations of the barrier thickness, which are exponentially amplified in the local current density. In low-quality junctions, most of the current goes actually through so-called pin-holes, giving rise to an unwanted significant sub-gap current.
The new technique shows several other advantages compared to traditionnal lift-off technique. Shadow evaporation starting with patterning the resist gives little room for cleaning the wafer. The resist itself can also pollute the evaporation. E-beam lithography and the thickness of the resist also limit the junction size. On the other hand, the presented fabrication method starts with preparing the multilayer. The wafer can be cleaned by baking in the UHV environment, which, to our belief, is an important factor for the pinhole-free SIN junction [13]. The thickness of the junction can be increased. Geometry on the junction is easily designed. Photolithography and etching technique naturally increase the junction area and reduce time and cost, make the method become more attractive to smaller lab or other industrial applications.
The fact that the normal part in a SINIS structure is suspended is promising. At low temperature, the superconductor is a bad thermal conductor and isolates the normal part on its top from the bath phonon. Attempts on suspending the normal part in

SINIS junctions made with shadow evaporation has been made. In these works, the underneath layer was etched at a high pressure in the Reactive Ion Etching machine. The limitation, however, come from the shadow evaporation itself, which usually limits the size of the device. Although isolating from the bath is believed to bring less noise, research on the role of the suspended layer is still rare at the moment.

3.3.1 Principle and device design

The principle of the over-etching technique is to start from a trilayer Aluminum/Aluminum oxide/Copper thin film on wafer. The bilayer is patterned to obtain the general device structure (contact pads, wiring and holes), then a selective etching [4] is performed to over-etch the aluminum, suspend copper parts. Finally we define the tunnel junctions (shape and size) by etching the copper. The different steps of fabrication are illustrated on figure 3.3.1.

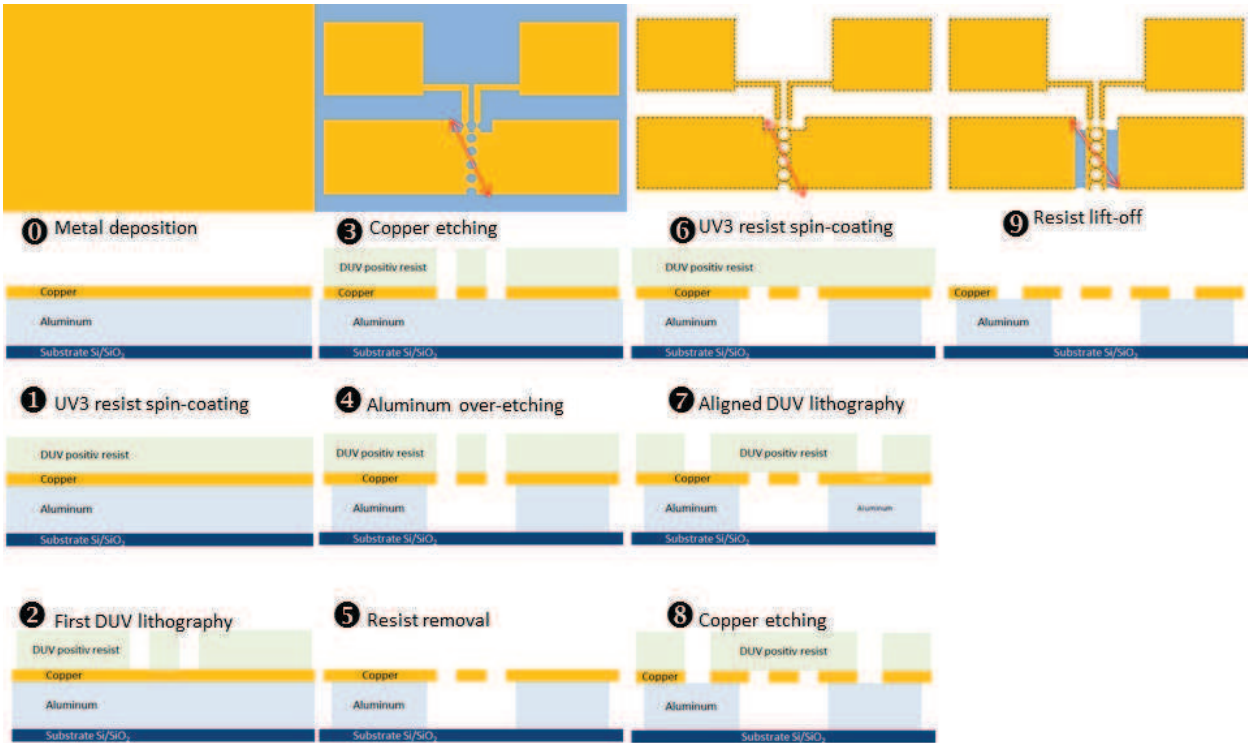

Figure 3.3.1: *The different steps of the over-etching technique. First line (0,3,6,9) are top view of the sample at main steps. Red arrow indicates the cut matching side views of the sample.*

To obtain cooler devices with this technique, we need at least two masks as shown on figure 3.3.2. The method bases on a pre-deposited multilayer of metals, which can be

4. http://www.cleanroom.byu.edu/processes.phtml

prepared at the highest quality. The normal part is suspended in the first lithography, which isolates it from the substrate. The second lithography separately defines the junction area with any geometry of interest.

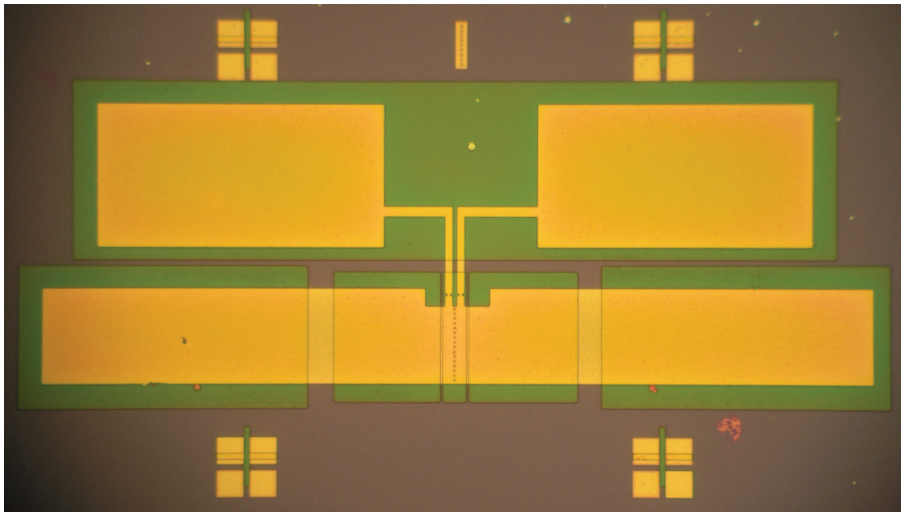

Figure 3.3.2: *Optical masks used to fabricate coolers: in orange the mask defining the general shape of devices contact pads, wiring and holes, in green the mask defining the size of cooler, thermometer probe and quasi-particle traps. The crosses help to align the masks.*

This new process raises few technical and physical questions about the quality of the tunnel junctions [97], the possibility that redeposit shunts the junctions and finally the cooling effects.

3.3.2 Substrate preparation

In the previous part dealing with the lift-off technique, we discussed the importance of the cleanliness of the substrate wafer on the quality of the deposition and the tunnel junctions. The quality and roughness of the substrate is essential since it induces the quality of thin film. Established methods for the removal of organic impurities and native or chemical oxides is a high temperature desorption step, that we perform at 300°C for a few hours. The substrate is then ready for metal deposition.

3.3.3 High quality metal deposition

The quality of thin films is indeed crucial for two main reasons. First is the technical argument of chemical etch process that is a very efficient but invasive method, one needs to insure that the mask, in our case the top layer of copper, is totally insensitive to the chemical etchant. Second is that the quality of thin films and tunnel junctions

oxide should be as good or even better than in devices done with the shadow evaporation technique, since increasing junction area increases the probability of defects and pinholes at the tunnel barrier.
After flashing the wafer we deposit the aluminum in the UHV chamber at 3.10^{-8} Torr at 1 Å/s speed. The wafer is then oxidized in the loadlock at 1 mbar for 15 minutes. The wafer is then placed in the UHV to deposit the copper layer at a pressure of 3.10^{-8} Torr and speed of 1 Å/s. The different to obtain Al/AlOx/Cu multilayer (Fig.3.3.1.0) are summarized in the following table 3.5.

step	process	equipment	parameter / remarks
1	wafer degazing	UHV	T =300°C for 4-8 hours at P=10^{-9}Torr
2	aluminum deposition	UHV	T=100°C, 100 or 400 nm, (v=1±0.5Å/s,α=0°, P=3.10^{-8}Torr)
3	oxidation	loadlock UHV O_2line	P_{SAS}=1 mbar for 15 minutes
4	copper deposition	UHV	T=80°C, 50 or 100nm, (v=1 ±0.5 Å/s,α=0°, P=3.10^{-8}Torr)

Table 3.5: *Parameter of Al/AlOx/Cu thin film multilayer fabrication*

The resistance of tunnel junction depends on the surface of the interface between copper and aluminum. It is also in inverse proportion to the transparency directly linked to the oxidation and in particular the oxidation pressure. After trying different pressures the optimum oxidation parameter is 1 mbar for 15 minutes giving approximately $1\,k\Omega.\mu m^2$.

3.3.4 Optical lithography process

Fabrication of copper bridges

The thin film wafer is coated with DUV positiv resist carefully chosen to not attack copper, aluminum or oxide (Fig.3.3.1.1). A DUV lithography is performed to pattern the raw design (Fig.3.3.1.2) following the different steps of table 3.6.

step	process	equipment	parameters / remarks
1	wafer cutting	scriber	10 pieces of 1.4×1.4 cm^2
2	rincing	aceton	1'
3	rincing	ethanol	1'
4	drying	nitrogen gun	
5	resist deposition «UV3»	spin-coater	4000 rpm - 2000 rpm/s - 30"
6	soft bake	hot-plate	1 minute at 130°C
7	exposure	MJB3 DUV aligner	5.5" (CI 475W)
8	hard bake	hot-plate	2 minute at 150°C
9	development	Microdev/DI (1:1)	1'
10	rincing	flowing DI water	2'
11	drying	nitrogen gun	no tweezers gun perpendicular to the wafer

Table 3.6: *Steps of DUV lithography to fabricate cooler with over-etching technique.*

The insolated polymer is dissolved during the development and leaves the copper exposed. There are two possibilities to remove copper (Fig.3.3.1.3), physical or chemical etching. The first one uses an IBE program that etches copper for 30 seconds and closes the shutter for 30 seconds to prevent resist from being burnt and therefore difficult to lift. It is repeated 20 times and removes 100 nm of copper. This method is well-controlled but slower compared to the chemical wet etching. The wet etching consists of diving the wafer in nitric acid 65% diluted fourty times in DI water. The reaction is very fast and stopped by rincing in two successiv baths of 250 mL DI water.

steps	equipment / parameter	steps	equipment / parameter
IBE etching	Program : "Gravure 400, Hung" 10' for 100 nm of Cu Ar : 2.2 - 2.3 scm	RIE etching	Program "Res" : 10"
		wet etch	HNO_3 65%/DI water 1:40 beaker Cu etch : 30" for 50 nm Cu etch : 40" for 100 nm
		rincing	1^{st} DI water beaker : 30" 2^{nd} DI water beaker : 2'
+	Very well controlled	+	Fast
-	Slow, burns resist, getting hard to remove	-	Less controlled

Table 3.7: *Copper etching : two possibilities either by IBE or wet etch*

The copper bridge are formed by over-etching the bottom aluminum layer with a mixture

of MF-CD 26/ DI water with a ratio of one to two. The etching is nicely controlled afterwards with the optical microscope because of the contrast between suspended copper or copper on aluminum. The reaction is stopped by rincing in two different DI water big beaker, thirty seconds in the first bath and two minutes in the second one. It takes 4'30" to dissolve 100 nm of aluminum and 7'30" for 400 nm. During the attack of aluminum the wafer has to be shacken for the homogeneity of etching and to remove resist residues (Fig.3.3.1.4). The remaining resist residues are removed with a succession of aceton, ethanol baths and RIE each for one minutes. Now the chip presents device with a suspended copper parts (Fig.3.3.1.5). However we still need to define the size and the shapes of junctions.

Shapes and size of S-I-N-I-S definition

For the next step of S-I-N-I-S junctions definition we perform a second optical lithography aligned of the pattern using the alignment marks (Fig.3.3.1.6 & 7). The design allows an error of few microns. The lithography process is similar to the previous one presented in table 3.6. The copper is then removed preferentially by IBE etching since it is more reliable and more precise than wet etch (Fig.3.3.1.8).
However it is also possible to perform an electronic lithography for this step especially to test the importance of the shape of the junction. In this case the lithography process used is similar to steps resumed in table 3.3. After a last lift-off we obtain a tridimimensionnal structure of S-I-N bridge-I-S micrometre size junctions (Fig.3.3.1.9). This helps to study the mecanism of quasi-particles evacuation in the superconductor. Measurements performed on device done with electronic lithography and optical lithography show equivalent results witness of the quality of tunnel junction. The cooler studied presents junctions area varying from 5 µm² to 1000 µm² and the rectangular and crenel-like shape.

3.3.5 High quality of large S-I-N suspended-I-S tunnel junctions

A tridimensionnal structure obtained after such process implies few verifications the control of the undercut, the aspect of bridges, the quality of tunnel junctions and S-I-N-I-S characteristics.

Observation

Fortunately under optical and electronic microscope there is a contrast between copper on aluminum and suspended copper that help us to estimate the undercut and to know the efficiency of the over-etching. At high voltage above 5 keV the hanging copper appears lighter than the copper on aluminum. It is well explained by the diffusion of electron in the material: the more energetic are electron the deeper they penetrate in the metal so that the image reveals not only the surface but also the film underneath. The

figure 3.3.3 shows the SEM image of the cooler at high voltage. The ring around holes matches to the copper undercut of the order of 2-3 µm. The second image is a SEM image of a copper bridge cut by Focused Ion Beam (FIB). The FIB system uses a Ga+ ion beam to raster over the surface of a sample in a similar way as the electron beam in a SEM. The generated secondary electrons (or ions) are collected to form an image of the surface of the sample. The ion beam allows the milling of small holes in the sample at well localized sites, so that cross-sectional images of the structure can be obtained or that modifications in the structures can be made. It allows an accurate control of the progress of the milling. Nanofab instrument combines a SEM and FIB column. The ion beam is mainly used for milling and the electron beam for imaging. The fig. 3.3.3.b demonstrates that aluminum is well-etched, that the copper is not bending.

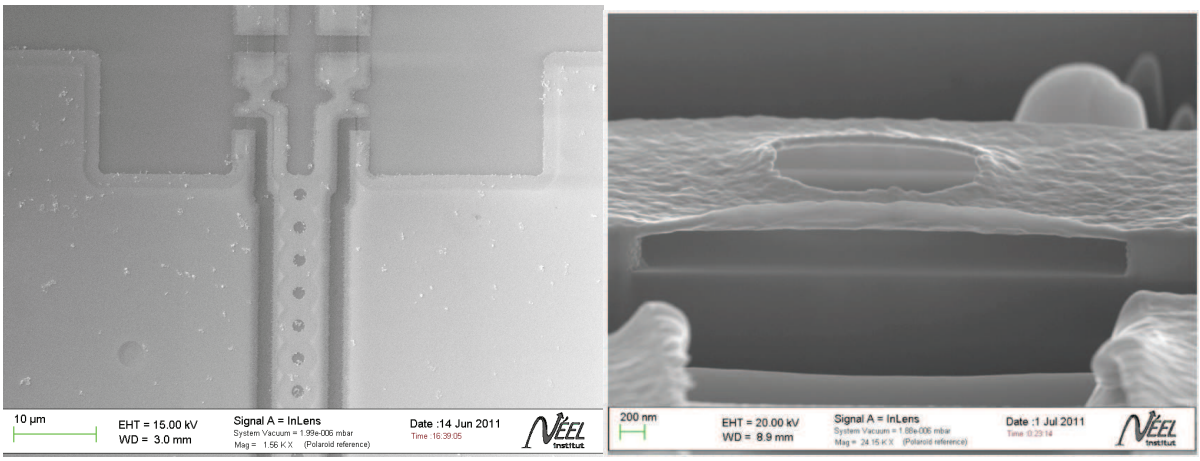

(a) *SEM image of device*

(b) *SEM image of the profile of copper bridge using FIB*

Figure 3.3.3: *(a) SEM image showing regions by decreasing brightness: Cu on Al, suspended Cu, substrate, and bare Al. On top, two thermometer junctions are added. (c) SEM image of a sample cut using Focused Ion Beam showing the Cu layer suspended over the holes region. The thickness of Al and Cu is 400 nm and 100 nm respectively.*

Characteristic

Four points measurements are performed on such devices at He3 and dilution temperatures. It enables to characterize quality of such tunnel junctions. The normal state resistance of junctions in series is typically $2.8\,\Omega$ for 200 µm^2 and the superconducting gap is $2\Delta = 360\,\mu\text{eV}$, the IV-characteristics of the junctions is not an isotherm S-I-N characteristics and show self-cooling effects as well as Andreev heating at very low temperature and bias. The average leakage rate is evaluated to $\gamma = \frac{G_0}{G_\infty} = 3.7 \times 10^{-4}$.

Different parameters of fabrication is studied: the thickness of aluminum and copper, the method for defining the rough design and the shape of junctions. All of these variations do not affect the junction quality, and the leakage rates $\gamma = \frac{G_0}{G_\infty}$ are always in the range of $10^{-4} - 10^{-5}$. A leakage rate below 10^{-4} implies an almost pinhole-free junction. With our large area SINIS junction consistently fall below 10^{-4}, we conclude that the superconductor has a very high quality. It is important to notice that there is no redeposition from different etching processes that may cause a shunt in the junction. The sample does not show any noticeable sign of aging, even stored at room temperature for months.
The figure 3.3.4 shows the differential conductance of a typical junction. We always observed Andreev current below 150 mK. The self cooling effect is also visible. From the slopes of normalised conductance plot, the change in temperature can appear as huge, but more clarification is needed to distinguish it with the overheating in the superconductor.

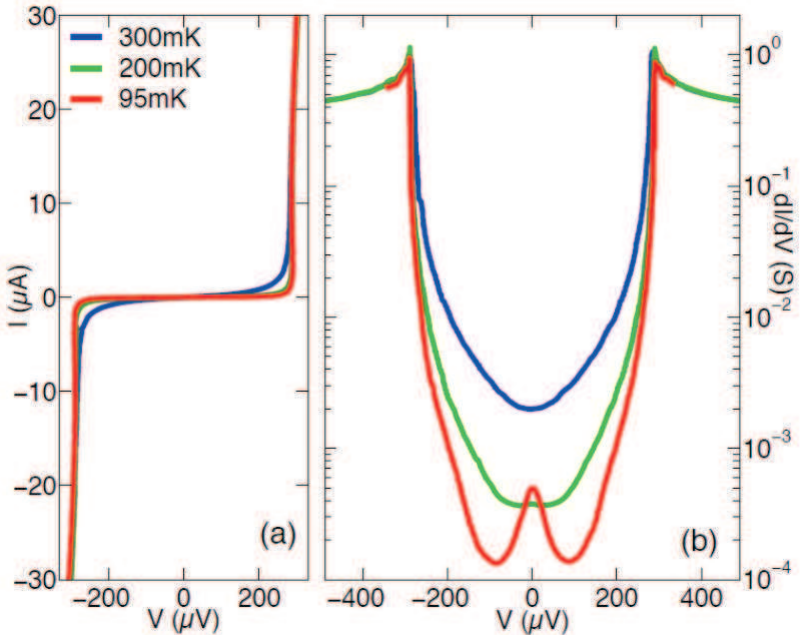

Figure 3.3.4: *(a) Current-voltage characteristic and (b) differential conductance of sample D at different cryostat temperatures, see Table 1 for its fabrication parameters.*

3.4 Conclusion

In this chapter we presented different techniques of fabrication used or developped in our group to study the thermal phenomena in hybrid superconducting devices. The range

of junction that we are able to fabricate goes from $< \mu m^2$ to $>1000 \mu m^2$.
We introduce a novel method to fabricate large-area S-I-N-I-S tunnel junctions with a suspended central normal metal part. The samples are fabricated by combining photolithography and chemical etch of multilayer. The process involves few fabrication steps, is reliable and produces extremely high-quality tunnel junctions. There are many room for improvements with this fabrication method. The aluminum layer can be made epitaxial for an even better quality. The robustness of the multilayer with chemicals give us more options in choosing etching and lithography technique. Other choice of material is possible providing one founds an appropriate way of selective etching (and overetching) the two different materials. In summary, we have presented a method for fabricating large area SINIS junctions from photolithography and overetching technique with a suspended normal metal part. The junctions are electronically high quality, chemically robust and show little aging. The method is reliable and is integrable with other fabrication techniques.
We are also able to design device where the Kapitza and electron-phonon coupling are different and where the quasi-particle evacuation are different from previous experiments.

Chapter 4

Measurements set-up

This chapter presents the cryogenic apparatus used during this thesis as well as the measurement set-up at room and low temperatures.

4.1 Cryogenics

The measurements on S-I-N-I-S devices based on Aluminum as the superconductor need to be done at a bath temperatures lower than the critical temperature of aluminum $T_C^{Al} \sim 1.2K$. Furthermore, the optimum bath temperature for electronic refrigeration is a third of the T_C^{Al}, which means that a Helium-3 system is appropriate to perform electronic refrigeration measurements. However, second order phenomena rising at lower temperature are ponctually worth of studying at lower temperature in a dilution fridge. The following paragraphs present the different systems used.

4.1.1 He3 system with magnetic field

We used a commercial Janis He3 fridge presented figure 4.1.1. It is a closed system working with a charcoal pump. The coolest temperature of 270 mK is reached after a few hours and the typical cycling time is a few days. The complete system, Inner Vacuum Calorimeter (IVC) and dewar, is put under vacuum. We precool to 77 K and then cool to 4K the system by filling the dewar with liquid nitrogen and then liquid helium. When the dewar is filled with liquid Helium, the 1 K pot is pumped to achieve a temperature of 1.1 K. At this temperature, Helium-3 is liquid and falls due to gravity to the cold plate. We heat the charcoal to desorb the Helium-3 gas trapped inside. After the charcoal is cool again, it will pump the He3 bath to achieve the lowest temperature. The minimal temperature of 245 mK can be kept by pumping on the 1 K pot. Nevertheless we can perfectly operate without pump and the minimum stable temperature achieved is then 270 mK.

The temperature of the cryostat is monitored by a TRMC2 linked to thermometers and heaters of the system. There are DT-Cu670B-Cu-diodes on the 1K pot and on the charcoal pot, a ruthenium oxide resistor on the He-3 pot and 25 Ohm resistors on the charcoal and on the Helium-3 pot for heating. Two magnets at the bottom of the dewar surrounding the calorimeter are powered by a Bouhnik power supply controlled by a Labview program. The transversal coil, a solenoid, offers a maximum field of 6 Tesla for 50 A, the Helmoltz coil has a maximum field of 700 mT for 62 A.
The cryostat is wired with Constantan wires of 100 ohm for each line ended by Tyco connectors of six gold-plated contacts (with a negligeable contact resistance) at the bottom and a Jaeger connector at the top. The system is equipped with a microwave line, not used during this thesis. For the experiment, we screw the sample holder to the cold plate and plug the Tyco connectors. Our sample-holder is an updated version of the sample-holder with low temperature filtering embedded developped during the thesis of E. Serret and F. Balestro [4, 81]. Every electrical contact can be shunted with a 1 Mohm resistor to the ground during the manipulation and microbonding. We glue our sample on a chip with GI vanish that can be easily removed with aceton.

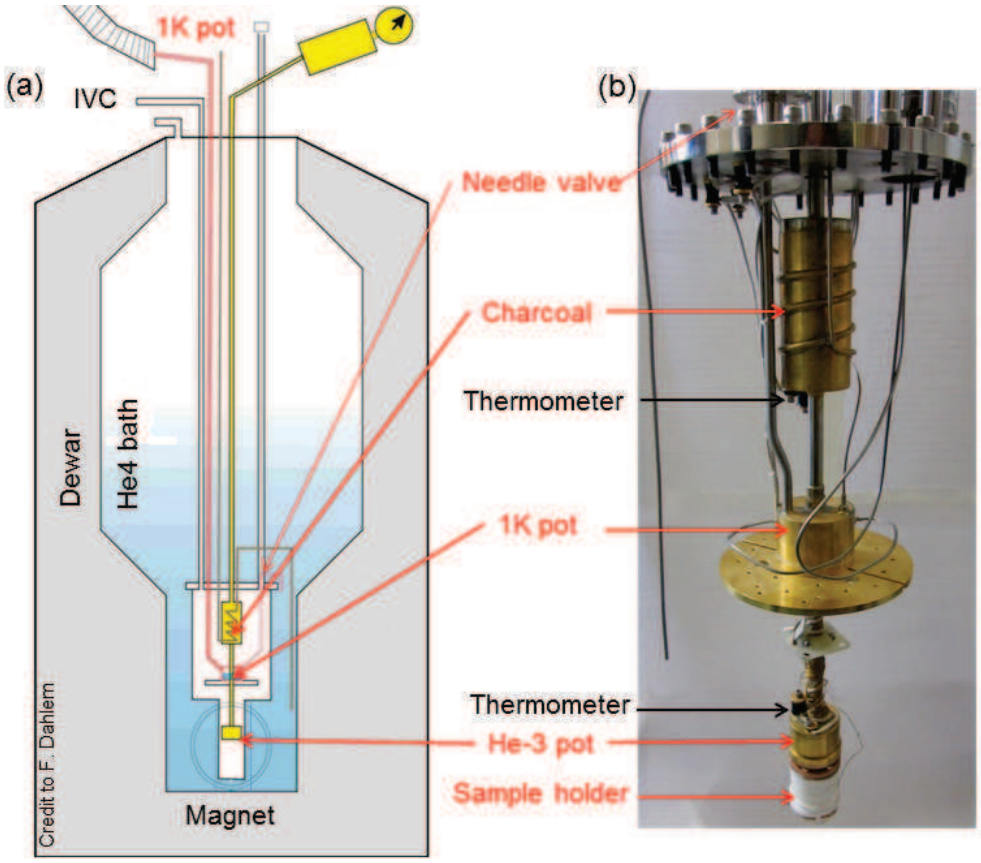

Figure 4.1.1: *(a) Schematic of the Janis Helium-3 system. (b) Picture of the IVC*

Most of our measurements are done in this set-up, however it features only two axes coils.

4.1.2 Inverted dilution system with three axis coils

The magnetic field effects on quasi-particles relaxation have been studied in Wernsdorfer's Sionludi including three-axe coils as described figure 4.1.2. A Sionludi, speciality of CNRS Grenoble first designed by A. Benoit and M. Caussignac, is an upside-down dilution fridge presenting the cold plate at the top. This design presents an important cooling power and a spacious cold plate of 13 cm diameter and 13 cm high, which is interesting to place coils and filtering. It operates at a high flow of He3/He4 mixture to cool down from 300 K to 1K. It presents five stages of thermalisation from 300K at the bottom to 1K at the top and the cold plate can reach a temperature below 30 mK.

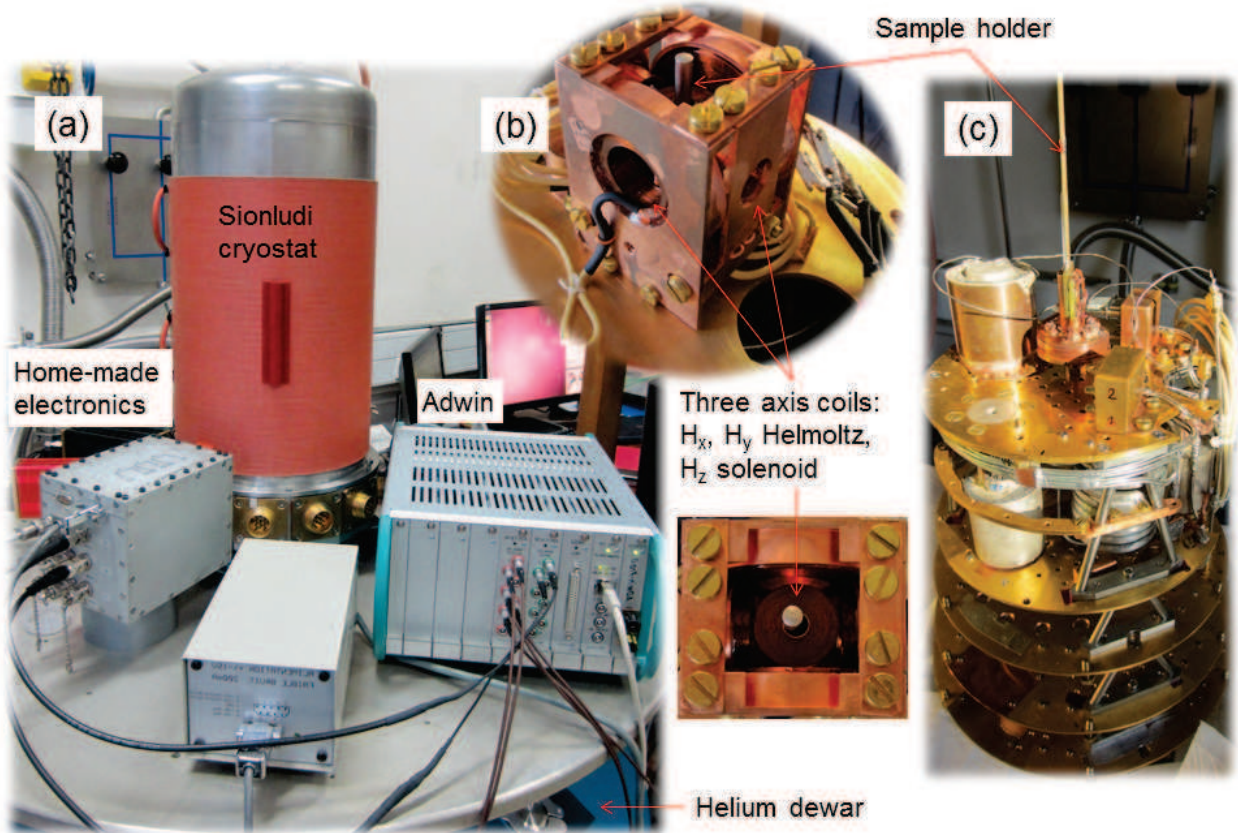

Figure 4.1.2: *(a) Complete set-up : electronics connected to the ADWIN interface, Home-made electronics with high impedance current sources inputs and voltage amplifier outputs, Sionludi. (b) Three-axe magnetic field coils: two Helmholtz and one solenoid. (c) Open Sionudi with including filtering.*

4.2 Measurements set-up

Before cooling down, we need to characterize the sample to verify that it presents all the characteristics required to study the phenomena of interest. The sample is first observed under SEM to know if the sample presents any disqualifying characteristics as an obvious short-cut or an open circuit. Since our device are made of tunnel junctions of the order of kiloOhm, their characteristics can be checked even at room temperature and at each step presented in the following sections.

4.2.1 Room temperature measurements

Probe station

The probe station on figure 4.2.1 is a characterization tool made of a binocular microscope and needles connected to a floating voltage source and a multimeter. As pictured on figure 4.2.1(b), when the needles are out of contact, the voltmeter measures V_0, which is usually 10 mV. Then we place the needles on the pads, and the voltmeter measures V between sample's terminals as shown on on figure 4.2.1(c). Following the circuit presented figure 4.2.1, the resistance of the sample R is then close to $\frac{V}{V_0}.200k\Omega$. This step allows us to choose which sample deserves to be microbonded.

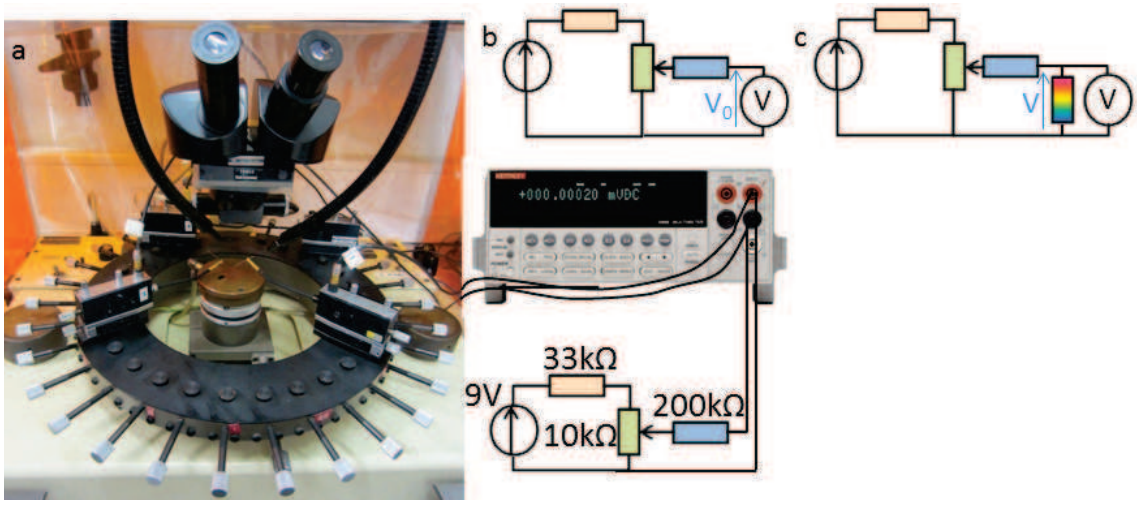

Figure 4.2.1: *(a) Probe station set-up; (b) Without sample: V_0 measurements; (b) With sample: V measurements*

Micro-bonding

The micro-bonding machine comes from Westbond company. According to the force applied by the tool, the ultrasonic-soldering power and the time, an aluminum wire going through the needle is soldered on each pad of our sample. With the phonon

thermometer sample, it is difficult to see the pads because of the silicon layer, so an extra light aside helps to localize properly the edges of pads. At this point, the sample on the chip is placed on our sample holder shunted with a network resistance of 1 MΩ, whereas the tunnel resistances are between 1 and 100 kΩ. We check that the junctions survive the microbonding with the hand-held synchronous detection supplied by a $9\,V$ battery and limited to 20 nA. The voltage response is linear for our range 500 Ω - 5 kΩ of resistance.

Room temperature measurements

Eventually, we fix our sample holder shunted with the sample microbounded at the bottom of the IVC. We previously check the wiring of the cryostat and the electronics is grounded. At this point, the sample is double grounded. The shunt of the sample holder is taken away and we verify with appropriated electronics each resistance. Doing a «two-wire measurement», we need to consider also the cryostat wiring resistance of 200 Ω. If all the resistances present suitable values, we cool down or we connect another sample.

4.2.2 Low temperature measurements

The sensitivity of our sample in respect of the temperature and the electronic noise can be useful to verify a set-up in terms of filtering, thermalisation and electronics. On the other hand investigations of thermal effects in such devices necessitate to hunt parasitic noises (electric, mecanic) and pay attention to the thermalisation. Indeed at the beginning of my work I had trouble to see clearly the aluminum gap at 500 mK because of the voltage source used at that time. This led us to develop and use a home-made electronics of three current sources powered on battery. We have also done efforts in the electronic filtering.

Filtering

Measuring superconducting hybrid devices means to use low currents of the order of 10 picoamperes in the subgap regime, which requires efforts to avoid electronic noise. Such small currents can be perturbated by electromagnetic RF or low frequency noise coming from different apparatus and environment. To decrease the electromagnetic noise, the compact electronics box is directly connected to Pi-filters. It is also connected to a NI-DAQ voltage source and acquisition card through twisted shielded BNCs. The electronic filtering of our set-up is composed of three stages as described on figure 4.2.2-a. At room temperature, a Pi-filter (R = 1 kOhm, C = 220 pF, L = 470 µH) acts as a low-pass filter with a cut-off frequency of 4 MHz. At low temperature, on the sample-holder, wires twisted in pairs go through 200 cm of a CuNi capillary filled with Ecosorb an elecromagnetic paste introduced by Siddiqui and al [83]. This ensemble cuts electrical

signals with a frequency above 200 MHz. Finally, capacitance feedthroughs close to the sample have a cuf-off frequency of 2 MHz. Figure4.2.2-b shows the home-made sample holder with the integrated filtering. Furthermore, to avoid a ground loop, the electronics designed to include three-current sources can be supplied with batteries. This electronics is described more precisely in the next paragraph.

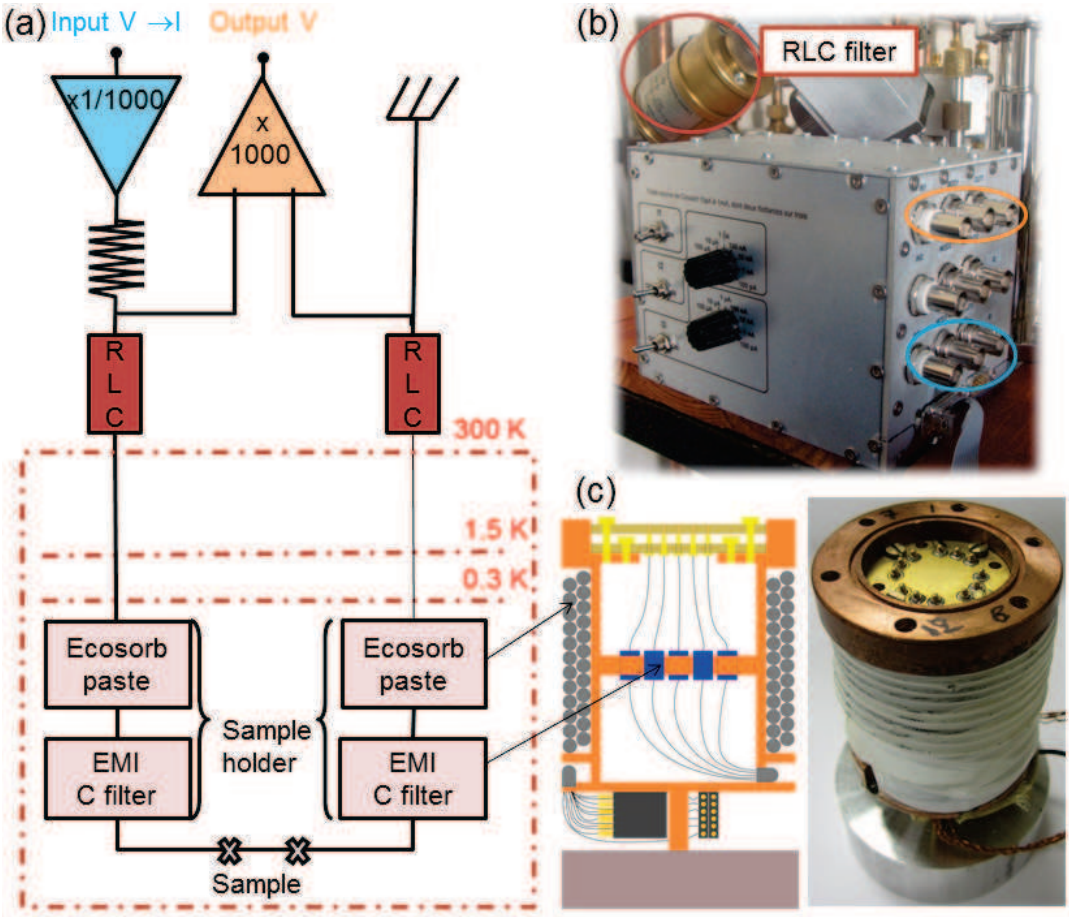

Figure 4.2.2: *Schematic of filtering stages*

Floating sources and high impedance DC electronics

The «phonon thermometer experiment» aims at studying the electron-phonon coupling by cooling or heating the normal metal through cooler junctions and measuring simultanously the electronic temperature of both circuits. It requires an appropriate low-loise, low-current, DC electronics without any ground loop. To do so, the electronics is powered from a battery or a low-noise power supply decoupled from the circuit by a couple of LEDs and photo-batteries. Based on pre-existing electronics, the new electronic box presents one remotable current source (n°1) that imposes the ground of the circuit and two floating current sources (n°2 and 3). In the electrical circuit of the loatting sources,

the voltage is measured before and after the $R_{polarisation}$ in order to control the current bias. A simplified electrical circuit of the different types of current source is presented on Figure 4.2.4, their complete circuits are described in the Annexe. All sources shown on figure 4.2.3.a feature:
- a voltage-current converter from 100 pA to 1mA, thanks to a set of resistances of biased $R_{polarisation}$. This wide range of current allows us to measure precisely the curent-voltage curve inside the gap. The resistance of our device changes from kiloOhm to more than MegaOhm in the gap. We stick to the regime where $R_{polarisation} >> R_{sample}$.
- a modulation input to apply a current modulation,
- a voltage amplifier of 1000 followed by a loss-pass filter.
For source n°1, the change of current range is remotely controlled by a Labview program that modifies the state of the relay selecting the $R_{polarisation}$. Concerning source n°2 and 3, the resistance of biased $R_{polarisation}$ is selected manually.
An other specificity of this box is that a connection matrix ensures a great flexibility of measurements. The matrix is made of two stages of gold stripes in perpendicular directions, separated by an insulator array. The connection between the two stages is established by gold pins. The current I+ and I- and voltage V+ and V- lines are connected to columns inputs of the matrix, whereas its lines outputs are connected to cryostat wires leading to the sample.
With this electronics, we are able to measure simultanously the current-voltage caracteristics of different junctions of a device, while under biased or not, with or without magnetic field. We present in the following paragraph the different and complementary ways to measure our devices.

4.3 Measurements

Precise measurements

To extract the electronic temperature experimentally, we measure the current-voltage characteristics (IV) for different ranges of current of bias, so that one isotherm curve is a superposition of several IV curves of different ranges. We then derivate numerically the IVs using a routine that acts also as a numerical filter. We then obtain a differential conductance that we fit with the theoretical expression of the derivative of the current through a N-I-S junction with respect to the voltage. In this way, we extract the electronic temperature T_e as described on figure 4.3.1. We repeat the measurements for different temperature and different parameters.

Fast measurements

Measurements are performed with our home-made electronic described previously in combination with an Adwin allowing real-time measurement [74]. The script is written in Javascript in the Nanoqt environment developped by E. Bonet and C. Thirion. First,

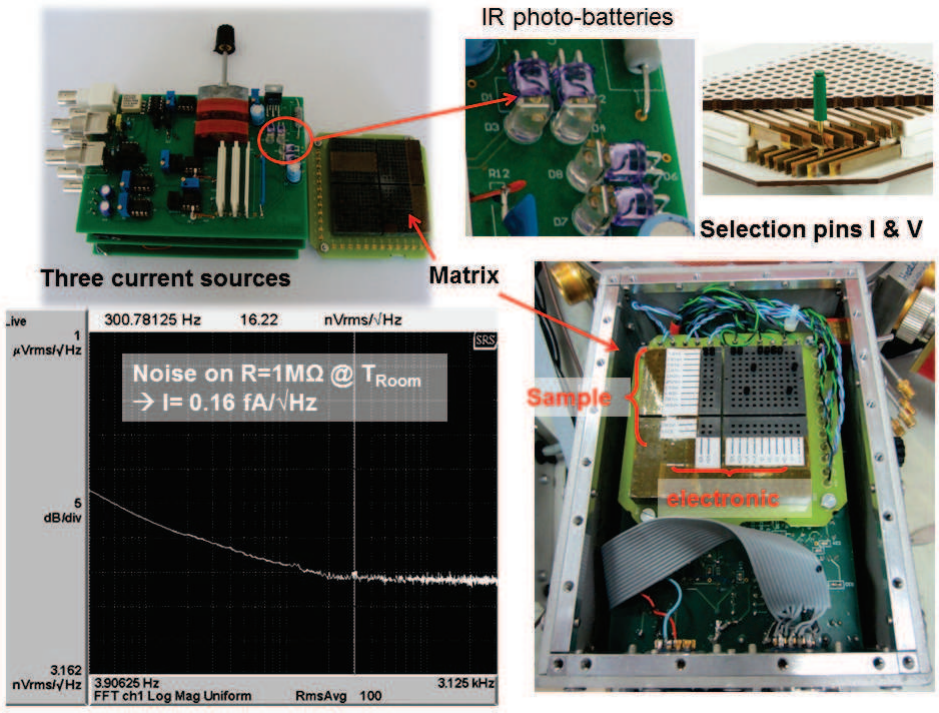

Figure 4.2.3: *(a) Stacked electronic boards of our current sources on the left and the matrice on the right (b) LED and Infrared photobattery decouple the electronics from the power supply ground. (c) Cut image showing the principe of a matrice (d) Noise of the electronics at room temperature for R =1 MΩ, I=0.16 fA/$\sqrt{Hz}$ above 100 Hz (e) Top view of utilized electronics.*

the entire IV characteristics of each junction is measured at low temperature in order to verify the quality of the junction, to fix the current of the thermometer at a relevant value, to find the optimum cooling range and the match between the electronic temperature and the temperature from the cryostat thermometers. After this first check, we for example choose to fix the current of the thermometer I_{th}= 5 nA for sample a2.5b10c5. We then sweep the current of the cooler I_{cooler} for different fields and measure the response of the thermometer and cooler respectively V_{th} and V_{cooler}. Thanks to the measurement of the thermometer V_{th} versus T_{bath}, at a given I_{th}, we know the calibration between V_{th} and T_e. We then obtain the dependance of V_{th} on I_{cooler} for different values of B,θ,φ et T_{bath}.
We calibrate the electronic thermometer by measuring the evolution of V_{th} when the junction is polarized at $I_{th} = 5nA$ and we vary the bath temperature. Figure 4.3.2.a shows V_{th} versus I_{cooler} when the thermometer is current polarised at $I_{th} = 5nA$. For $I_{cooler} = 0$, V_{th} gives the electronic temperature equilibrate to T_{bath}. When we sweep the current of the cooler the increase of V_{th} demonstrate a drop of the electronic temperature. Considering the IV characteristics of the cooler 4.3.2.b we can express V_{th} in function

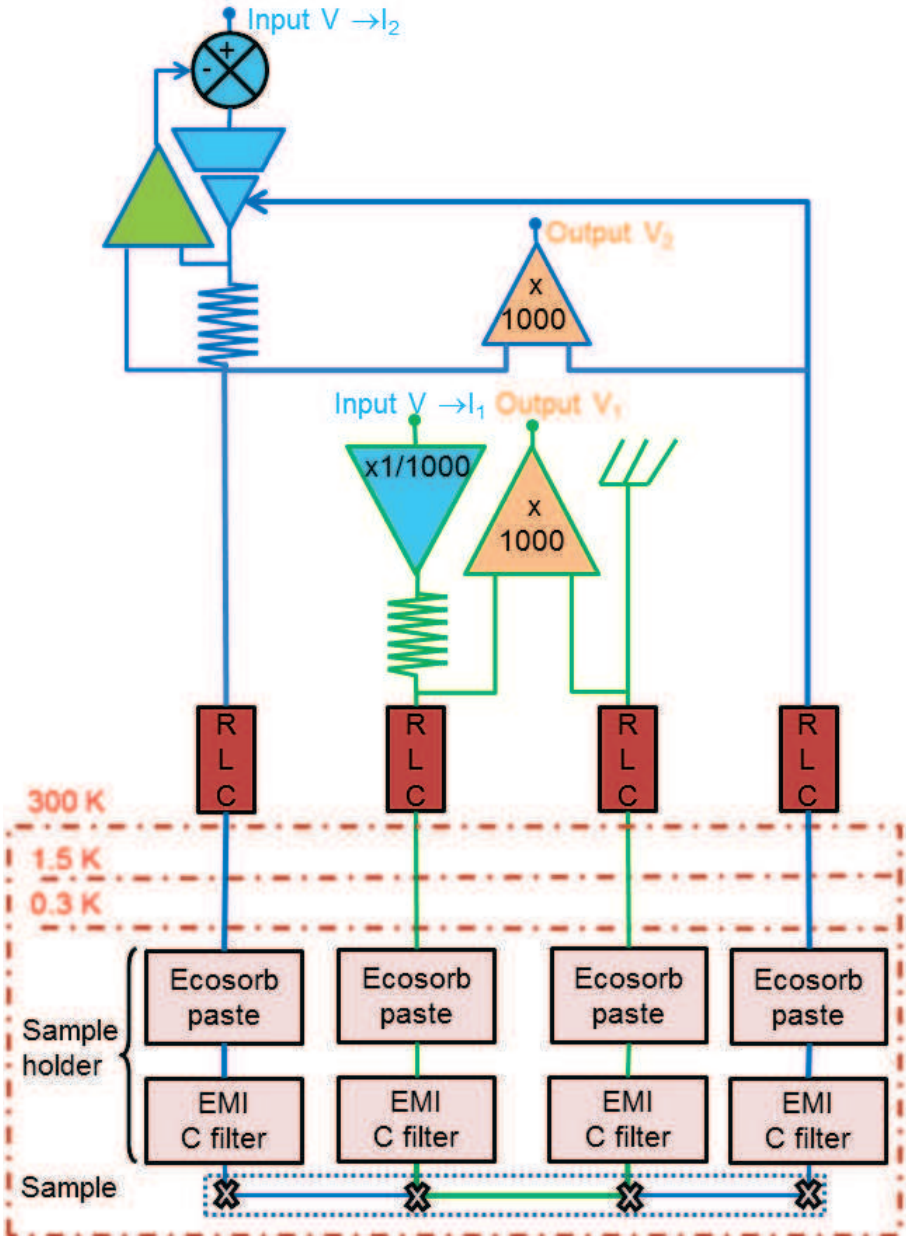

Figure 4.2.4: *Schematic of the entire measurement circuit: the green circuit is the remote current source circuit, which defines the voltage reference, and the blue circuit is a floating current sources circuit.*

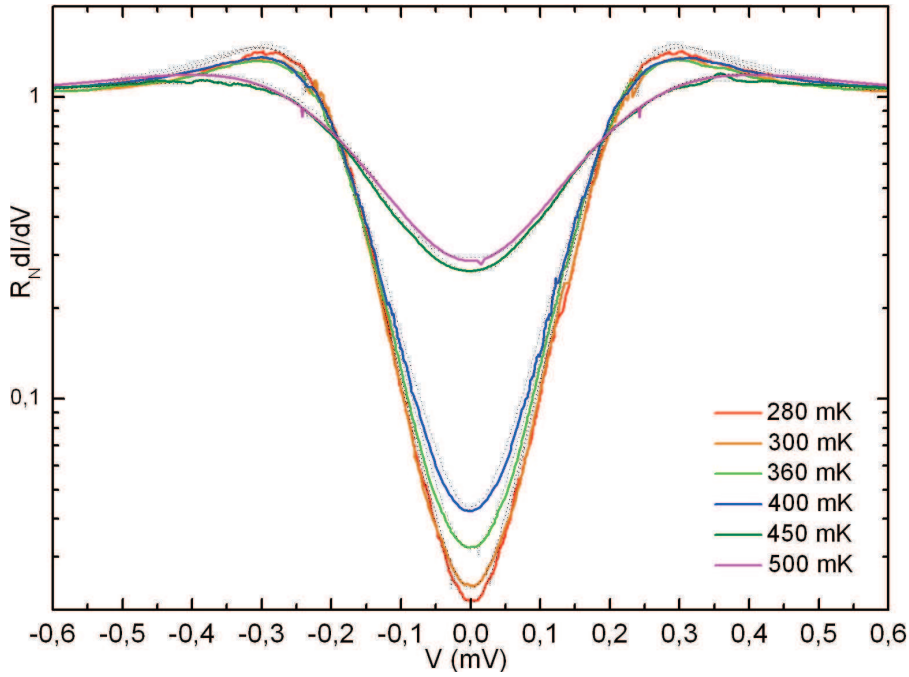

FIGURE 4.3.1: *Experimental normalised conductance (continuous colorfull lines) fitted with isotherm (black dotted lines) to extract the electronic temperature, for different bath temperatures.*

of V_{cooler}. The curve V_{th} vs I_{cooler} are recorded for different value of the perpendicular magnetic field H_y. The plot maps of the electronic temperature ($T_e \propto \frac{1}{V_{th}}$) vs I_{cooler} in x-axis and H_y in y-axis.

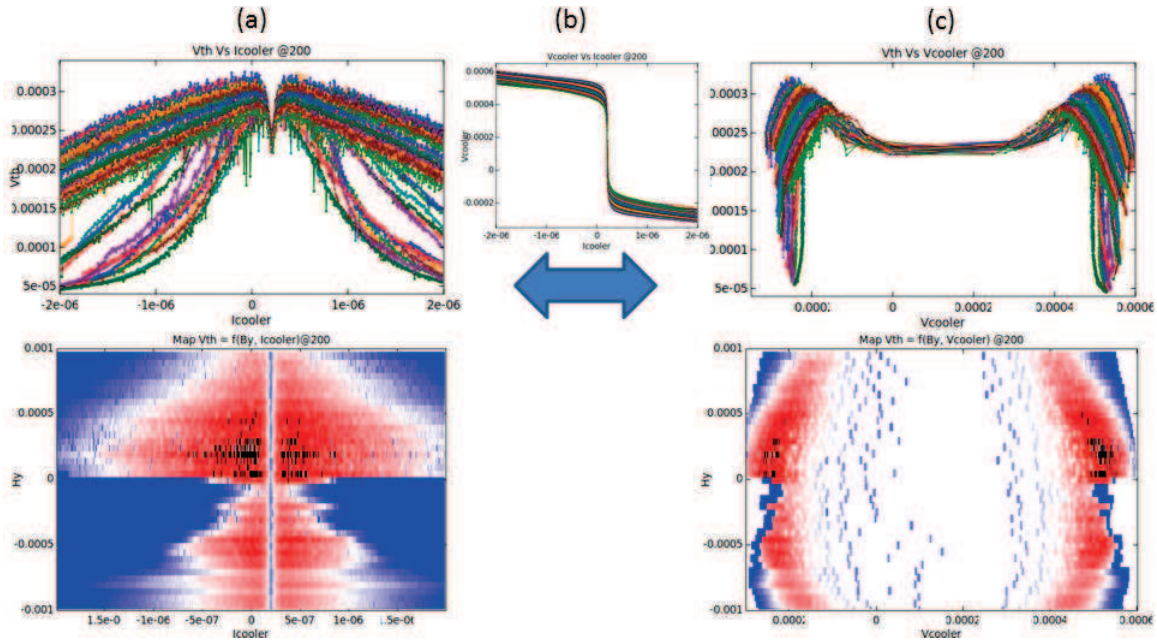

FIGURE 4.3.2: *Sample a10b10c10 : Biased thermometer I_{th} = 5 nA. (a) V_{th} vs I_{cooler} for different magnetic field. (b) V_{cooler} vs I_{cooler} for different B. (c) V_{th} vs V_{cooler} for different B.*

4.4 Conclusion

DC measurements at low temperatures require to be careful on the electromagnetic noise and ground loops. The electronics developped during this thesis is not a original idea but more flexible, faster, more convenient, more precise and more compact than the previous one. The measurement method that we use is also balanced between efficiency and precision. When I started my PhD, I was doing IV characteristics of only one S-I-N-I-S junctions for a given bias, selecting the range manually with a noisy characteristics. Now we can use a new electronic set-up able to measure simultanously two S-I-N-I-S junctions for a given bias of the cooler. The noise is reduced, and ground loops are reduced too. Now we use Labview program with a NI-DAQ or NanoQt with an Adwin to change of current ranges and currents through magnets.

Chapter 5

Thermal couplings in a mesoscopic metal

5.1 Introduction

Electrons in a metal are coupled to the environment mainly through phonons. Previous experiments revealed that electronic refrigeration can also cool down phonons. As discussed in Chap. 1, Rajauria et al. proposed a comprehensive thermal model of electronic cooling, taking into account phonon chilling. However, the lack of a direct phonon temperature measurement can cast some doubt on the model's validity. Thus we have designed a new experiment, called «phonon thermometer experiment», aimed at measuring directly the phonon heating or cooling simultaneously to electron temperature measurement, under heating or cooling.
In this chapter, we will first introduce the thermal model and the purposes of the experiment. Secondly we present the conception of the experiment, especially the hypotheses to verify, the comparison of the different thermal couplings involved, and experimental parameters. We will then present our experimental results. Afterwards, we will compare these results to various possible models and finally with our full thermal model. In particular, this will enable us to verify its validity on a wide range of injected power. This will give us access to the electron-phonon power as well as to the Kapitza coupling.

5.1.1 Thermal model

The thermal model for electronic refrigeration in a micro-cooler [70] is presented in Figure 5.1.1. It takes into account electron-phonon and Kapitza couplings to describe the electronic temperature evolution for a given cooling power P_{cool} or heating power P_{Joule}. Initially proposed in the cooling regime, we extend, in this thesis, the thermal model to the heating regime.
By biasing the $S-I-N-I-S$ junction (blue arrows on Fig.5.1.1), a heat current

P_{cool} flows from the Normal metal to the Superconductor and induces an electronic temperature drop in the Normal metal for a voltage bias below the gap $eV < \Delta$. When the $S - I - N - I - S$ junction is biased at a voltage larger than the gap $eV \gg \Delta$, the heating regime is achieved.

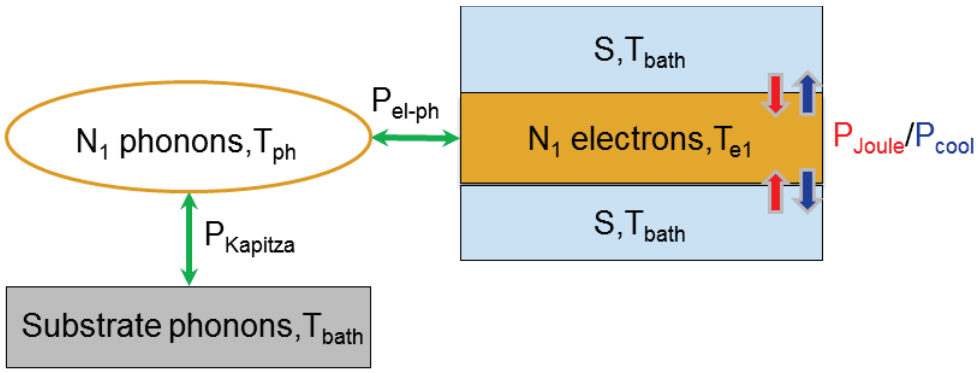

Figure 5.1.1: *Thermal model for electron and phonon cooling in a micro-cooler*

At thermal quasi-equilibrium in the normal metal N_1, the power that is injected P_{Joule} or extracted P_{cool} is compensated by thermal couplings such as electron-phonon coupling and the Kapitza resistance.
Electrons are coupled to the metallic lattice through electron-phonon coupling that in a bulk metal follows a T^5 law:

$$P_{el-ph} = \Sigma V(T_e^5 - T_{ph}^5) \tag{5.1.1}$$

where V is the volume of the normal metal, and Σ is the electron-phonon coupling constant, which is material-dependent. For bulk copper, $\Sigma \sim 2\,\mathrm{nW}.\mu\mathrm{m}^{-3}.\mathrm{K}^{-5}$.
Phonons of the metal are coupled to the phonons of the substrate through a Kapitza resistance. This thermal resistance is due to the lattice mismatch at the interface between the metal and the substrate. In our case, we consider a T^4 law:

$$P_{Kapitza} = KA(T_{ph}^4 - T_{bath}^4) \tag{5.1.2}$$

where A is the contact surface between the normal metal and the substrate, and K is the Kapitza constant. K varies with material and interface quality. In Ref. [70], a value $K = 44\,\mathrm{pW}.\mu\mathrm{m}^{-2}.\mathrm{K}^{-4}$ was found for a silicon-copper interface similar to ours. At mesoscopic scale, surface effects are gaining importance with respect to volume effects, thus the Kapitza resistance can be sizeable.
The thermal model is summarized by the following system equations:

$$\begin{cases} P_{Joule}(T_e,\, T_{bath},\, V) + P_{el-ph}(T_e,\, T_{ph}) = 0 \\ P_{el-ph}(T_e,\, T_{ph}) + P_{Kapitza}(T_{ph},\, T_{bath}) = 0 \end{cases} \tag{5.1.3}$$

Contrary to Ref. [70], we focus here on the heating regime since the accessible power range is wider and the experiment gives a larger temperature difference. We will inject a Joule power P_{Joule} in the normal metal and study the thermometers response.

5.1.2 Objective

The «phonon thermometer experiment» is performed to understand better the different thermal couplings between electron and phonon baths in a mesoscopic device. In particular, we will focus on the electron-phonon coupling and Kapitza coupling. We will study a thermal regime where we can not approximate the phonon temperature to the bath temperature, in contrast to hot electron experiments [76, 75, 94, 95, 86]. We will investigate the validity of our thermal model by measuring independently phonon T_{ph} and electron temperatures T_e. This will enable us to determine the power law and the prefactor of the different thermal couplings.

5.2 Experiment conception

5.2.1 Hypotheses

Our model is based on the following assumptions:

– As discussed in section 1.3.1, we consider that the electronic bath is at thermal equilibrium. Magneto-resistance experiments on a Copper wire made from our sample's source [1] have been previously pursued in our team. The dephasing time τ_ϕ obtained by a fit using the weak localization theory [8] was 150 ps at 275 mK.

Parameters	Copper 1	Cooper 2
$R_N\,(k\Omega)$	16	130
$t\,(\mu m)$	0.045	0.045
$l\,(\mu m)$	18	3
$w\,(\mu m)$	0.3	0.3
$\Gamma\,(s^{-1})$	4.10^6	5.10^6
$\tau_\phi\Gamma$	6.10^{-4}	8.10^{-4}

Table 5.1: *Values of the phonon thermometer sample parameters relevant for the validity of quasi-equilibrium conditions: normal-state resistance R_N, thickness t, length l, width w, injection rate Γ, product of the injection rate and dephasing time $\tau_\phi\Gamma$.*

Here we assume that the phase coherence time τ_ϕ and the inelastic scattering are of the same order. Out-of-equilibrium in a metal coupled to electrodes though tunnel

1. Cu of 6N purity (99.9999\%)

junctions can be characterized by the product $\tau_\phi\Gamma$, where Γ is the injection rate introduced in Eq. 1.3.1. According to the $\tau_\phi\Gamma$ values shown in Table 5.1, electron baths of each metal island are at thermal quasi-equilibrium, characterized by an electronic temperature T_e.

– In order to consider a Kapitza resistance, we need to be able to define a distinct population of phonons between the metal and the substrate. A population of phonons in a film of thickness d is defined by building wave packets including phonons with wavelengths at least as short as d. It requires a temperature $T \gtrsim \frac{\hbar v_s}{2k_B d}$ where v_s is the sound velocity. In copper $v_s \simeq 5 \cdot 10^3\,\mathrm{m.s^{-1}}$. For $d = 100\,\mathrm{nm}$, it means $T \geq 190\,\mathrm{mK}$, for $d = 30\,\mathrm{nm}$, it means $T \geq 640\,\mathrm{mK}$, and $d = 45\,\mathrm{nm}$, it means $T \geq 430\,\mathrm{mK}$. In order to define a N-metal phonon temperature different from the substrate phonon temperature, the total thickness of the sample should then be of the order of 100 nm at 300 mK. The sample characteristics are thus a trade-off between fabrication ease and the above requirements for a bulk phonon system.

5.2.2 Measurement of distinct population temperatures

Our experiment is extended from hot electron experiments. Similarly to these experiments, we inject a given power in a normal metal N_1 and probe the electronic temperature by S-I-N-I-S junctions. The power is calculated from the current injected. The experimental principle is schematized by its thermal model in Figure 5.2.1.
The specificity of this experiment is that we add a copper island N_2 on top of the heated normal metal N_1. A S-I-N-I-S junction is used to probe the electronic temperature N_2. The N_2 island is galvanically decoupled from N_1 by a silicon oxide layer. The N_2 island can only be heated through electron-phonon coupling. Thus, without other source of heat and assuming non-perturbative temperature measurements, N_2 electrons are thermalized to N_2 phonons. Thus, in the rest of the chapter we will refer to the electronic thermometer on island N_2 as phonon thermometer.

5.2.3 Electron-phonon coupling vs Kapitza resistance

We first consider the limit of a strong Kapitza coupling represented on Fig. 5.2.2a. The phonons of the Normal metal are then thermalized to the bath temperature, $T_{ph} = T_{bath}$. The electron-phonon coupling is thus predominant on the electron temperature T_e behavior, which can be expressed as:

$$T_e = \sqrt[5]{P_{ext}/\Sigma V + T_{bath}^5} \tag{5.2.1}$$

where $V = l.w.t$ is the volume of the Normal metal.
We can also consider the limit of strong electron-phonon coupling, represented on Fig. 5.2.2b. Phonons and electrons of the Normal metal and electrons are then at the same temperature, $T_e = T_{ph}$. The Kapitza coupling is thus predominant on the electron temperature

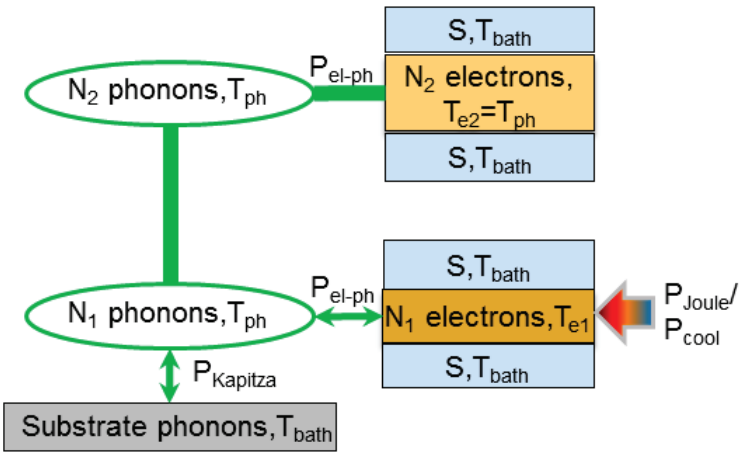

Figure 5.2.1: *Complete thermal model of the phonon thermometer experiment*

T_e behavior, which can be expressed as:

$$T_e = \sqrt[4]{P_{ext}/KA + T_{bath}^4} \tag{5.2.2}$$

where $A = l.w$ is the area of the interface between the Normal metal and the substrate.

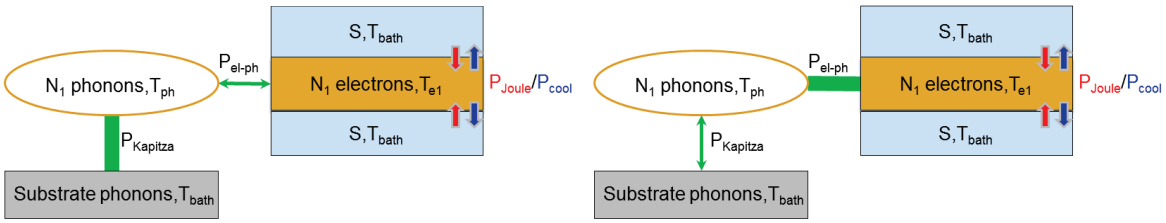

(a) *Strong Kapitza coupling* (b) *Strong electron-phonon coupling.*

FIGURE 5.2.2: *Limiting cases of the thermal model.*

Let us now compare the electronic thermal behavior expected from these two laws for sample parameters close to the ones that we will use: $T_{bath} = 0.3\,\mathrm{K}$, for a copper wire (length $\mathrm{l} = 70\,\mu\mathrm{m}$, width $\mathrm{w} = 0.3\,\mu\mathrm{m}$, thickness $\mathrm{t} = 0.03\,\mu\mathrm{m}$) with $\Sigma = 2000\,\mathrm{pW}\mu\mathrm{m}^{-3}\mathrm{K}^{-5}$, $K = 80\,\mathrm{pW}\mu\mathrm{m}^{-2}\mathrm{K}^{-4}$.

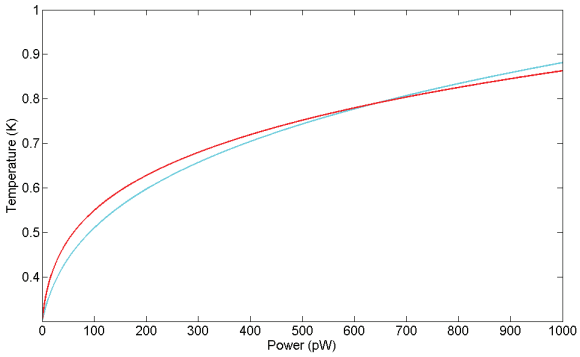

Figure 5.2.3: *Calculated electronic temperature versus injected power in the case of a Kapitza coupling bottleneck (blue) and an electron-phonon coupling bottleneck (red) for parameters* $\Sigma = 2000\,pW\mu m^{-3}K^{-5}$, $K = 80\,pW\mu m^{-2}K^{-4}$, *length* $= 70\,\mu m$, *width* $= 0.3\,\mu m$, *thickness* $= 0.05\,\mu m$ *and* $T_{bath} = 0.3\,K$.

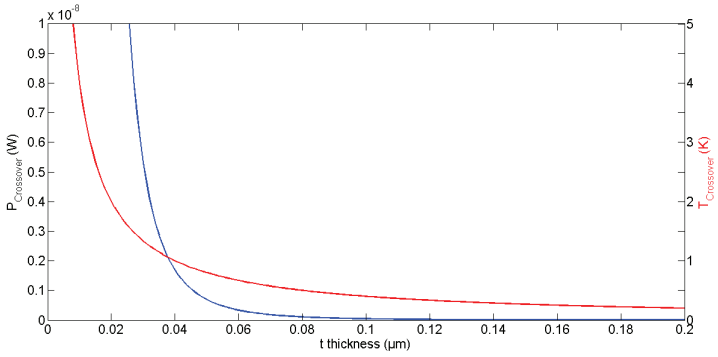

Figure 5.2.4: *Crossover temperature* $T_{crossover}$ *and power* $P_{crossover}$ *evolution with the thickness t for parameters:* $\Sigma = 2000\,pW\mu m^{-3}K^{-5}$, $K = 80\,pW\mu m^{-2}K^{-4}$, *length* $= 70\,\mu m$, *width* $= 0.3\,\mu m$, *and* $T_{bath} = 0.3\,K$.

The two curves in Figure 5.2.3 displays the evolution of T_e as a function of injected power P_{ext} in the two limits of a strong Kapitza (Eq. 5.2.1) or strong electron-phonon coupling (Eq. 5.2.2). Comparing the two laws is interesting in order to weight the influences of bath temperature and sample geometry on the thermal evolution. Albeit the two plots are quite close, we observe that the thermal behavior at low power is dominated by a $P^{1/5}$ related to electron-phonon coupling. A $P^{1/4}$ law related to Kapitza resistance is observed at high power. The difference of power exponent between electron-phonon and Kapitza coupling features a cross-over between these two laws at a given bath temperature depending of the device characteristics. The power at the crossover is given by $P = \frac{K^5 A}{\Sigma^4 d^4}$ and at a temperature of $T = \frac{K}{\Sigma d}$. The temperature $T_{crossover}$ and power $P_{crossover}$ crossover evolution with the thickness t is shown on Fig. 5.2.4. Both quantities decrease with the thickness of the metal. With commonly admitted values

of $\Sigma = 2000\,\mathrm{pW}\mu\mathrm{m}^{-3}\mathrm{T}^{-5}$, and $K = 80\,\mathrm{pW}\mu\mathrm{m}^{-2}\mathrm{T}^{-4}$, for $d = 50\,\mathrm{nm}$, the crossover temperature is $T \sim 0.8\,\mathrm{K}$.
Since we are working at T_{bath} situated in the intermediate regime where both couplings play a role, we have to understand both couplings and how parameters precisely affect the thermal behavior and define the different regimes.

5.2.4 Sample characteristics

In table 5.2 and 5.3, we summarize parameters and characteristics of samples studied, respectively in section 5.3 and 5.4.

Parameters	Copper 1	Silicon	Copper 2
t (µm)	0.05	0.015	0.05
w (µm)	0.3	\	0.3
l (µm)	70	\	7
$R_{N\,thermometer}$	8.8 kΩ	\	\
Heating	$R_{Cu1} = 135\,\Omega$	\	\

Table 5.2: *Preliminary sample parameters*

Parameters	Copper 1	Silicon	Copper 2
t (µm)	0.045	0.05	0.045
w (µm)	0.3	\	0.3
l (µm)	18	\	3
$R_{N\,thermometer}$	16 kΩ	200 MΩ	130 kΩ
Heating	$R_{N\,heater} = 16\,\mathrm{k}\Omega$	\	\
$\tau_\phi\Gamma$	6.10^{-4}	\	8.10^{-4}
C (fF)	\	3.85	\

Table 5.3: *Phonon thermometer sample parameters*

5.3 Preliminary phonon thermometer experiment

5.3.1 Preliminary sample

Figure 5.3.1 (left) shows our first sample's SEM images. N_1 is made of a 70 µm long, 300 nm wide and 50 nm thick copper wire of resistance R=135 Ω. The wire is in direct transparent contact with pads or reservoirs at each extremity. A S-I-N-I-S junction is placed close to the center of the metallic wire, and is used as an electron thermometer.

The copper wire N_1 is covered by a 15 nm thick silicon layer that decouples galvanically the two circuits and protects electron thermometer tunnel junctions during the second lithography process. The copper island N_2, of a 7 µm length, 300 nm width and 50 nm thickness, is colored in yellow on Fig. 5.3.1. It is placed with a perfect alignment, on top of the copper wire N_1. The top island N_2 also possesses a S-I-N-I-S junction so that we can measure the phonon temperature of the system. On Figure 5.3.1 (left), the blue outlined inset is a zoom on the electron thermometer. The red-outlined inset is a zoom on the phonon thermometer. We are not able to distinguish silicon on this image.
The electron thermometer S-I-N-I-S junction shows a 8800 Ω normal state resistance. For calibration , we have measured its current-voltage characteristics at equilibrium (no current bias in N_1) (figure 5.3.2). The data are nice isotherms, without out-of-equilibrium phenomena like self-cooling effects.

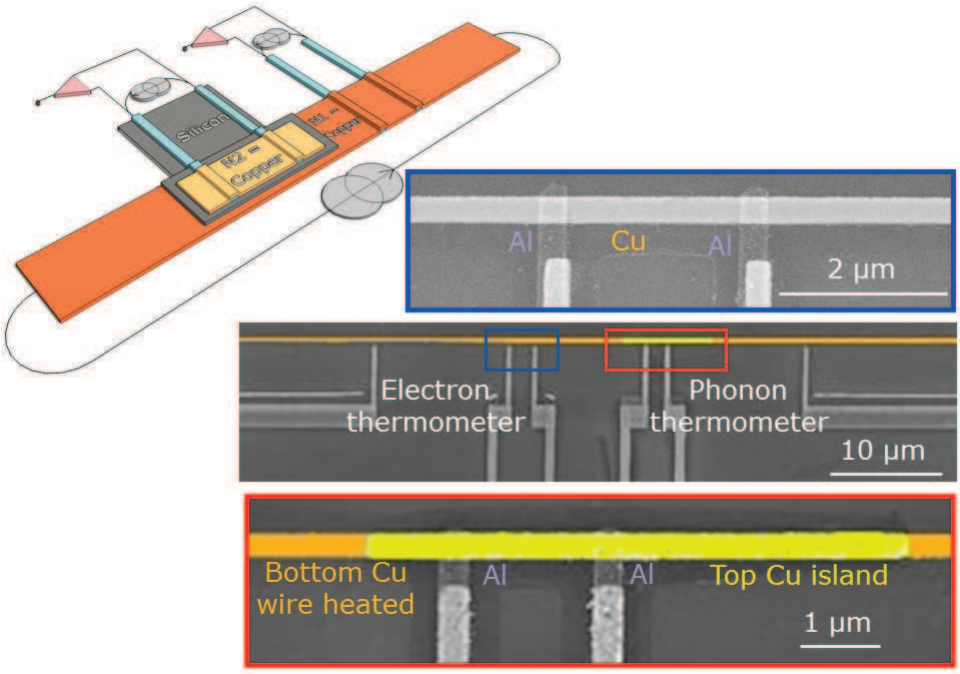

Figure 5.3.1: *Preliminary phonon thermometer: schematic and SEM image. The blue inset shows the electron thermometer made of a S-I-N-I-S junction, the red inset shows the phonon thermometer made of a S-I-N-I-S junction. In light gray is copper, gray is aluminum and dark gray is silicon oxide substrate*

5.3.2 Measurements

In this section, we present the measurements we have pursued on the preliminary sample. In the experiment, we bias the Cu wire and measure simultaneously the electron

thermometer current-voltage characteristics. The electronic temperature T_e is then extracted from the related differential conductance using Eq. 1.2.12. The injected power is calculated as the square of polarization $V_{wire} = V_{app} \frac{R_{Cu\,wire}}{R_{Cu\,wire}+R_{leads}}$ divided by the wire's resistance R_{Cu1}: $P_{inj} = {}^{V^2_{wire}}/_{R_{Cu\,wire}}$.

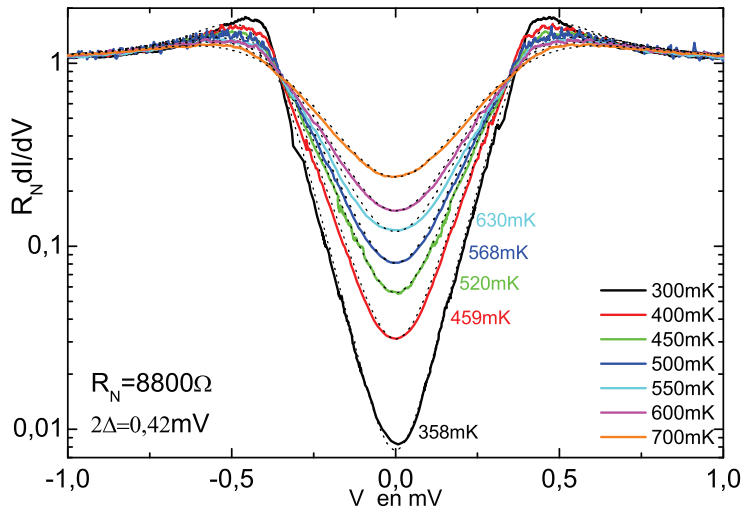

Figure 5.3.2: *Differential conductance of the electronic thermometer for different* T_{bath}= *300, 400, 450, 500, 550, 600, 700 mK from the bottom to the top.* T_0 = *358, 459, 520, 568, 630, 678, 774 mK extracted from theoretical isotherm fits (dotted line) with fixed parameters* $\Delta = 0.21\,mV$, $R_N = 8800\,\Omega$

Fig. 5.3.4 shows the electronic temperature T_e versus the injected power P_{inj} in the range from 0 to 5000 pW for different bath temperatures from 360 mK to 680 mK. We observe that the temperature increase is not linear with the injected power. As expected, the electronic temperature sets measured by starting from different bath temperatures tend to merge at high injected power.

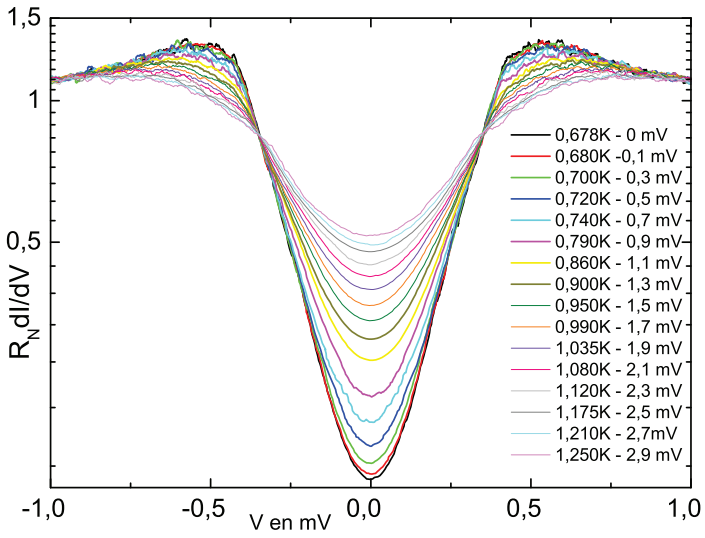

Figure 5.3.3: *Electron thermometer response under voltage bias of N_1 Cu wire from 0 to 2.9 mV from the bottom to the top at $T_{bath} = 0.6\,K$: differential conductances and T_e extracted from theoretical fits with fix parameters $\Delta = 0.21\,mV$, $R_N = 8800\,\Omega$, and $T_0 = 0.678\,K$.*

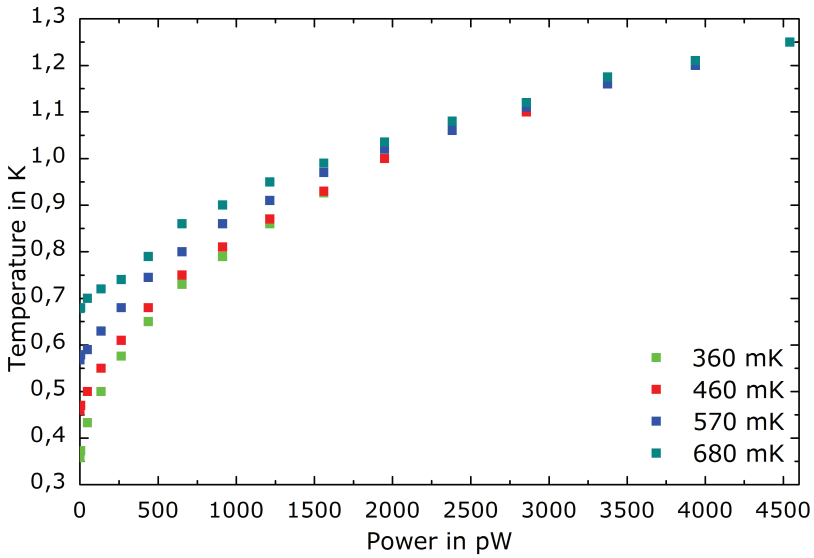

Figure 5.3.4: *Electron thermometer: electronic temperature T_e versus injected power P_{inj} for different bath temperatures (different colors)*

5.3.3 Data analysis

In this discussion, we will first consider that the whole metallic wire N_1 is at a uniform temperature. Although it may appear clear from the beginning that this it is an oversimplification, this hypothesis has the interest of simplicity.

Electron-phonon coupling bottleneck

Let us first assume that Normal metal phonons and substrate phonons are thermalized to the bath temperature $T_{ph} = T_{bath}$, which amounts to consider an infinite Kapitza coupling. The fitting parameter is Σ. Figure 5.3.5 shows the electronic temperature T_e calculated from Eq. 5.2.1 for different values of Σ from 1200 to 1800 $\mathrm{pW}\mu\mathrm{m}^{-3}\mathrm{K}^{-5}$.

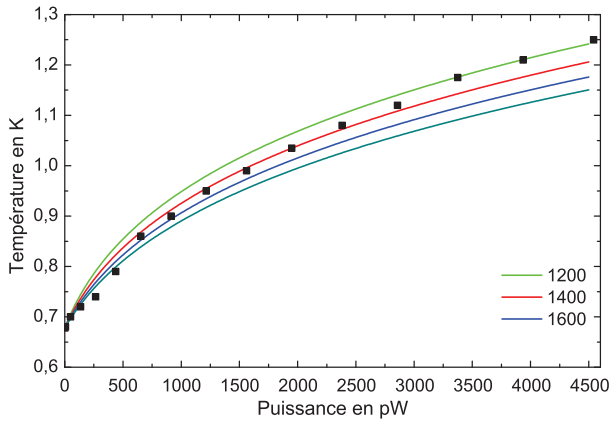

Figure 5.3.5: *Experimental data of $T_{bath} = 678$ mK (black square) and theoretical temperature evolution given by Eq. 5.2.1 for Σ =* 1200, 1400, 1600, 1800 $\mathrm{pW.K}^{-5}.\mu\mathrm{m}^{-3}$ *(from the top to the bottom).*

As can be seen from Fig. 5.3.5, no fixed value of Σ can describe all the experimental data. The most appropriate Σ for each bath temperature data is given in Table 5.4. In every case, the fit Σ is smaller than the usual 2000 $\mathrm{pW}.\mu\mathrm{m}^{-3}.\mathrm{K}^{-5}$ found in the literature for bulk Copper. Thus the assumption of Normal metal phonons fully thermalized to the bath temperature appears as incorrect. The electron-phonon coupling does not give a full picture of the thermal effects taking place in our sample.

T_{Bath} (mK)	358	459	568	678
Σ ($\mathrm{pW.K}^{-5}.\mu\mathrm{m}^{-3}$)	1600	1200	1290	1200

Table 5.4: *Estimated Σ for different bath temperatures.*

Kapitza resistance bottleneck

As a second approach, let us consider phonons and electrons to be at a same temperature $T_{ph} = T_e$, which means an infinite electron-phonon coupling. The fitting formula is then Eq. 5.2.2 with K as a fitting parameter. Figure 5.3.6 shows the electronic temperature calculated from Eq. 5.2.2 with different values of K from 70 to 120 $\mathrm{pW.\mu m^{-3}.K^{-5}}$ and data at $T_{bath} = 678\,\mathrm{mK}$.

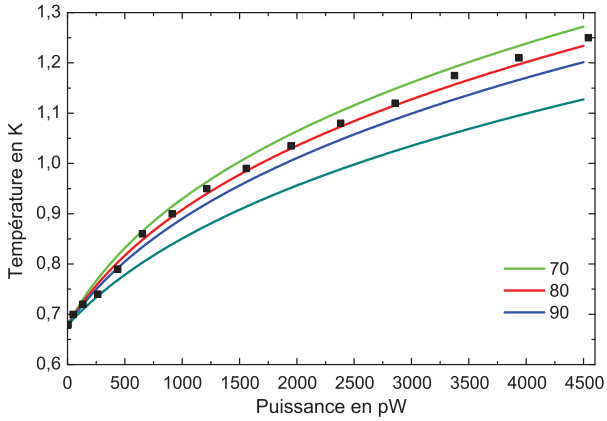

Figure 5.3.6: *Experimental data of T_{bath}= 678 mK (black square) and theoretical temperature evolution given by eq. 5.2.2 for K=* 70, 80, 90, 120 $\mathrm{pW.K^{-4}.\mu m^{-2}}$ *(from the top to the bottom).*

Again we obtain a different Kapitza resistance for every bath temperatures. The fit values summarized on Table 5.5 are of the same order of magnitude than the value of 80 $\mathrm{pW.\mu m^{-2}.K^{-4}}$ from Ref. [70].

T_{Bath} (mK)	358	459	568	678
K ($\mathrm{pW.K^{-4}.\mu m^{-2}}$)	89	83	77	77

Table 5.5: *Best fit K values for different bath temperatures.*

Full model

The two former analyses show that the electronic temperature increase can not be explained completely by either the electron-phonon coupling or the Kapitza coupling. If we consider now the entire model including electron-phonon coupling and the Kapitza resistance, this means that we replace the bath temperature T_{bath} in Eq. 5.2.1 by the

expression 5.2.2 of the phonon temperature, so that we obtain:

$$T_e = \sqrt[5]{P_{inj}/\Sigma V + \left(P_{inj}/KA + T_{bath}^4\right)^{5/4}} \tag{5.3.1}$$

Figure 5.3.7 (right) shows our experimental data for the electron thermometer response (black dots) at $T_{bath} = 586\,\mathrm{mK}$, together with the theoretical T_e values calculated from Eq. 5.3.1 (continuous blue line) and from Eq. 5.2.2 (continuous red line). Fig. 5.3.7 (left) shows the same data and predictions but in the cooling regime, from Ref. [70] at $T_{bath} = 568\,\mathrm{mK}$. In every case, the fit parameters used are $\Sigma = 2000\,\mathrm{pW.K^{-5}.\mu m^{-3}}$, $K = 40\,\mathrm{pW.K^{-4}.\mu m^{-2}}$. The predicted temperatures from the complete model are much higher than our experimental values. Moreover, the fit between experimental data and theory can not be improved by a reasonable modification of fit parameters Σ and K.

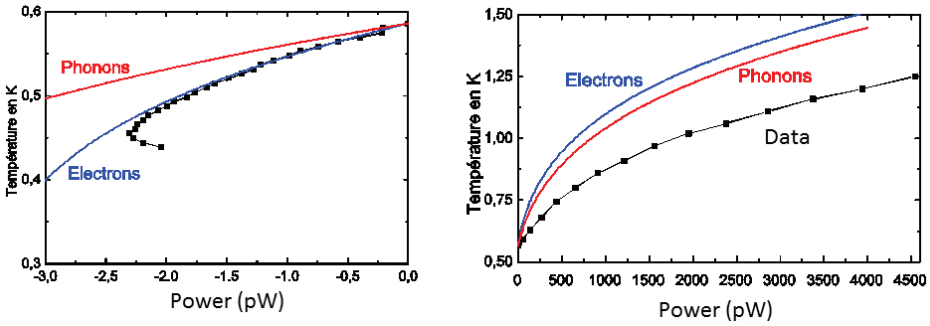

Figure 5.3.7: *(a) Experimental data from Ref. [70] in the cooling regime (black linked squares) at T_{bath}= 568 mK and (b) Experimental data in the heating regime (black linked squares) at T_{bath}= 586 mK, theoretical T_e given by Eq. 5.3.1 and theoretical T_{ph} given Eq. 5.2.2 with fit parameters* $\Sigma = 2000\,\mathrm{pW.K^{-5}.\mu m^{-3}}$, $K = 40\,\mathrm{pW.K^{-4}.\mu m^{-2}}$.

Temperature gradient

Let us step back. We have made a strong assumption by considering that the wire length of 70 µm was long enough to establish a uniform temperature close to the middle of the wire determined by a local equilibrium between the injected power and the relevant thermal couplings to the bath. Pads are thermalized at the bath temperature thanks to their large size and most of the power is dissipated there. Consequently, there is a temperature gradient along the wire. A typical profile is drawn Figure 5.3.8. In general, the local temperature is lower than the prediction of our model [29, 86, 35]. We then need to consider the heat equation diffusion:

$$\frac{d}{dx}\left(\frac{L_0 T(x)}{R}\frac{dT}{dx}\right) = -\rho i^2 + \Sigma V\left(T^n(x) - T_0^n(x)\right) \tag{5.3.2}$$

where L_0 is the Lorentz number, ρ is the resistivity, n is an exponent, which is in our case $n = 5$. Here, we make for simplification of the discussion the assumption that the Kapitza resistance can be neglected.

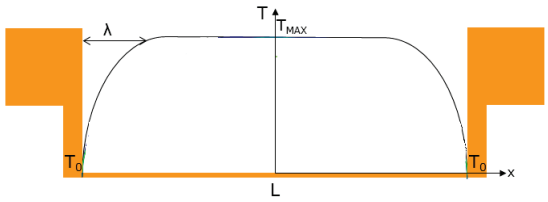

Figure 5.3.8: *Schematic of temperature gradient along the copper wire for a wire of length* λ

The length necessary to reach the maximum temperature, called the healing length λ, can be evaluated to be $\lambda = \sqrt{\frac{L_0}{\rho\Sigma T^3}}$. At T_{bath}= 500 mK, the healing length λ is 70 µm. It decreases as the bath temperature increases. We have applied our model to data including this gradient of temperature. As shown in Figure 5.3.9, we can fit our data of different bath temperatures with $T_e = \sqrt[5]{P_{inj}/\Sigma V + T_{bath}^5}$, where the fitting parameter $\Sigma = 2000\,\mathrm{pW}.\mu\mathrm{m}^{-3}.\mathrm{T}^{-5}$ is similar to the literature value. This could suggest that the thermal relaxation of electrons is limited by the electron-phonon coupling. Notwithstanding the agreement between experimental data and the corrected theoretical T_e, the numerous fit parameters involved here makes the fit not very persuasive and the above conclusion uncertain. Finally, the phonon thermometer was measured but its differential conductance had no coherence peaks, so that the analysis has not been pursued.

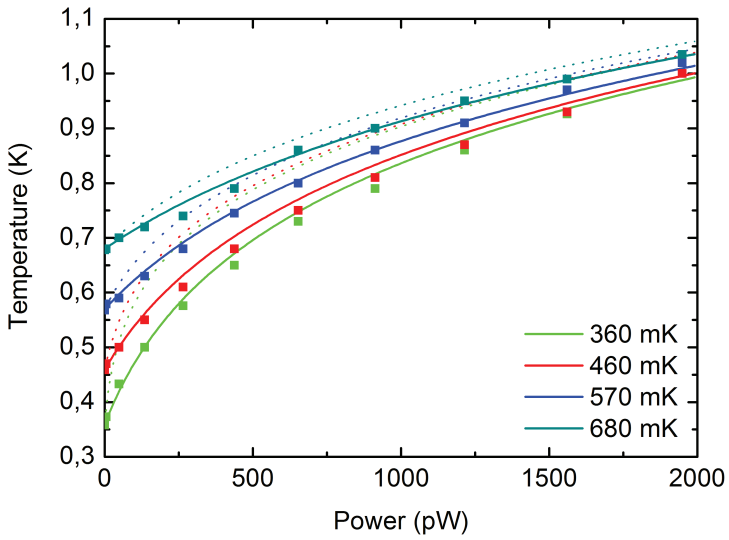

Figure 5.3.9: Data fitting including the thermal gradient effect. Continuous line is $T_e = \sqrt[5]{P_{inj}/\Sigma V + T_{bath}^5}$, dashed line is $T_{ph} = \sqrt[4]{P_{inj}/KA + T_{bath}^4}$ with $\Sigma = 2000\,\mathrm{pW}.\mu\mathrm{m}^{-3}.\mathrm{T}^{-5}$ and $K = 44\,\mathrm{pW}.\mu\mathrm{m}^{-2}.\mathrm{T}^{-4}$

We conclude that a long wire was not the best option to study the phonon contribution in a mesoscopic system, since we have to take into account the heat diffusion along the wire. An optimized design should present a well-defined thermal boundaries at the normal metal N_1 extremities. In this respect, this study helped us to optimize the sample design for the following experiment.

5.4 Phonon thermometer new generation

We have elaborated a new sample design, where the bottom copper wire is heated by highly resistive tunnel junctions that give a homogenous temperature along the wire. Figures 5.4.1 and 5.4.2 show respectively a schematic and a SEM image of the sample. The length of the bottom copper wire was decreased to 18 µm, and its thickness slightly decreased to 45 nm for need of the fabrication process, the width remaining the same. Each of its extremities ends with a tunnel junction. The silicon layer deposited was thicker with 45 nm. In this case, we measured the resistance of the silicon layer between the two stages to be 200 MΩ at low temperature. Finally, we have reduced the top copper island size to a 3 µm length. All tunnel junctions parameters are summarized in table 5.6 and 5.3.

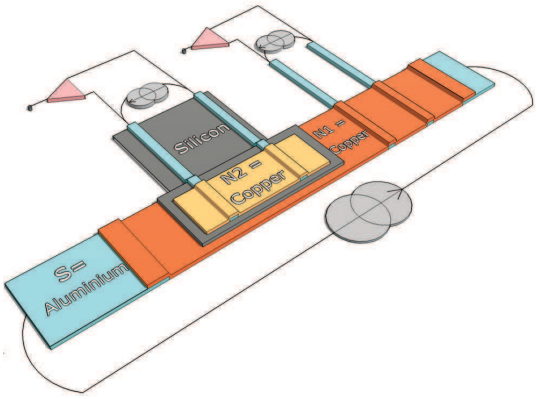

Figure 5.4.1: *Schematic of phonon thermometer sample. There is a tunnel barrier of aluminum oxide between the copper wires (orange) and the aluminum leads (blue). Silicon covers the entire bottom circuit.*

Figure 5.4.2: *SEM image of phonon thermometer.*

Junctions	Area (µm²)	R_N ($k\Omega$)	Δ(meV)	T_C (K)
Heating	0.3×0.3	16	0.21	1.47
Electron thermometer	0.3×0.3	16	0.21	1.47
Phonon thermometer	0.3×0.3	130	0.23	1.47

Table 5.6: *Tunnel junctions characteristics of the phonon thermometer sample*

First, we characterized all the sample's tunnel junctions, in order to verify their properties as a temperature probe and/or a power injector. In the experiment, we bias the heater junctions at a voltage higher than the gap, see Fig. 5.4.3, in order to be in the Joule heating regime. The power injected is calculated from the I-V characteristics of the junction and the equation 1.2.19.

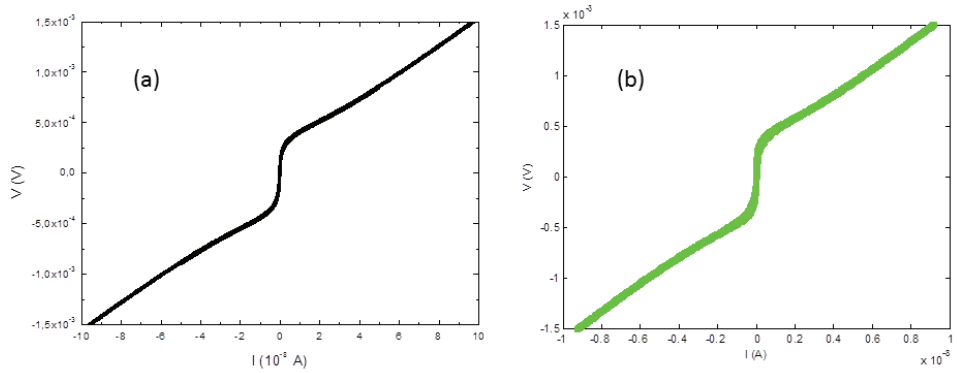

FIGURE 5.4.3: *IV characteristic of heater (a) and thermometer (b) for different bath temperature, and polarisation i.e power injected at bath temperature of 400 mK .*

Similarly to the preliminary experiment, we have measured the electron and phonon thermometer response independently for different values of the bath temperature and injected power. Electron and phonon temperatures versus injected power are plotted in log-log-scale on Figure 5.4.4. We observe that the temperature evolution features a linear behavior of slope coefficient n between 1/6 and 1/4. Thus the electronic temperature and the Joule power appears to be related through a power law.
Let us now compare the data with the different limits of our model. Similarly to the preliminary experiment, we first consider the extreme limits, i.e. the electron-phonon relaxation limited and the strong Kapitza resistance limited, for the different thermometers. We first focus on the electron thermometer behaviour.

5.4.1 Electron thermometer

Electron-phonon coupling bottleneck

The temperature recorded by the electron thermometer at different bath temperatures is first compared to the theoretical temperature prediction obtained for electron-phonon coupling limited relaxation. Figure 5.4.4 shows the plots of theoretical electronic temperature obtained from Eq. 5.2.1, taking into account the geometry of the sample $V = t_{Cu1} w_{Cu1} l_{Cu1}$, for different values of $\Sigma = 1000, 2000, 3000\,\mathrm{pW.K^{-5}.\mu m^{-3}}$.

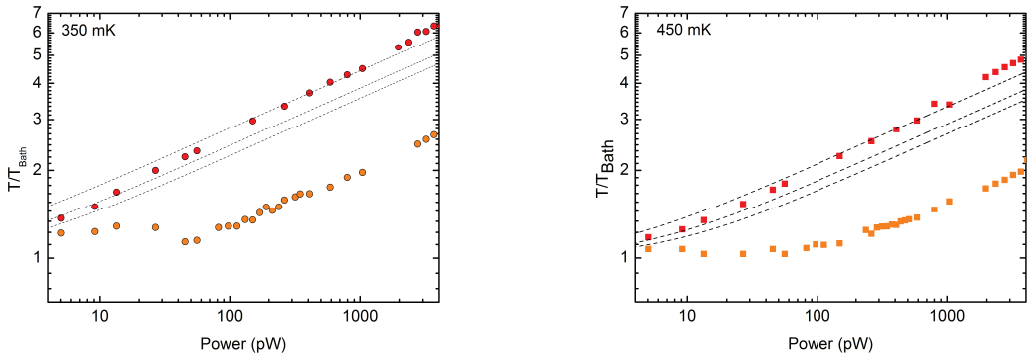

Figure 5.4.4: *Experimental data of electron thermometer (red symbols) and phonon thermometer (orange symbols) at* $T_{bath} = 350$ *mK and 450 mK and theoretical temperature profile given by eq. 5.2.1 for* $\Sigma = 1000, 2000, 3000\,\mathrm{pW.K^{-5}.\mu m^{-3}}$ *(dashed line from the top to the bottom), .*

We observe that there is no value of Σ that can describe the thermal behaviour of electron thermometer over the entire power range. It means that the electron-phonon coupling is not the unique limiting factor for thermal relaxation of the electrons in the copper wire.

Kapitza resistance bottleneck

Thus we consider the other limit, where the electron-phonon coupling is strong ($\Sigma \to \infty$), so that the Normal metal electrons and phonons are at thermal equilibrium. The temperature is then limited by the Kapitza resistance. Fig. 5.4.5 shows the experimental data and the theoretical prediction given by Eq. 5.2.2.
The K value that fits best the experimental data for the different bath temperature is $K = 20\,\mathrm{pW.K^{-4}.\mu m^{-2}}$, which is very low. Furthermore, this limit of strong electron-phonon coupling is not the regime we expect.

Complete thermal model

Let us now consider the full picture described by our thermal model, where the phonons are at a intermediate temperature T_{ph} between T_{bath} and T_e. Fig. 5.4.6 shows both our experimental data and the calculated temperatures from the complete thermal model (Fig. 5.2.1). We obtain a good fit for the parameter values $\Sigma = 2000\,\mathrm{pW.K^{-5}.\mu m^{-3}}$ and $K = 80\,\mathrm{pW.K^{-4}.\mu m^{-2}}$ for both bath temperature considered. This experiment suggests that phonons are neither at bath temperature nor at the electron temperature, but at an intermediate temperature between the two. Moreover, it stresses the fact that the

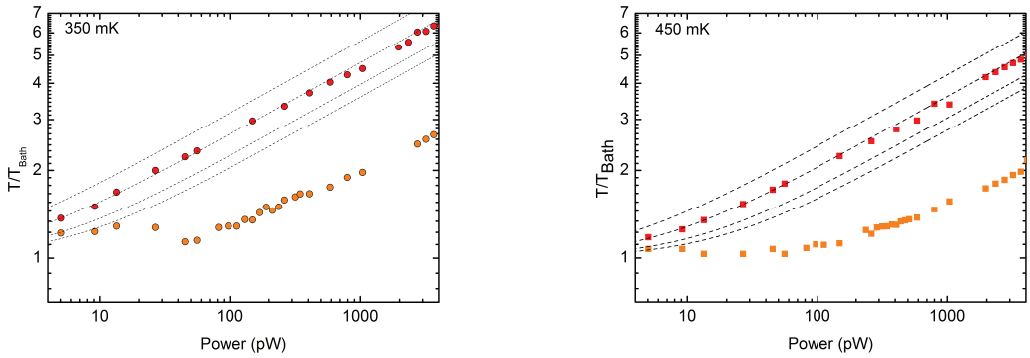

FIGURE 5.4.5: *Experimental data of electron thermometer (red symbols)$T_e(P_{inj})$ and phonon thermometer (orange symbols) at T_{bath}= 350 mK and 450 mK and theoretical temperature evolution given by Eq. 5.2.1 for K= 10, 20, 40, 60 pW.K^{-4}.μm^{-2} (black dashed lines from the top to the bottom).*

Kapitza resistance plays a significant role and can not be neglected in the determination of the electronic temperature.

5.4.2 Phonon thermometer data analysis

Let us now focus on the phonon thermometer data plotted in orange (Fig. 5.4.6). We observe that the phonon temperature T_{ph} increase with injected power is less strong than T_e. The linear behavior in log-log-scale above 100 pW indicates that it follows a power law. As we assume that the top copper island is thermally coupled only to the bottom copper wire, and this through phonons, we consider that the electron temperature of N_2 gives a measure of the phonon temperature in N_1. coupling.
The phonon temperature (orange dots) can thus be fitted with Eq. 5.4.1 from our thermal model:

$$T_{ph} = \sqrt[4]{P_{inj}/K'A + T_{bath}^4} \tag{5.4.1}$$

where $A = l_{Cu1}.w_{Cu1}$ is the surface between the bottom copper wire and the silicon substrate. The Kapitza coefficient is used as a fit parameter and the fitted value is $K' = 700\,\text{pW}.\mu\text{m}^{-2}.\text{T}^{-4}$. As can be seen on Fig. 5.4.6, the prediction fits perfectly the data of the phonon thermometer. The power law is what we expected for phonon temperature, however the fit parameters indicates a Kapitza parameter ten times higher than for the electron thermometer.

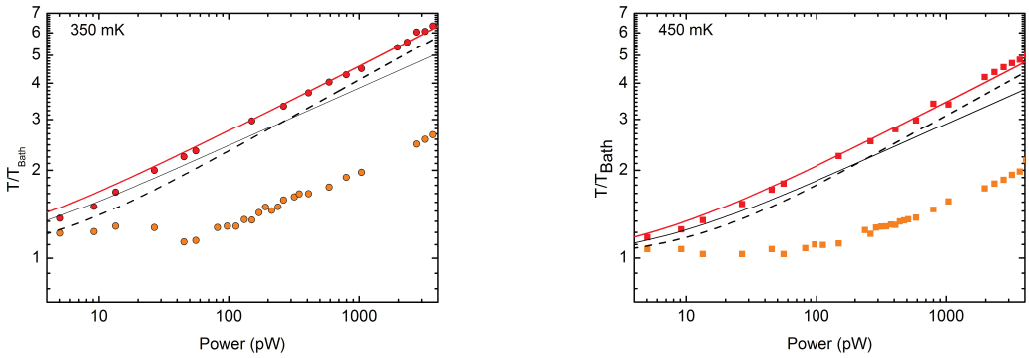

FIGURE 5.4.6: *Experimental data of Electron thermometer (red symbol) at $T_{bath} = 350$ mK (black square), 450 mK (black square) and theoretical temperature profile given by the complete thermal model Eq. 5.3.1 (continuous red line), the theoretical phonon temperature from Eq 5.2.2 (dashed black line), and theoretical electron temperature in the strong Kapitza coupling Eq 5.2.1 (dotted black line) for $K = 80\,\mathrm{pW.K^{-4}.\mu m^{-2}}$ and $\Sigma = 2000\,\mathrm{pW.K^{-5}.\mu m^{-3}}$.*

5.4.3 Discussion

The model fits perfectly the electron temperature data with fitting parameters $\Sigma = 2000\,\mathrm{pW.\mu m^{-3}.T^{-5}}$ and $K = 80\,\mathrm{pW.\mu m^{-2}.T^{-4}}$. Both values are in agreement with previous works. It suggests that our model is valid.
The phonon temperature evolution agrees with a $P^{1/4}$ law given by the Kapitza coupling, which is in agreement with our model. Nevertheless the Kapitza constant derived from this fit is significantly larger than the Kapitza resistance derived from the electron thermometer data.
Let us discuss different possible explanations. In the top island, we measure an electronic temperature assumed to be in equilibrium with N-metal phonons. The assumption of a diffusive phonon bath in the entire sample might not be correct. However, the more realistic reason is that the top copper island is more coupled to the substrate than assumed. To isolate galvanically the two stages, we have deposited 45 nm of silicon on the entire wafer. It can explain that the metallic island is not totally decoupled thermally from the silicon substrate. Its apparent value K' is thus higher than expected.
In order to cross-check our conclusions, we have heated the top circuit and measured the electron thermometer at the bottom. Does it follow a $P^{1/5}$ or $P^{1/4}$ law?

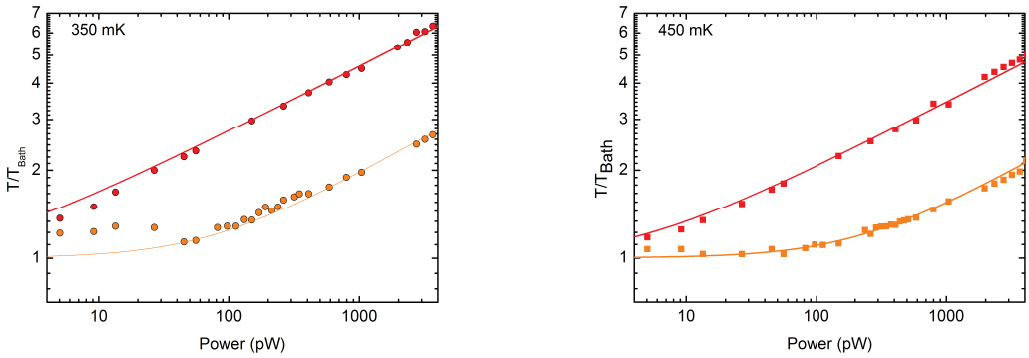

FIGURE 5.4.7: *Experimental data of Electron thermometer (red symbols) at T_{bath} = 350 mK (left), 450 mK (right) fitted with the theoretical temperature evolution (red line) given by Eq. 5.3.1 for* $K = 80\,\mathrm{pW.K^{-4}.\mu m^{-2}}$ *and* $\Sigma = 2000\,\mathrm{pW.K^{-5}.\mu m^{-3}}$ *and phonon thermometer data (orange symbols) fitted by Eq. 5.2.2 (orange line) with K'=* 700, $\mathrm{pW.K^{-4}.\mu m^{-2}}$.

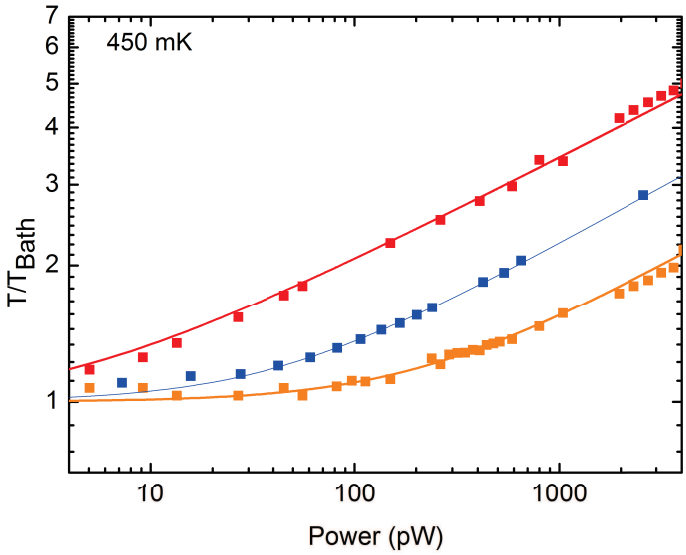

Figure 5.4.8: *Expreiment done at T_{bath}=450 mK. Experimental data: electron thermometer T_e (red symbols), electron thermometer T_{ph} (orange symbols), inverted experiment T_i (blue symbols). Theoretical fit: complete thermal model (red line), strong electron-phonon coupling (orange line), strong electron-phonon coupling (blue line)*

In parallel to previously discussed data, Fig. 5.4.8 shows the measured electron thermometer temperature when we heat from phonon thermometer. From our model, this data can be fitted with

$$T_{ph} = \sqrt[4]{P_{inj}/K''A'' + T_{bath}^4}$$

with $K"A" = 1215\,\mathrm{pW.K^{-4}}$ where $A" = l_{Cu2}.w_{Cu2}$. The fitted coupling constant is not identical to the one derived from the phonon thermometer evolution. Thus an asymmetry is revealed between the two stages. This latter experiment is an other hint that we might have an extra coupling between the top copper island and the substrate. It would also mean that the temperature measurement on the top copper island does not give exactly the phonon temperature. A more detailed model needs to be devised, which would take into account the direct coupling of the insulating silicon layer to the substrate at the bath temperature.

5.5 Conclusion & Perspectives

In this chapter, we have studied the thermal behavior of electrons in a metallic mesoscopic wire. A preliminary experiment has outlined the importance of conditions at limits. Then we designed and measured a device allowing two inndependent temperature measurements. Our experimental results validate our thermal model for bath temperature close to 400 mK and over a wide range of heating power. However, the experiment also shows that the top island, which is assumed to be at the phonon temperature, might be more coupled to the substrate than expected. More precisely, we obtain a correct power law for the power-temperature law relation, but the fitted prefactor differs from predictions.
Eventually, we have designed and fabricated another sample presented on Figure 5.5.1 in order to study asymmetry revealed by the previous experiment and to quantify losses to the substrate. This sample presents this possibility with two sets of S-I-N-I-S junctions on the two normal metals. This would enable us to heat and probe temperature of both stages. Moreover, tunnel junctions to the main metallic wire are made larger in order to be able to investigate also the cooling regime.

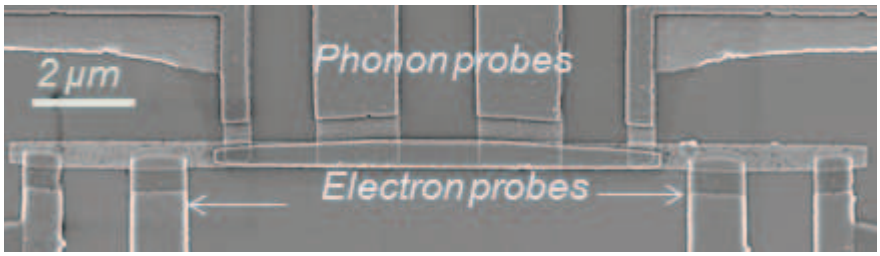

Figure 5.5.1: *SEM image of the ultimate phonon thermometer dedicated to quantify contribution of substrate and study the electronic cooling regime*

Chapter 6

Quasi-particle relaxation under magnetic field

6.1 Introduction

While a high magnetic field weakens electronic refrigeration by reducing the superconductive gap [3], a small magnetic field appears to improve electronic refrigeration in a S-I-N-I-S junction by enhancing relaxation processes in the superconducting electrodes (Ref. [62]). Indeed, under small magnetic field vortices are created. They reduce locally the gap and thus trap in their core quasi-particles (qp), which then relax more easily.
In this chapter we will discuss the influence of quasi-particle trap geometry. We will first discuss the process of relaxation of hot quasi-particles in the superconductor. Afterwards, the experiment performed in our lab on trap geometry and magnetic field influence will be presented

6.2 Quasi-particles relaxation and quasi-particle trap

One factor curbing S-I-N-I-S electronic refrigeration is the relaxation of the quasi-particles that are injected into the S electrode. As the superconductor locally overheats, it decreases the cooling power at a NIS junction because of enhanced qp back-tunneling. The excess qp density close to the junction can be reduced by increasing the thickness of superconducting electrodes [14], or by covering them partially with a layer of normal metal that acts as a qp trap [56]. The qp population behaviour is typically modeled in terms of a diffusion equation, describing their recombination retarded by phonon re-trapping, and other loss mechanisms. Converting the excess density into an effective, position-dependent temperature, it appears that at phonon temperatures $k_B T \ll \Delta$, the superconducting leads can be overheated on a length scale ranging from tens of micrometers to a millimeter. This is possible because in superconducting state the

electron-phonon relaxation and electronic heat conduction are exponentially suppressed compared to their normal-state values.

6.3 Experiment

6.3.1 Samples

In this chapter we study samples provided by PICO group from Alto University. Figure 6.3.1 shows a sample (Ref. [62]) similar to the ones studied in this chapter. All samples are S-I-N-I-S cooler junctions from the same chip, obtained by traditional two-angle shadow evaporation, described in Chapter 3. The Normal metal is a 22 nm thick Copper island, colored in red in the picture 6.3.1. The superconductor is a 30 nm Aluminum deposit, in blue in Fig. 6.3.1. The Al electrodes are characterized by a zero-temperature energy gap $\Delta \sim 210\,\mu eV$ and a critical temperature $T_c = 1.4\,\mathrm{K}$. The electronic thermometer is placed at the center of the Normal metal island, while cooler junctions are situated at each extremities of the Normal metal island. The geometry of the superconducting electrodes close to the cooler is defined by three parameters : a, b, and c. Sample's parameters are shown in Table 6.1. The normal states tunnel resistances of these junctions are of the order of $R_N \sim k\Omega$

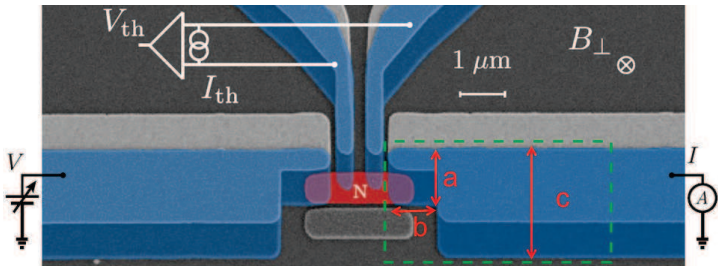

Figure 6.3.1: *SEM picture of cooler studied*

sample	t_S (µm)	t_N (µm)	w_N (µm)	l_N (µm)	a (µm)	b (µm)	c (µm)
a25b10c10	0.03	0.022	0.5	1	2.5	10	10
a5b5c10	0.03	0.022	0.5	1	5	5	10
a5b10c5	0.03	0.022	0.5	1	5	10	5
a10b10c10	0.03	0.022	0.5	1	10	10	10

Table 6.1: *Geometric parameters of the different samples studied*

6.3.2 Measurements

In Fig. 6.3.1 is schematized the electrical set-up. Measurements are performed in a dilution refrigerator featured with a three-axes coil. First we study the sample behaviour under a magnetic field $B_\perp$ perpendicular to the surface of our sample. Similarly to the description of Chapter 4, the thermometer is polarized at a fixed current I_{th}. We sweep I_{cooler} and measure voltages V_{cooler} and V_{th}, the latter being calibrated against T_{bath} at $I_{cooler} = 0$. For each sample, we have studied electronic refrigeration effect for different perpendicular field value $B_\perp$ and different bath temperatures T_{bath}.

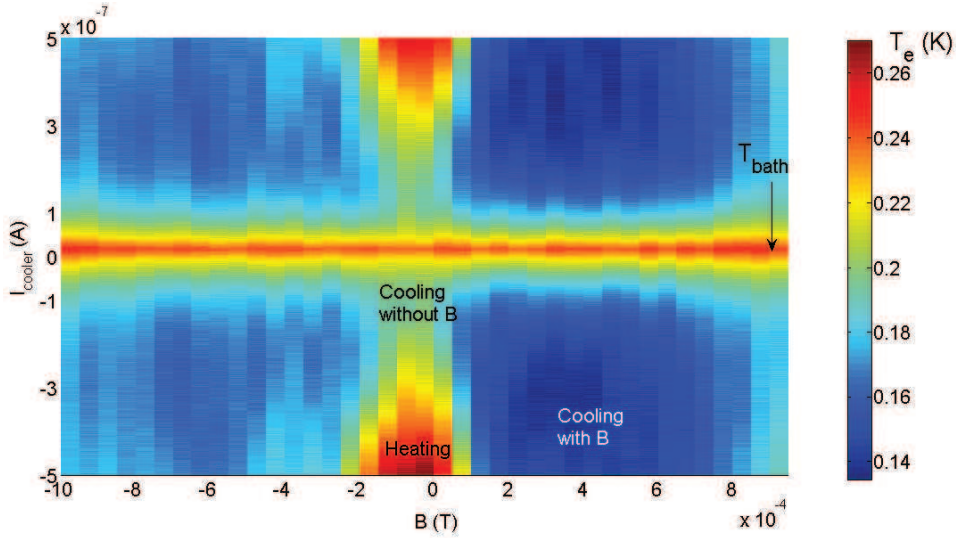

Figure 6.3.2: *Sample a25b10c5 @ T_{bath}=250 mK : map of T_e versus I_{cooler} and $B_\perp$. Color code blue to red as T_e.*

Thus we obtain a mapping of the electronic temperature T_e versus I_{cooler} on a y-axis and perpendicular $B_\perp$ on a x-axis, as shown in Figure 6.3.2. This map gives already much information. The color code goes from blue to red as T_e increases. The red line at $I_{cooler} \sim 0$ A is at equilibrium temperature equals to T_{bath}. We see that the electronic temperature at equilibrium probed by the electronic thermometer is not disturbed by the perpendicular magnetic field. We also observe that electronic cooling is symmetric in regard to current polarization. Considering the remanent field of 1G that shift the effect of the origin of x-axis, the effect looks also symmetric in field $B_\perp$.
The map color scale demonstrates the perpendicular magnetic field effects on electronic refrigeration. We will discuss quantitatively this effect in the next section. In this experiment, we have also access to the S-I-N-I-S cooler IV characteristic just below the gap value. In agreement with results from Ref. [62], we observe that the gap increases slightly under small magnetic field between 1-2 Gauss, see in Figure 6.3.3. Measurements show minimum electronic temperature decreases noticeable under magnetic field compared to zero field conditions, with an enhancement of $\sim 12\%$ of the gap. These observations agree

with conclusions of Ref. [62] on enhancement of electronic refrigeration under magnetic field.

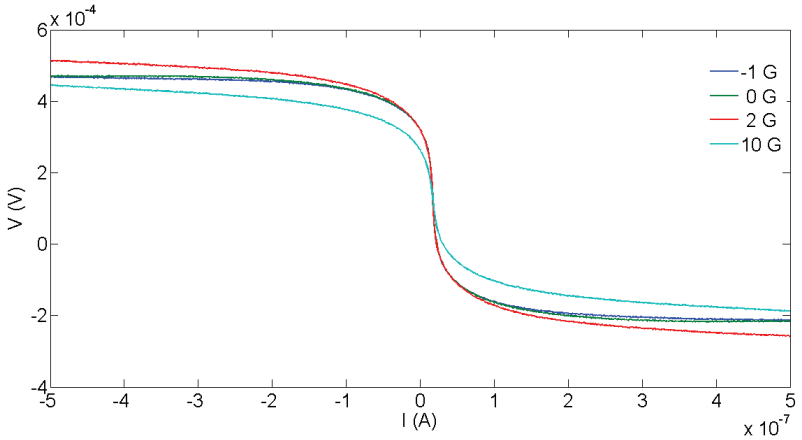

Figure 6.3.3: *Sample a25b10c5 at T_{bath}=250 mK : V_{cooler} versus I_{cooler} for $B_\perp$*= -1, 0, 2, 10 G

6.4 Magnetic effect on electronic refrigeration

6.4.1 Electronic refrigeration improvement

In this section, we focus on a quantitative analysis of electronic refrigeration improvements under a perpendicular magnetic $B_\perp$concentrate on Sample a5b5c10.
Figure 6.4.1 is the plot of $\triangle T_{e\,min} = T_{e\,min} - T_0$ versus the perpendicular magnetic field $B_\perp$. First we notice a diminution of the electronic temperature at negative and positive field. Then it increases slowly above 3 G. The electronic temperature drop $\triangle T_{e\,min}$ in sample a5b5c10 then shows a maximum electronic cooling for $B_\perp$ between 1 and 3 Gauss. Nevertheless, the cooling performance still depends on T_{bath}. As we can observe, the most important electronic cooling is obtained for 280 mK with a drop of 80 mK without magnetic field by biasing the cooler only. The magnetic field improves the cooling such that the electronic temperature drop reaches 140 mK.
We will now concentrate on the optimum bath temperature, i.e close to 300 mK, in order to study the influence of qp-trap geometry on electronic refrigeration.

6.4.2 Quasi-particle trap geometry

We are interested in the behaviour of different qp-trap geometry under a perpendicular magnetic field, in terms of electronic refrigeration.
In Figure 6.4.2 is plotted the electronic temperature drop $\triangle T_{e\,min}$ versus $B_\perp$ at T_{bath}=300 mK for samples a5b5c10, a10b10c10, a25b10c5 and a5b10c5. The graph shows a drop

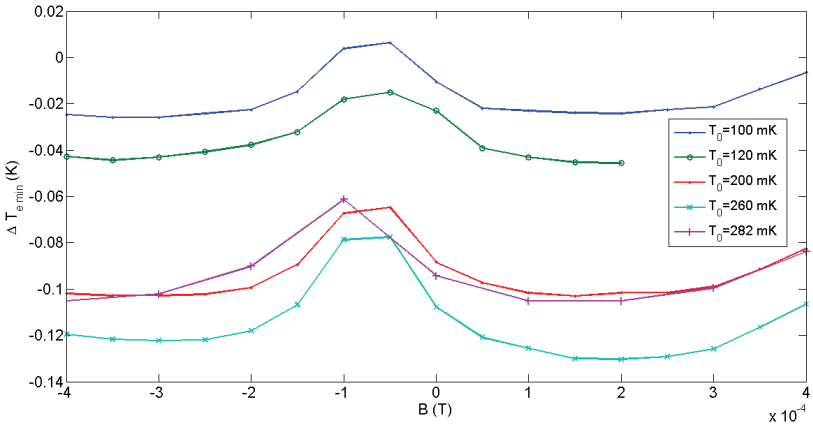

Figure 6.4.1: *Sample a5b5c10: Evolution of ΔT_e versus $B_\perp$ for different T_{bath} =100, 120, 200, 260, 280 mK*

of temperature with a different amplitude, depending on the sample. After a small stabilization it increases again.
The magnetic field B_0 below which all vortices are expelled from a narrow wire of width ω is given by $B_0 = \phi_0/\omega^2$, where the quantum flux $\phi_0 = h/2e$ [85]. Concerning samples studied here, their width vary between 2.5 and 10 µm, corresponding respectively to $B_0 \simeq$ 3.3 G and 0.2 G. It corroborates the idea of a qp-particles relaxation enhanced due to vortices creation. Differences in behaviour between a25b10c5 and a10b10c10 can be related to differences in their pad geometry. The decrease slope of $\triangle T_{e\,min}$ in a25b10c5 is smoother than in a10b10c10. Its $\triangle T_{e\,min}$ minimum is reached at larger $B_\perp$ and it increases later as well. A contrario, in a10b10c10, $\triangle T_{e\,min}$ decreases sharply the minimum is reached faster. These results supports Peltonen et al. thesis.

6.5 Conclusion

In this chapter we have improved our understanding of qp-trap efficiency. Since the perpendicular magnetic field induces vortices in the superconductors, creating normal regions that trap quasi-particles, we have changed the section of superconducting leads with different parameters a, b, and c, in order to control the relaxation of quasi-particle, close to the tunnel junction. In this first analysis, the width a close to the tunnel junction appears as the important important parameter the qp-relaxation respect to the $B_\perp$.
It is worthwhile to study the effect of the magnetic field orientation on electronic refrigeration. This study has been made, but could not be presented here since the analysis is still under way.

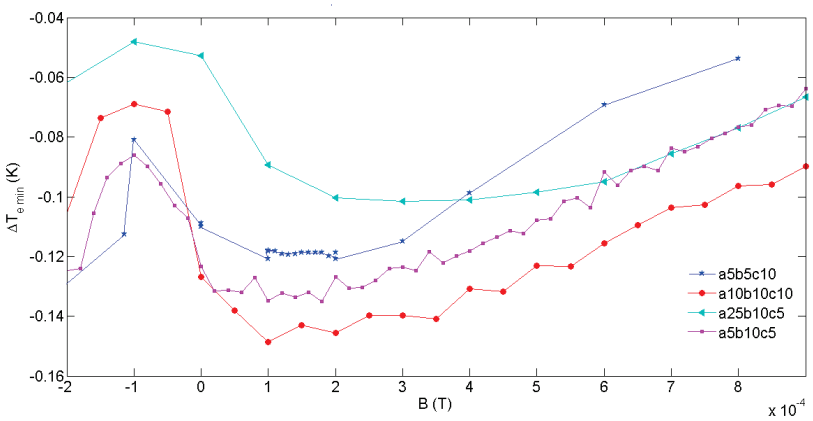

Figure 6.4.2: *Electronic refrigeration $\triangle T_{e\,min}$ under $B_\perp$ at T_{bath}= 300 mK: comparison of different qp-trap geometry: a5b5c10, a10b10c10, a25b10c5 and a5b10c5*

Conclusion & perspectives

Objectives summarize

The electronic refrigeration performance in hybrid superconducting tunnel junctions is curbed by fundamental and technological issues. Among the different limitations of electronic refrigeration, we have been interested in thermal couplings of normal metal electrons and in quasi-particle relaxation in the superconductor. Our aim was to improve the electronic refrigeration or at least to understand better its limitation. Despite the fact that we study these effects on the electronic temperature in S-I-N-I-S junctions, they are not specific to micro-refrigerators. Thermal couplings of the electronic bath to its environment and the qp-relaxation process are also pregnant in the context of quantum nano-electronics, including ultimate detector and quantum computing devices. Thanks to their quantitative sensitivity to the electronic temperature and to the superconductive gap, S-I-N-I-S micro-coolers are a perfect system to investigate these issues. In this thesis we have investigated the electron-phonon and Kapitza couplings, with a focus on on the phonon temperature of our mesoscopic metal. We have also discussed the photonic heat channel and its quantitative analysis for a series of practicals circuits [55]. Finally, we have also investigated quasi-particle relaxation effect in the superconducting leads of a micro-cooler.

Results of this thesis

We designed, fabricated and studied a device, called «phonon thermometer» that gives us access to electron and phonon temperature directly and independently. This experiment confirmed the power relation in exponent 5 in electron-phonon coupling, like in a bulk copper. It means that the phonon temperature is between the electron and the bath temperature. In practice, the approximation of a phonon temperature thermalized to the bath temperature is not valid at above a bath temperature of 300 mK and and a Joule power larger than 100 pW. The experiment revealed a thermal coupling of the phonon thermometer to the substrate more important than expected and an asymmetrical behaviour of our coupling. Consequently we designed and fabricated a new sample in order to quantify the coupling to the substrate. A deeper analysis of the present data set is also under way.
We have also developed a process to fabricate micro-coolers with large junction area and

a suspended normal metal in order to eliminate the direct coupling of the normal metal to the substrate. This process gives nice cooling characteristics and is really promising because of its ease of fabrication and its consistency in terms of superconducting cooling junctions [51].
Finally, we investigated the quasi-particle relaxation under a magnetic field, and see a significative enhancement of electronic cooling. Compared to previous results, our study gives us a better understanding of the optimum quasi-particle trap geometry to improve the electronic refrigeration.

Limits & perspectives

As the dimension of our system decrease, the electron-phonon coupling power law is expected to decrease. This is also very promising for electronic refrigeration since the electron-phonon coupling weakens at low dimension [28]. Consequently, a large electron and phonon cooling has been predicted in metallic beams. Experimentally, electronic refrigeration has been demonstrated in a two-dimensionnal electron gas and in a bulk doped semi-conductor [66].
In our cooling power calculations, we consider a continuous 3D density of states for the normal metal, it would be interesting to characterize the cooling regime in the limit of a really nanoscale normal metal island.
The electronic refrigeration with larger junction emphasizes non-equilibrium effects [11]. IV characteristics need to be analyzed taking into account the superconducting energy gap variation due to local heating of the electrode. This effect is quite relevant in respect of the cascade cooler geometry S'-S-I-N-I-S-S', where the outer junctions in the device cool the superconductor used in the central junctions, allowing a large temperature difference between the central normal metal that is cooled. Further theoretical analysis needs to be done before a practical realization can be successfully envisaged.

Annexes

Annexe A

Floatting Current Sources

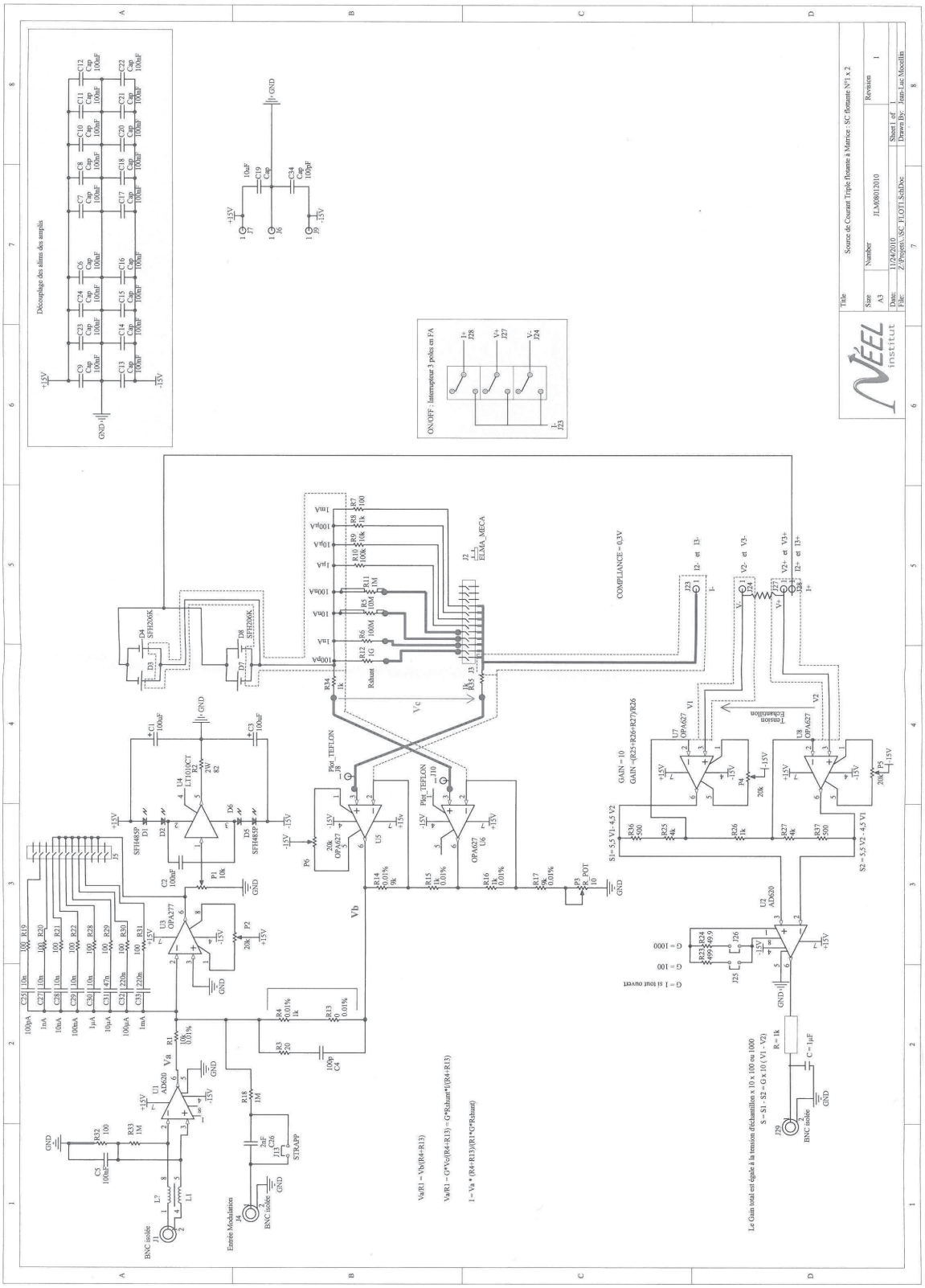

FIGURE A.1: Floatting current source electrical circuit

Annexe B

Remotable Current Sources

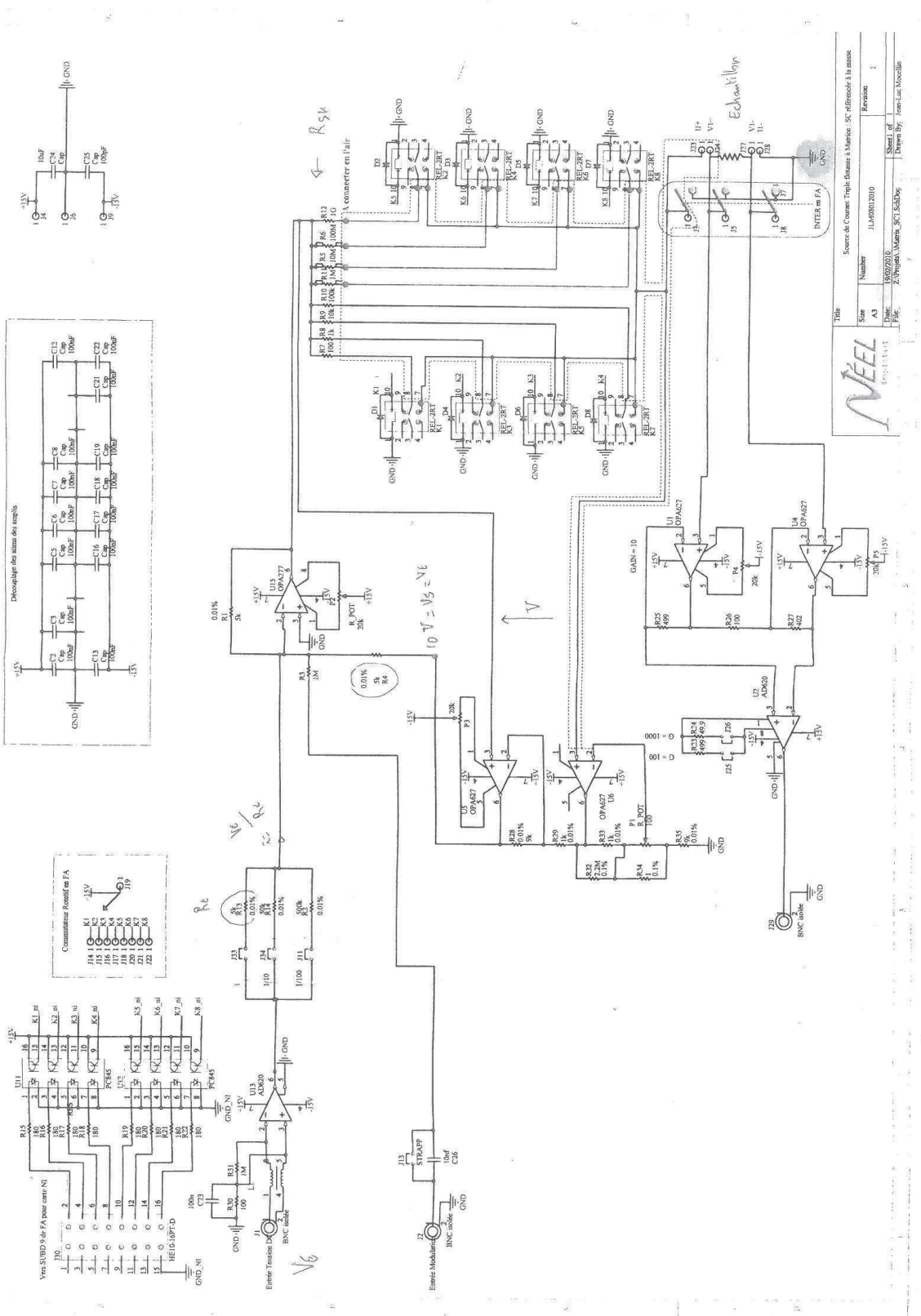

FIGURE B.1: Floatting current source electrical circuit

Bibliographie

[1] J. Anderson, D. Peterson, and D. Finnemore. Anisotropy of the Superconducting Energy Gap in Th. *Physical Review*, 179(2) :472–474, March 1969.

[2] D. Angelescu. Heat transport in mesoscopic systems. *Superlattices and Microstructures*, 23(3-4) :673–689, March 1998.

[3] K. Yu. Arutyunov, T. I. Suppula, J. K. Suoknuuti, and J. P. Pekola. Influence of magnetic field on cooling by normal-insulator–superconductor junctions. *Journal of Applied Physics*, 88(1) :326, July 2000.

[4] F. Balestro. *Dynamique quantique d'un SQUID-DC*. PhD thesis, 2003.

[5] A. Bardas and D. Averin. Peltier effect in normal-metal - superconductor microcontacts. *Physical Review B*, 52(17) :12873–12877, 1995.

[6] J. Bardeen, L. N. Cooper, and J. R. Schrieffer. Theory of superconductivity. *Physical Review*, 108(5) :1175–1204, 1957.

[7] C. W. J. Beenakker, M. Kindermann, and Yu. V. Nazarov. Temperature dependent third cumulant of tunneling noise. *Physical Review Letters*, 90(17) :176802, January 2003.

[8] G. Bergmann. Weak Localization in Thin Films a time-of-flight experiment with conduction electrons. *Physics Reports*, 107(1) :1–58, 1983.

[9] B. L. Blackford and R. H. March. A tunneling investigation of energy-gap anisotropy in superconducting bulk tin crystals. *Journal of Low Temperature Physics*, 43(2) :397, 1969.

[10] G. E. Blonder, M. Tinkham, and T. M. Klapwijk. Transition from metallic to tunneling regimes in superconducting microconstrictions : Excess current, charge imbalance, and supercurrent conversion. *Physical Review B*, 25(7) :4515–4532, 1982.

[11] S. Chaudhuri and I. J. Maasilta. Cooling, conductance, and thermometric performance of nonideal normal metal-superconductor tunnel junction pairs. *Physical Review B*, 85(1) :014519, January 2012.

[12] A. M. Clark, N. A. Miller, A. Williams, S. T. Ruggiero, G. C. Hilton, L. R. Vale, J. A. Beall, K. D. Irwin, and J. N. Ullom. Cooling of bulk material by electron-tunneling refrigerators. *Applied Physics Letters*, 86(17) :173508, 2005.

[13] A. M. Clark, M. L. Van Den Berg, and J. N. Ullom. Fabricating NIS tunnel Junctions on Single Crystal Superconducting Substrate by a Lithographic Process. *IEEE Transactions on Applied Superconductivity*, 13(2) :1111–1113, 2003.

[14] A. M. Clark, A. Williams, S. T. Ruggiero, M. L. van den Berg, and J. N. Ullom. Practical electron-tunneling refrigerator. *Applied Physics Letters*, 84(4) :625, 2004.

[15] B. Cord, C. Dames, K. K. Berggren, and J. Aumentado. Robust shadow-mask evaporation via lithographically controlled undercut. *Journal of Vacuum Science & Technology B : Microelectronics and Nanometer Structures*, 24(6) :3139, 2006.

[16] G. J. Dolan. Offset masks for lift-off photoprocessing. *Applied Physics Letters*, 31(5) :337, 1977.

[17] R. C. Dynes, V. Narayanamurti, and J. P. Garno. Direct Measurement of Quasiparticle-Lifetime broadening in a Strong-Coupled Superconductor. *Physical Review Letters*, 41(21) :1509–1512, 1978.

[18] H. Fröhlich. Theory of the Superconducting State. I. The Ground State at the Absolute Zero of Temperature. *Physical Review*, 79(5) :845–856, September 1950.

[19] G. Gamow. Zur Quantentheorie des Atomkernes. *Zeitschrift Für Physik*, 51(3-4) :204–212, 1928.

[20] V. F. Gantmakher. The experimental study of electron-phonon scattering in metals. *Reports on Progress in Physics*, 37(3) :317–362, March 1974.

[21] I. Giaever. Electron Tunneling Between Two Superconductors. *Physical Review Letters*, 5(10) :464–466, November 1960.

[22] I. Giaever. Energy Gap in Superconductors Measured by Electron Tunneling. *Physical Review Letters*, 5(4) :147–148, August 1960.

[23] I. Giaever. Electron tunneling and superconductivity. *Reviews of Modern Physics*, 46(2) :245, 1974.

[24] I. Giaever and K. Megerle. Study of Superconductors by Electron Tunneling. *Physical Review*, 122(4) :1101–1111, May 1961.

[25] F. Giazotto, T. Heikkilä, A. Luukanen, A. Savin, and J. P. Pekola. Opportunities for mesoscopics in thermometry and refrigeration : Physics and applications. *Reviews of Modern Physics*, 78(1) :217–274, March 2006.

[26] F. Giazotto, T. Heikkilä, A. Luukanen, A. Savin, and J. P. Pekola. Erratum : Opportunities for mesoscopics in thermometry and refrigeration : Physics and applications [Rev. Mod. Phys. 78, 217 (2006)]. *Reviews of Modern Physics*, 81(3) :1351–1351, 2009.

[27] F. W. J. Hekking and Yu. V. Nazarov. Subgap conductivity of a superconductor–normal-metal tunnel interface. *Physical Review B*, 49(10) :6847–6852, 1994.

[28] F. W. J. Hekking, A. O. Niskanen, and J. P. Pekola. Electron-phonon coupling and longitudinal mechanical-mode cooling in a metallic nanowire. *Physical Review B*, 77(3) :033401, 2008.

[29] B. Huard, H. Pothier, D. Esteve, and K. Nagaev. Electron heating in metallic resistors at sub-Kelvin temperature. *Physical Review B*, 76(16) :1–9, October 2007.

[30] J .B. B Johnson. Thermal Agitation of Electricity in Conductors. *Physical Review*, 32(July) :97–109, 1928.

[31] J. Karvonen and I. Maasilta. Influence of Phonon Dimensionality on Electron Energy Relaxation. *Physical Review Letters*, 99(14) :145503, October 2007.

[32] J. Karvonen, L. J. Taskinen, and I. J. Maasilta. Observation of disorder-induced weakening of electron-phonon interaction in thin noble-metal films. *Physical Review B*, 72(1) :012302, July 2005.

[33] J. T. Karvonen, T. Kühn, and I. J. Maasilta. Phonon transport in suspended silicon nitride membranes at low temperatures. *Journal of Physics Conference Series*, 150(1) :012019, 2009.

[34] J. T. Karvonen, L. J. Taskinen, and I. J. Maasilta. Electron-phonon interaction in thin copper and gold films. *Physica Status Solidi C*, 1(11) :2799–2802, 2004.

[35] J. T. Karvonen, L. J. Taskinen, and I. J. Maasilta. Influence of Temperature Gradients on Tunnel Junction Thermometry below 1 K : Cooling and Electron–Phonon Coupling. *Journal of Low Temperature Physics*, 146(1-2) :213–226, December 2006.

[36] P. J. Koppinen and I. Maasilta. Phonon Cooling of Nanomechanical Beams with Tunnel Junctions. *Physical Review Letters*, 102(16) :165502, April 2009.

[37] P. J. Koppinen and I. J. Maasilta. Cooling of suspended nanostructures with tunnel junctions. *Journal of Physics : Conference Series*, 150(1) :012025, February 2009.

[38] F. Lecocq, I. M. Pop, Z. H. Peng, I. Matei, T. Crozes, T. Fournier, C. Naud, W. Guichard, and O. Buisson. Junction fabrication by shadow evaporation without a suspended bridge. *Nanotechnology*, 22(31) :315302, August 2011.

[39] M. M. Leivo and A. J. Manninen. NIS chip refrigeration. *Cryogenics*, 39(8) :653–657, 1999.

[40] M. M. Leivo, A. J Manninen, and J. P. Pekola. Microrefrigeration by Normal metal/Insulator/Superconductor Tunnel Junctions. *Applied Superconductivity*, 5(97) :227–233, 1998.

[41] M. M. Leivo, J. P. Pekola, and D. V. Averin. Efficient Peltier refrigeration by a pair of normal metal/insulator/superconductor junctions. *Applied Physics Letters*, 68(14) :1996, 1996.

[42] E. M. Lifschitz and L. P. Pitaevskii. *Statistical Physics, Part 2*. Pergamon p edition, 1980.

[43] P. J. Lowell, G. C. O'Neil, J. M. Underwood, and J. N. Ullom. Andreev Reflections in Micrometer-Scale Normal Metal-Insulator-Superconductor Tunnel Junctions. *Journal of Low Temperature Physics*, (to be published) :1–6, November 2011.

[44] A. J. Manninen, J. K. Suoknuuti, M. M. Leivo, and J. P. Pekola. Cooling of a superconductor by quasiparticle tunneling. *Applied Physics Letters*, 74(20) :3020, 1999.

[45] M. Meschke, W. Guichard, and J. P. Pekola. Single-mode heat conduction by photons. *Nature*, 444 :187–190, December 2006.

[46] N. A. Miller. *Using electron-tunneling refrigerators to cool electrons, membranes, and sensors*. PhD thesis, 2008.

[47] N. A. Miller, W. Duncan, J. Beall, G. C. Hilton, K. Irwin, D. R. Schmidt, and J. Ullom. Development of a solid-state 100mK refrigerator for user-supplied microelectronics. *Nuclear Instruments and Methods in Physics Research Section A : Accelerators, Spectrometers, Detectors and Associated Equipment*, 559(2) :633–635, 2006.

[48] N. A. Miller, G. C. O'Neil, J. a. Beall, G. C. Hilton, K. D. Irwin, D. R. Schmidt, L. R. Vale, and J. N. Ullom. High resolution x-ray transition-edge sensor cooled by tunnel junction refrigerators. *Applied Physics Letters*, 92(16) :163501, 2008.

[49] J. T. Muhonen, A. O. Niskanen, M. Meschke, Yu. Pashkin, J. S. Tsai, L. Sainiemi, S. Franssila, and J. P. Pekola. Electronic cooling of a submicron-sized metallic beam. *Applied Physics Letters*, 94(7) :073101, 2009.

[50] M. Nahum, T. M. Eiles, and John M. Martinis. Electronic microrefrigerator based on a normal-insulator-superconductor tunnel junction. *Applied Physics Letters*, 65(24) :3123–3125, December 1994.

[51] H. Q. Nguyen, L. M. A. Pascal, Z. H. Peng, O. Buisson, B. Gilles, C. Winkelmann, and Hervé Courtois. Etching suspended superconducting hybrid junctions from a multilayer. *Applied Physics Letters submitted*, November 2011.

[52] H. Nyquist. Thermal agitation of electric charge in conductors. *Physical Review*, 32(July) :110–113, 1928.

[53] T. Ojanen and T. Heikkilä. Photon heat transport in low-dimensional nanostructures. *Physical Review B*, 76(7) :073414, August 2007.

[54] T. Ojanen and A.-P. Jauho. Mesoscopic Photon Heat Transistor. *Physical Review Letters*, 100(15) :155902, April 2008.

[55] L. Pascal, H. Courtois, and F. W. J. Hekking. Circuit approach to photonic heat transport. *Physical Review B*, 83(12) :125113, March 2011.

[56] J. P. Pekola, D. V. Anghel, T. I. Suppula, J. K. Suoknuuti, A. J. Manninen, and M. Manninen. Trapping of quasiparticles of a nonequilibrium superconductor. *Applied Physics Letters*, 76(19) :2782, 2000.

[57] J. P. Pekola and F. W. J. Hekking. Normal-metal-superconductor tunnel junction as a Brownian refrigerator. *Physical Review Letters*, 98(21) :210604, 2007.

[58] J. P. Pekola, V. Maisi, S. Kafanov, N. Chekurov, A. Kemppinen, Yu. Pashkin, O.-P. Saira, M. Möttönen, and J. S. Tsai. Environment-Assisted Tunneling as an Origin of the Dynes Density of States. *Physical Review Letters*, 105(2) :02680, July 2010.

[59] J. P. Pekola, A. J. Manninen, M. M. Leivo, K. Yu. Arutyunov, J. K. Suoknuuti, T. I. Suppula, and B. Collaudin. Microrefrigeration by quasiparticle tunnelling in NIS and SIS junctions. *Physica B : Condensed Matter*, 280(1-4) :485–490, 2000.

[60] J. P. Pekola, R. J. Schoelkopf, and J. N. Ullom. Cryogenics on a Chip. *Physics Today*, 57(5) :41, 2004.

[61] J. T. Peltonen, M. Helle, A. V. Timofeev, P. Solinas, F. W. J. Hekking, and J. P. Pekola. Brownian refrigeration by hybrid tunnel junctions. *Physical Review B*, 84(14) :144505, October 2011.

[62] J. T. Peltonen, J. T. Muhonen, M. Meschke, N. Kopnin, and J. P. Pekola. Magnetic-field-induced stabilization of nonequilibrium superconductivity in a normal-metal/insulator/superconductor junction. *Physical Review B*, 84(22) :220502, December 2011.

[63] J. B. Pendry. Quantum limits to the flow of information and entropy. *Physics*, 16(October 1982) :2161–2171, 1983.

[64] H. Pothier, S. Guéron, N. O. Birge, D. Esteve, and M. H. Devoret. Energy Distribution Function of Quasiparticles in Mesoscopic Wires. *Physical Review Letters*, 79(18) :3490–3493, 1997.

[65] H. Pothier, S. Guéron, D. Esteve, and M. Devoret. Flux-Modulated Andreev Current Caused by Electronic Interference. *Physical Review Letters*, 73(18) :2488–2491, October 1994.

[66] J. Prance, C. Smith, J. Griffiths, S. Chorley, D. Anderson, G. Jones, I. Farrer, and D. Ritchie. Electronic Refrigeration of a Two-Dimensional Electron Gas. *Physical Review Letters*, 102(14) :146602, April 2009.

[67] O. Quaranta, P. Spathis, F. Beltram, and F. Giazotto. Cooling electrons from 1 to 0.4 K with V-based nanorefrigerators. *Applied Physics Letters*, 98(3) :032501, January 2011.

[68] S. Rajauria, H. Courtois, and B. Pannetier. Quasiparticle-diffusion-based heating in superconductor tunneling microcoolers. *Physical Review B*, 80(21) :214521, December 2009.

[69] S. Rajauria, P. Gandit, T. Fournier, F. W. J. Hekking, B. Pannetier, and H. Courtois. Andreev Current-Induced Dissipation in a Hybrid Superconducting Tunnel Junction. *Physical Review Letters*, 100(20) :207002, 2008.

[70] S. Rajauria, P. Luo, T. Fournier, F. Hekking, H. Courtois, and B. Pannetier. Electron and Phonon Cooling in a Superconductor–Normal-Metal–Superconductor Tunnel Junction. *Physical Review Letters*, 99(4) :047004, July 2007.

[71] S. Rajauria, L. Pascal, Ph. Gandit, F. W. J. Hekking, B. Pannetier, and H. Courtois. Efficiency of quasiparticle evacuation in superconducting devices. *Physical Review B*, 85(2) :020505, January 2012.

[72] M. Yu. Reizer. Effective electron-electron interaction in metals and superconductors. *Physical Review B*, 39(3) :1602–1608, January 1989.

[73] M. Yu. Reizer. Electron-phonon relaxation in pure metals and superconductors at very low temperatures. *Physical Review B*, 40(8) :5411–5416, September 1989.

[74] N. Roch. *Transistors à molécule unique : des effets Kondo exotiques à la spintronique moléculaire*. PhD thesis, 2009.

[75] M. Roukes, M. Freeman, R. Germain, R. Richardson, and M. B. Ketchen. Hot electrons and energy transport in metals at millikelvin temperatures. *Physical Review Letters*, 55(4) :422–425, July 1985.

[76] J. Rowell and D. Tsui. Hot electron temperature in InAs measured by tunneling. *Physical Review B*, 14(6) :2456–2463, September 1976.

[77] D. Saint-James. Elementary excitations in the vicinity of the surface separating a normal metal and a superconducting metal.Excitations élémentaires au voisinage de la surface de séparation d'un métal normal et d'un métal supraconducteur. *Journal de Physique*, 25(10) :899, 1964.

[78] D. R. Schmidt, R. J. Schoelkopf, and Cleland A. N. Photon-Mediated Thermal Relaxation of Electrons in Nanostructures. *Physical Review Letters*, 93(4) :045901, July 2004.

[79] K. Schwab, E. A. Henriksen, J. M. Worlock, and M. L. Roukes. Measurement of the quantum of thermal conductance. *Nature*, 404(April 2000) :974–977, 2010.

[80] A. Sergeev and V. Mitin. Electron-phonon interaction in disordered conductors : Static and vibrating scattering potentials. *Physical Review B*, 61(9) :6041–6047, March 2000.

[81] E Serret. *Etude de réseaux de nanojonctions Josephson : compétition entre le champ magnétique et la géométrie*. PhD thesis, 2002.

[82] U. Sivan and Y. Imry. Multichannel Landauer formula for thermoelectric transport with application to thermopower near the mobility edge. *Physical Review B*, 33(1) :551–558, 1986.

[83] D. H. Slichter, O. Naaman, and I. Siddiqi. Millikelvin thermal and electrical performance of lossy transmission line filters. *Applied Physics Letters*, 94(19) :192508–192508, 2009.

[84] Solymar. *Superconductive Tunnelling & Applications*. Wiley-inte edition.

[85] G. Stan, S. Field, and J. Martinis. Critical Field for Complete Vortex Expulsion from Narrow Superconducting Strips. *Physical Review Letters*, 92(9) :097003, March 2004.

[86] A. H. Steinbach, J. M. Martinis, and M. H. Devoret. Observation of hot-electron shot noise in a netallic resistor. *Physical review letters*, 76(20) :3806–3809, May 1996.

[87] E. Swartz and R. Pohl. Thermal boundary resistance. *Reviews of Modern Physics*, 61(3) :605–668, July 1989.

[88] A. V. Timofeev, C. P. Garcia, N. B. Kopnin, A. M. Savin, M. Meschke, F. Giazotto, and J. P. Pekola. Recombination-limited energy relaxation in a Bardeen-Cooper-Schrieffer superconductor. *Physical Review Letters*, 102(1) :017003, 2009.

[89] A. V. Timofeev, M. Helle, M. Meschke, M. Möttönen, and J. P. Pekola. Electronic Refrigeration at the Quantum Limit. *Physical Review Letters*, 102(20) :200801, May 2009.

[90] M. Tinkham. *Introduction to Superconductivity*, volume vol.6 of *International series in pure and applied physics*. McGraw-Hill, 1996.

[91] J. M. Underwood, P. J. Lowell, G. C. O'Neil, and J. N. Ullom. Surprising insensitivity of sub-Kelvin electron-phonon coupling to substrate properties. *Physical Review Letters*, 107 :255504, 2011.

[92] B. Van Wees, P. de Vries, P. Magnée, and T. M. Klapwijk. Excess conductance of superconductor-semiconductor interfaces due to phase conjugation between electrons and holes. *Physical Review Letters*, 69(3) :510–513, July 1992.

[93] J. Voutilainen, T. Heikkilä, and N. Kopnin. Nonequilibrium phenomena in multiple normal-superconducting tunnel heterostructures. *Physical Review B*, 72(5) :054505, August 2005.

[94] F. C. Wellstood, C. Urbina, and J. Clarke. Hot-electron limitation to the sensitivity of the dc superconducting quantum interference device. *Applied Physics Letters*, 54(25) :2599, 1989.

[95] F. C. Wellstood, C. Urbina, and J. Clarke. Hot-electrons effects in metals. *Physical Review B*, 49(9) :5942, 1994.

[96] B. Yurke and J. Denker. Quantum network theory. *Physical Review A*, 29(3) :1419–1437, March 1984.

[97] T. Zijlstra, C. F. J. Lodewijk, N. Vercruyssen, F. D. Tichelaar, D. N. Loudkov, and T. M. Klapwijk. Epitaxial aluminum nitride tunnel barriers grown by nitridation with a plasma source. *Applied Physics Letters*, 91(23) :233102, December 2007.

Refroidissement Electronique et Couplages Thermiques dans les Circuits Hybrides Supraconducteurs.

Le refroidissement électronique de jonctions tunnel Supraconducteur - Isolant - métal Normal (S-I-N) a lieu grâce la bande d'énergie interdite du supraconducteur, qui agit tel un filtre laissant passer les électrons les plus énergétiques par effet tunnel. Cependant, l'efficacité de tels refrigérateurs électroniques est habituellement plus faible que les prédictions théoriques. Après l'introduction des équations décrivant le refroidissement électronique dans une jonction tunnel, nous présentons les différentes limitations fondamentales, parmi elles les couplages thermiques entre bains thermiques d'électrons ou de phonons et la relaxation des quasi-particules. Afin d'avoir une meilleure compréhension des différents couplages thermiques en jeu, nous avons mis au point une expérience permettant de mesurer indépendamment la température des électrons et des phonons. Un réfrigérateur hors équilibre est ainsi étudié dans les régimes de refroidissement et de chauffage. Les résultats sont interprétés en utilisant un modèle thermique qui tient compte des transferts de chaleur entre électrons, phonons et photons. En particuliers, le canal photonique de chaleur lié au bruit thermique dans les résistances du circuit apporte une contribution de chaleur supplémentaire dépendant de la transmission du circuit de couplage. Nous nous sommes intéressées à l'amélioration du refroidissement électronique sous champ magnétique, facilitant la relaxation des quasi-particules dans le supraconducteur. Enfin nous avons développer un procédé de fabrication permettant d'obtenir de large jonctions S-I-N-I-S avec un ilôt métallique suspendu découplé du substrat.

Electronic refrigeration and Thermal couplings in Superconducting Hybrid Devices.

Electronic cooling in Superconductor - Insulator - Normal metal (S-I-N) junction is based on the energy selectivity of electron tunneling induced by the superconductor energy gap. Nevertheless, the efficiency of coolers based on such junctions is usually significantly less than theoretically expected. After introducing the principle of superconducting micro-coolers, we present the fundamental limitations to electronic cooling. We focus on the different thermal couplings between electron and phonon thermal baths and the relaxation of hot quasi-particles deposited in the superconductor. We have designed an experiment to monitor independently electron and phonon temperatures. An electronic cooler was studied under out-of-equilibrium conditions, in both the cooling and the heating regimes. The results are interpreted using a thermal model, which takes into account the heat transfers between the electron, phonon and photon baths. In particular, the photonic heat flow related to the thermal noise arising in the circuit resistors can bring an additional heat contribution, depending on the transmission of the biasing circuit. Moreover, we investigate the enhancement of quasi-particles relaxation under magnetic field, leading to an enhanced quasi-particle relaxation. Finally we develop a process to fabricate S-I-N-I-S coolers with large junctions and a suspended Normal metal island decoupled from the substrate.